Grid Filter Models for the Large Eddy Simulation of Fluid Flows

THÈSE N^O 4818 (2010)

PAR

Marc Anthony David HABISREUTINGER

EPFL

ÉCOLE POLYTECHNIQUE
FÉDÉRALE DE LAUSANNE

Suisse
2010

When I meet God, I am going to ask him two questions, why relativity? and why turbulence? I really believe he will have an answer for the first.

Werner Heisenberg

Résumé

En mécanique des fluides, la turbulence peut se produire dans des géométries d'écoulement très simples, pour des fluides newtoniens et sans la nécessité de conditions supplémentaires, telles que gradients de température ou réactions chimiques. Dans les cas standard, des hypothèses intuitives sur la physique des échelles de sous-maille couplées avec les théories classiques de la turbulence peuvent être bien adaptées pour la simulation des grandes échelles. Cependant, pour des situations plus complexes, le comportement des échelles de sous-maille n'est pas clairement identifié, certainement pas aussi intuitif et les théories correspondantes ne sont pas encore disponibles.

La question est de savoir comment procéder lorsque la modélisation fonctionnelle, qui impose un comportement connu aux échelles de sous-maille, n'est pas possible. Ce problème pourrait être résolu par l'utilisation de modèles basés sur une approche de déconvolution qui consiste en l'approximation des variables originales depuis leur homologue filtrée. Les quantités originales sont obtenues par le truchement d'une inversion approchée de l'opérateur de filtrage qui est appliqué aux équations décrivant le système au niveau macroscopique. Toutefois, cet avantage est généralement perdu puisque ces modèles sont associés à des approches auxiliaires, directement basées sur une modélisation fonctionnelle, afin de tenir compte des interactions avec les échelles qui ne sont pas représentables sur la discrétisation spatiale utilisée pour la simulation des grandes échelles.

La principale motivation de ce travail est d'éviter le recours à cette modélisation auxiliaire de manière à étendre l'utilisation des modèles de déconvolution à la simulation d'écoulements dont le comportement des échelles de sous-maille n'est pas identifié. En considérant les effets de la discrétisation spatiale comme le seul filtre appliqué aux équations macroscopiques, une interprétation des modèles de déconvolution comme un moyen d'approcher l'effet du filtre de maillage sur les échelles résolues de l'écoulement est démontrée. Par conséquent, une nouvelle catégorie de modèles de sous-maille, les modèles de filtre de maillage, est définie et propose une justification théorique à l'utilisation de modèles de déconvolution pour l'ensemble de la modélisation.

Dans cette perspective, une méthode générale pour le calcul du filtre de convolution permettant de modéliser l'effet du filtre de maillage sur les échelles résolues de la solution est présentée, ce qui constitue une première réponse à la question clé de la discrétisation numérique en simulation des grandes échelles. Cette approche de modélisation est tout d'abord validée en effectuant la simulation des grandes échelles de l'écoulement incompressible d'un fluide newtonien dans une cavité entraînée. Les comparaisons avec des modèles de sous-maille classiques permettent de valider cette approche ainsi que la suppression de modélisation fonctionnelle.

Afin d'étendre le domaine de validité de ces modèles, la simulation des grandes échelles d'un problème de turbulence élastique est envisagée. Dans ce cas, les simulations numériques sont sujettes à des instabilités numériques et la charge de calcul est considérablement accrue par rapport au cas newtonien. En conséquence, les simulations numériques directes disponibles dans la littérature sont limitées à des domaines périodiques et bidimensionels. Parmi ces études, l'écoulement de Kolmogorov viscoélastique est choisi comme cas test.

Mots-clés: Modélisation de sous-maille, modèles de déconvolution, turbulence inertielle, turbulence élastique, fluides viscoélastiques, inversion approchée d'opérateurs projectifs

Abstract

In fluid mechanics, turbulence can occur in very simple flow geometries, for Newtonian fluids and without the need for additional flow conditions such as temperature gradients or chemical reactions. In standard cases, intuitive assumptions on the physics of the subgrid scales coupled with the classical theories of turbulence can be well suited for subgrid modelling in large eddy simulation. However, considering more complex situations such as elastic or plasmas turbulence, the behaviour of the subgrid scales is not clearly identified, certainly not as intuitive and the corresponding theories are not available yet.

The question is how to proceed when the functional modelling, which imposes a known behaviour to the subgrid scales of the flow, is not possible. For instance, this issue could be overcome using deconvolution-based subgrid models which aim at a partial recovery of the original quantities from their filtered counterpart. In principle, functional modelling is avoided by attempting to invert the filtering operator applied to the governing equations. However, this apparent advantage is completely lost since these models are usually coupled with auxiliary approaches, directly based on functional modelling, in order to account for the interactions with the scales which are not representable on the coarse spatial discretization used for large eddy simulation.

The driving motivation of this work is to suppress the need for this secondary modelling which would allow to extend the use of deconvolution-based models to the large eddy simulation of flows whose behaviour of subgrid scales is not identified. Considering the effects of the coarse numerical discretization as the only effective filter applied to the macroscopic equations, an interpretation of the deconvolution models as a way to approximate the effect of the scales lost by numerical discretization on the resolved scales of the flow is demonstrated. Consequently, a new category of subgrid models, the grid filter models, is defined and gives a theoretical justification to the use of deconvolution models for the entire subgrid modelling process.

In this perspective, a general method for the computation of the convolution filter which models the effect of the grid filter on the computable scales of the solution is proposed, thereby addressing the key issue of the numerical discretization in large eddy simulation. This modelling approach is validated performing the large eddy simulation of the incompressible flow of a Newtonian fluid in a lid-driven cubical cavity. Comparisons with classical subgrid models allow to assess the validity of this modelling approach and the suppression of the need for functional modelling.

In order to extend the validity domain of the grid filter models, the large eddy simulation of an elastic turbulence problem is envisaged. Numerical simulations of elastic turbulence are limited by numerical instabilities which are particularly stringent at high elasticity. Moreover, the computational burden resulting from the required space-time resolutions is significantly increased as compared to the Newtonian case. Consequently, available direct numerical simulations are restricted to periodic and two-dimensional cases. Among these studies, the large eddy simulation of the viscoelastic Kolmogorov flow is chosen as benchmark problem.

Keywords: Subgrid modelling, deconvolution models, inertial turbulence, elastic turbulence, viscoelastic fluids, approximate inverse of projective operators

Remerciements

Le travail présenté dans les pages qui suivent met en très étroite relation la modélisation des écoulements de fluides, les méthodes de simulation numérique dites spectrales et d'ordre élevé, ainsi que la modélisation de la turbulence. Ces domaines constituent les principaux axes de recherche que Michel Deville, mon directeur de thèse, a suivi au cours de sa carrière. J'aimerais tout d'abord le remercier pour m'avoir offert la possibilité de travailler avec lui sur ces sujets, mais aussi de m'avoir laissé une entière liberté dans la recherche tout en l'éclairant de ses conseils avisés. Les quelques conférences auxquelles nous avons eu le plaisir de participer, les sorties de laboratoire et les fameuses biérrres belges partagées à Sat, une fois, restent des moments inoubliables.

L'idée directrice de cette thèse est née au cours du projet de Master que j'ai effectué au Laboratoire d'Ingénierie Numérique de l'Ecole Polytechnique Fédérale de Lausanne et sous la supervision de Roland Bouffanais. Elle est le fruit d'un échange pratiquement quotidien qui s'est maintenu après la fin de ce projet et malgré l'éloignement physique. J'aimerais manifester tout le plaisir que j'ai eu au cours de notre collaboration, non seulement pour les compétences et la disponibilité de Roland, mais aussi pour tout ce que j'ai pu apprendre avec et grâce à lui.

Bien qu'une seule personne soit inscrite en couverture en tant qu'auteur, d'autres ont directement contribué à certaines parties de ce travail, au cours de leur projet de semestre ou de Master. Je pense notamment à Christoph Boeckle, Sohrab Kehtari et Christian Vessaz qui ont fourni un travail particulièrement brillant. En me remémorant ces collaborations, je ne peux m'empêcher de dire que la charge d'enseignement des doctorants devrait plutôt porter le nom de plaisir d'encadrement. A cette liste, je dois bien évidemment ajouter Nicolas Fiétier, premier assistant du Laboratoire d'Ingénierie Numérique, et aussi parfois affublé du doux nom de *Terminator* en raison de ses immenses connaissances de la littérature et de sa manière unique d'aborder et de résoudre les problèmes.

A tous ceux qui ont travaillé au Laboratoire d'Ingénierie Numérique, je tiens à exprimer ma gratitude pour leur temps et leur aide. En particulier, je remercie Heidi Francelet et Marie-Madeleine Gruaz pour leur assistance dans les domaines non-scientifiques, Ali Tolou pour son soutien permanent lié à la gestion des ressources de calcul. Je tiens également à remercier tous les professeurs et chargés de cours qui m'ont donné l'occasion de les aider dans leurs activités d'enseignement à l'Ecole Polytechnique Fédérale de Lausanne, soit le Prof. Thomas Gmür, le Dr. Alain Drotz, le Prof. Michel Deville, le Dr. Mark Sawley et le Prof. Peter Monkewitz.

Je suis aussi très reconnaissant envers le Dr. Marco Picasso, le Prof. Timothy Phillips et le Prof. Vincent Legat pour leur participation au comité de thèse, pour avoir pris le temps de lire le manuscrit et pour avoir assisté à la présentation privée. Je tiens également à remercier le Prof. Christophe Ancey pour la présidence du jury et le Prof. Daniel Favrat en tant que co-directeur de thèse.

Que ceux qui gardent le meilleur pour la fin y perçoivent l'expression de mes pensées pour mes parents qui m'ont offert la liberté d'entreprendre les études qui ont précédé ce doctorat. J'aimerais les remercier de m'avoir toujours soutenu et encouragé dans cette voie et d'avoir constamment manifesté leur intérêt pour mes activités.

Acknowledgements

The work presented in the following pages builds a very close relationship between the modelling of fluid flows, numerical simulation methods known as spectral and of high order, and turbulence modelling. These are the main fields of research that Michel Deville, my thesis supervisor, has investigated throughout his career. First of all I would like to thank him for giving me the opportunity to work on these issues but also for giving me full freedom in research while illuminating it with great advices. The few conferences we have had the pleasure of participating to and the famous Belgian beers shared at Sat will remain unforgettable moments.

The underlying idea of this thesis was born during the Master project that I made at the Laboratoire d'Ingénierie Numérique of the Ecole Polytechnique Fédérale de Lausanne under the supervision of Roland Bouffanais. It is the result of a daily exchange that lasted after the end of this project and despite the physical distance. I express the pleasure I had during our collaboration, not only for the skills and the availability of Roland, but also for all that I could learn with and through him.

Although only one person is listed on the cover as author, others have directly contributed to parts of this work, during their semester project or Master thesis. I think especially to Christoph Boeckle, Sohrab Kehtari and Christian Vessaz who provided a particularly brilliant work. In remembering these collaborations, I can not help saying that the teaching load of the Ph.D. students should rather be called a pleasure of coaching. To this list, I have to add Nicolas Fiétier, First Assistant of the Laboratoire d'Ingénierie Numérique, and also sometimes saddled with the sweet name of *Terminator* because of his immense knowledge of literature and his unique way of solving problems.

To everyone who worked at the Laboratoire d'Ingénierie Numérique, I express my appreciation for their time and help. In particular, I thank Heidi Francelet and Marie-Madeleine Gruaz for a very precious assistance in all non-scientific matters, Ali Tolou for his permanent assistance related to the computational resources and Jonas Lätt with whom I had enriching scientific interactions. I wish also to thank all the Professors and Lecturers who gave me the opportunity to assist them in teaching activities at the Ecole Polytechnique Fédérale de Lausanne, that is Prof. Thomas Gmür, Dr. Alain Drotz, Prof. Michel Deville, Dr. Mark Sawley and Prof. Peter Monkewitz.

I am also very grateful to Dr. Marco Picasso, Prof. Timothy Phillips and Prof. Vincent Legat for their participation in the thesis committee, for taking the time to read through the manuscript and for attending the private defence. I would also like to thank Prof. Christophe Ancey for presiding over the committee and Prof. Daniel Favrat as thesis co-director.

Those who keep the best for last should see the expression of my thoughts for my parents who gave me the freedom to undertake the studies that preceded this Ph.D. thesis. I thank them for their support and their constant interest in my activities.

Avant-propos

Il se dit souvent qu'un tiers d'une thèse est compréhensible par tout le monde, qu'un autre tiers est dédié aux experts du domaine et que la partie restante ne demeure accessible qu'à l'auteur lui-même. En raison de la spécialisation croissante des sujets de recherche scientifique, je pense que la réalité est en fait bien pire, du moins en ce qui concerne la première partie.

Ainsi, même si ce travail s'adresse en premier lieu au jury de thèse, puis à une partie restreinte de communauté scientifique, le lectorat visé est plus étendu. En partant de bases relativement générales illustrées par des exemples pratiques, et en retardant autant que possible l'apparition du langage mathématique indispensable à l'expression d'une pensée scientifique et quantitative, le travail présenté dans les pages qui suivent est abordable par un lecteur qui ne disposerait pas de connaissances scientifiques approffondies. Toutefois, par souci de concision, tous les concepts utilisés ne peuvent pas être présentés dans le détail mais des références à d'autres publications jalonnent le texte pour aider le lecteur à poursuivre son parcours.

Dans cette perspective, le choix de la langue est aussi un point crucial, surtout en Suisse, pays aux quatre langues nationales. Au sein de la communauté scientifique, la langue la plus utilisée pour les échanges fut autrefois le grec, puis le latin, et devint le français. Aujourd'hui, l'hégémonie est celle de l'anglais. Comme l'explique très clairement Libero Zupirolli [63], ce choix favorise indéniablement les anglophones. En contrepartie, ils doivent affronter la lecture de textes écrits en anglais apauvri qui ne doivent pas sonner de manière très musicale à leurs oreilles. Comme ils le disent si bien, *"there is no free lunch!"*

Ce travail est le fruit de quatre ans d'apprentissage et de recherche. Il s'inscrit dans l'étude de la turbulence en mécanique des fluides et, par un choix délibéré, il est présenté sous une forme non dogmatique. En effet, peut-être par manque de compétences, de connaissances, d'acharnement, d'imagination, ou simplement de temps, ce travail soulève des questions non encore résolues. Ainsi, les incertitudes et les lacunes ne sont pas passées sous silence mais sciemment soulignées de manière à constituer autant de points d'ancrage pour des recherches ultérieures. Le format s'avère ainsi plus proche de la *disputatio* médiévale que des cours *ex cathedra* dispensés aujourd'hui. Je serais donc particulièrement heureux de voir ces développements repris dans le futur et d'avoir l'occasion de contribuer à leur amélioration.

La proportion de publications exemptes de fautes ou imprécisions est etrêmement réduite. Et même si le jury et divers relecteurs attentifs on passé le manuscrit au peigne fin, cette thèse n'en fait vraisemblablement pas partie. Tout commentaire sur ce texte est donc le bienvenu dans une perspective d'amélioration, de complément et de manière à éviter la propagation d'erreurs.

Foreword

People say that a third of a thesis is understood by everyone, another third is dedicated to the experts of the domain and the remainder will only remain accessible to the author himself. Due to the increasing specialisation of scientific research topics, I think the reality is actually much worse, at least regarding the first part.

Thus, even if this work is primarily intended for the jury, then for a small part of the scientific community, the target audience is wider. Starting from relatively general bases illustrated by practical examples, and by delaying the onset of the mathematical language necessary for the expression of scientific and quantitative thoughts, the work presented in these pages is affordable by a reader who does not have a great scientific knowledge. However, for the sake of conciseness, all the concepts can not be presented in details, but references to other publications mark the text to help the reader to continue its journey.

In this perspective, the choice of the language is also a crucial point, especially in Switzerland, a country with four national languages. Within the scientific community, the most widely used language for trade once was Greek, then Latin, and became French. Today the hegemony is that of English. As explained very clearly Libero Zupirolli [63], this choice favours undeniably English speaking people. In return, they must confront the reading of texts written in poor-English which do not sound that musical in their ears. As they say so, *"there is no free lunch!"*

This work is the result of four years of learning and research addressing the study of turbulence in fluid mechanics. By choice, it is presented in a non-dogmatic way. Indeed, and perhaps because of the lack of skills, knowledge, dedication, imagination, or simply time, this work raises unanswered questions. Thus, the uncertainties and gaps are not ignored but deliberately highlighted to form as many starting points for further research. The presentation is therefore closer to the medieval *disputatio* than to the actual *ex cathedra* lectures. Hence, I would be particularly pleased to see these developments further investigated in the future and to have the opportunity to contribute to their improvement.

Unfortunately, the proportion of publications without errors is extremely small. And despite the useful comments of the jury and some reviewers which read the manuscript with great attention, this thesis makes probably not part of it. Any comment is therefore most welcome in order to improve and complete the content of this work, but also to avoid the propagation of errors.

Contents

Chapter 1

Introduction

The huge development and the accumulation of the scientific knowledge make the research fields and the resulting studies more and more specific. Therefore, setting the stage of a research work, whose title is perhaps only evocative to the few experts of the field, often becomes a challenging task.

The general context of this study is fluid mechanics and more precisely the introduction of a novel approach for turbulence modelling in the numerical simulation of fluid flows. The meaning of these words is perhaps more explicit but they shall be described into more details. In this introduction, as suggested by Stephen Hawking in *The Brief History of Time*, *"Each equation included in a book halves the potential readers"*, the presentation of the ideas and the concepts is privileged over equations and technical aspects.

1.1   Fluid mechanics

The famous quote by Herakleitos of Ephesus *"παντα ρει, και ουδεν μενει."*, which means "Everything flows, nothing stands still.", perfectly reflects the huge domain of application of fluid mechanics. Fluid flows can be illustrated by natural phenomena such as the blowing of the wind, the flow of a river, a snow avalanche, a landslide, a volcanic eruption, or the formation of mountains by the interaction of tectonic plates. The fundamental difference between these flows lies on their time-scale. Over sufficiently long periods of time, materials which are commonly classified as solids are observed in flow. For instance, the glass flow in windows due to gravity forces is only observable over centuries when the bottom becomes thicker than the top. The distinction between fluids and solids appears somewhat blurred and relies on the material behaviour as discussed by Robert Owens and Timothy Phillips [45].

The first known human applications related to fluid mechanics date back to Mesopotamia with the use of hydraulic machinery for irrigation and to the ancient Egypt with the invention of water clocks. Among the conserved works in this area, the earliest go back to the days of the ancient Greece and the investigations of Archimedes of Syracuse on buoyancy forces. After this pioneering contribution, the recent development of this discipline has been characterised by a strong interaction between theory and experiment which began near the end of the 15$^{\text{th}}$ century with Leonardo da Vinci and his observations on the resistance of air to the movement of a solid object.

The laws of classical mechanics introduced by Isaac Newton and his studies on viscosity marked the beginning of the theory of this discipline. Among other mathematicians, physicists and engineers, Blaise Pascal, Louis de Lagrange and Leonhard Euler contributed to the advancement of this theory which essentially relies on classical mechanics, that is on the assumptions of mass, momentum and energy conservation but also on the continuum hypothesis. Despite the discrete character of matter which seems to be composed by elementary particles, fluids are described from a macroscopic point of view and are supposed to be a continuous media. In this framework, the governing equations were established by Claude Navier and George Stokes.

Beside the classical theory, fluid flows were also studied in the framework of the kinetic theory whose bases were laid by Daniel Bernoulli. This statistical and mesoscopic description was further developed by Rudolf Clausius and James Maxwell who formulated the velocity distribution function expressing the proportion of particles having a certain velocity at a given position. This was the first statistical law in physics and inspired the works of Ludwig Boltzmann which gave birth to statistical mechanics. The study of fluid flows is also carried out in a relativistic framework since the derivation by Taub [57] of the corresponding equations. This discipline is mostly dedicated to cosmology problems [1].

Since the beginning of the 20$^{\text{th}}$ century, the studies of fluid flows spread over various domains. For instance, aero- and hydrodynamics are concerned with studying the motion of air and water, particularly when they interact with moving objects such as aircrafts, automobiles, high-speed trains, boats or constructions such as bridges, buildings but also energetic systems such as engines, pumps and turbines. At the scale of the Earth, the short- and mid-term prediction of air and water flows in the atmosphere and the oceans concerns the meteorology whose link with fluid mechanics began with the invention of the barometer by Evangelista Torricelli in the 17$^{\text{th}}$ century.

Rheology deals with the flow and deformation of more complex materials such as muds, sludges, suspensions, polymers, many foods or molten metals. Complex fluids are also studied in the framework of the bio-fluid mechanics whose blood flows in aneurysms or in stenoses and the design of artificial heart valves are among classical problems. Plasma physics is another discipline which is devoted to the study of partially or fully ionised gases whose common examples are the lightning, the polar auroras or the sun. The characteristics of such flows, and in particular their space- and time-scales, stretch over several orders of magnitude from the artificial plasmas generated in laboratories to the cosmic ones of inter-galactic nebulae.

1.2   Turbulence in fluid mechanics

Turbulence is often associated to the flight of an aircraft passing through different atmospheric structures. When the size of these structures is small as compared to the distance travelled in a given time-scale, which is the case in storms or convection cells, the passage from a structure to the other gives rise to high frequency jerks which are referred to as *"turbulences"*.

In the various domains of fluid mechanics, the definition is slightly different, laminar flows are the exception and turbulent flows are rather the rule. Turbulence is a flow regime characterised by the strong coupling among flow structures which stretch over a broad range of space- and time-scales. For instance, the range of scales in the flow of a river can stretch from the size of the riverbed to extremely small flow structures whose interaction makes the flow behave in a chaotic manner. This means that any perturbation of the system is exponentially amplified in time. A good illustration is the casino game *La roulette*. The smallest disturbance in the initial conditions leads to enormous differences in the results which are therefore unpredictable. The throw of a dice or of a coin has also a chaotic behaviour. Even if these macroscopic systems are deterministic, the only way of representing the results is the use of probabilities. This is often called the deterministic chaos which is extremely well presented by Pierre Bergé *et al.* in [4].

Another example of turbulent flow is the atmosphere. It is turbulent since the largest scale has the size of the Earth and it can be subdivided into smallest quasi-stable structures known as the Hadley cells, Ferrel cells, Polar cells and jet-streams which redistribute the energy coming from the Sun. This subdivision extends to structures which are of the characteristic size of a mountain, of a tree or even of smaller size and which are more and more unstable and time-dependent. This results in a chaotic behaviour which is well known in meteorology since weather is almost unpredictable

after only three days. Consequently, deterministic predictions are gradually replaced by probabilistic weather forecasts.

In the case of fluids whose viscosity can be assumed as constant, such as air or water, and which are called Newtonian, Osborne Reynolds observed that turbulence occurs when the inertial stresses are large compared to the viscous ones, and introduced the dimensionless Reynolds number to measure this ratio. In the early 1940s, the theory of homogeneous and isotropic turbulence proposed by Andreï Kolmogorov allowed to demonstrate that the range of space-scales varies with respect to the Reynolds number to the power three fourths [28–30]. This kind of turbulence, which can be referred to as inertial turbulence since it is driven by inertial effects, has been the subject of an enormous amount of experimental and theoretical studies.

The development of an elastic turbulence regime was also experimentally observed by Alex Groisman and Victor Steinberg [23] in flows of highly viscous polymer solutions and in the limit of strong elasticity, which is measured by the dimensionless Deborah number. The flows of such fluids display characteristics typical of turbulent flows, even at low velocity and high viscosity, that is in the limit of vanishing Reynolds number. Despite its growing practical interest, elastic turbulence is only partially understood from a theoretical viewpoint and a few studies are available in this field of research. Recent theoretical predictions rely on simplified versions of viscoelastic models, or on the strong analogy with the turbulence of plasmas which has been recently demonstrated by Gordon Ogilvie and Michael Proctor [42].

In technical applications, turbulence shall be sometimes promoted and sometimes avoided. For instance, it can be used to enhance mixing processes but should be avoided to improve the efficiency of an hydraulic turbine. As an other example, the development of viable nuclear fusion reactors requires the production of long-life and stable plasma flows in such a way that nuclear reactions can take place. In experimental devices such as tokamaks or stellerators, turbulence mainly arises from the interaction of the magnetic field imposed for the confinement of the plasma and the magnetic field induced by the electrically charged and moving particles. Understanding and predicting turbulence which controls the confinement properties of any magnetically confined plasma is a key issue on the way towards the industrial use of this energy conversion method.

1.3   Numerical simulation

As shown by the example of fluid mechanics, physics is classically studied by means of theory and experiment. However, the increasing performance of modern computers coupled with the improvement of the numerical analysis algorithms enabled the numerical simulation to become the third way of physics which is more and more used by physicists and engineers for fundamental or applied studies.

The first issue involved in the numerical simulation of any physical system is the definition of a physical model, and thereby of a level of approximation, in order to obtain the required information about its behaviour with a given precision. For instance, the system can be described at the levels of elementary particles, atoms and molecules, or at the meso- and macroscopic levels. A description at a given scale can be interpreted as an averaging of the detailed descriptions obtained at the lower levels and induces a loss of information. This succession of nested levels of description forms a structure which could be compared to onion rings or Russian dolls. Being at a given level actually prevents to see what is inside. The oral quote by Thibaut Vernay, *"La température d'un gaz peut être calculée en connaissant la trajectoire des ses particules. En revanche, en connaissant uniquement la température, il est impossible de reconstruire la trajectoire des particules."*, perfectly illustrates the loss of information induced by the choice of a given level of description.

Moreover, once the level of description is defined, additional assumptions can be made in order to simplify the resulting mathematical model which implies additional restrictions on the validity domain and possibly deteriorates the accuracy. However, adequate assumptions can lead to drastic simplifications without major accuracy drawbacks, but for a limited range of physical situations.

In a second step, the resulting equations must be solved using sufficiently accurate algorithms in order to preserve the precision of the model. The execution of these algorithms requires their implementation on computers which implies hard- and software issues but also places the numerical simulation at the crossroads between physics, mathematics and computer science.

In the particular case of fluid mechanics, which is essentially the study of systems consisting of a large number of interacting atoms and molecules, the choice of a level of approximation and thus a level of averaging is fundamental. For instance, a description at the atomic level leads to the definition of a discrete molecular dynamics system, the mesoscopic viewpoint leads to the Boltzmann equations whereas the macroscopic one corresponding to a scale of representation much larger than the mean free path of molecules leads to a system which is governed by the Navier–Stokes equations. This last level is the one of the continuous media mechanics and is the most common description adopted for numerical fluid mechanics.

As it relies on the continuum mechanics, the Navier–Stokes model is a system of coupled partial differential equations. Its numerical solution requires the spatial discretization of the system in order to retrieve a finite system of coupled ordinary differential equations which can be numerically integrated in time. The resolution requires therefore to discretize the equations in both space and time.

1.4   Turbulence modelling

The flow simulation at the macroscopic level requires to find the solution of the Navier–Stokes equations. This implies the use of a space-time discretization which enables the direct numerical simulation of all the space- and time-scales present in the flow dynamics. This constraint may turn out to be of prohibitive computational cost when the solution of the problem contains a broad range of scales, which is the case for turbulent flows.

In order to solve the macroscopic equations in a turbulent flow case, the computational cost must be reduced by decreasing the number of computed space- and time-scales of the flow. This can only be achieved by the introduction of a coarser level of approximation than the macroscopic one represented by the Navier–Stokes model. Some scales shall be directly computed by numerical simulation while the others are modelled. However, the non-linearity of the equations reflects the dynamic coupling among all scales of the solution which implies that they can not be computed independently. Therefore, an accurate representation of the resolved scales requires the modelling of both unresolved scales and their interaction with resolved ones. Since this modelling represents the action of a large number of scales with those that are resolved, it only reflects the global or average action representing therefore a higher or coarser level of approximation. Several approaches have been introduced in order to decrease the number of degrees of freedom of the simulation and the choice among them also depends on the desired precision and required information on the system dynamics.

In engineering applications, the mostly used approach, referred to as the Reynolds averaged numerical simulation [52], consists in the calculation of the statistical average of the solution. In this framework, the fluctuations are not represented by the numerical simulation and are only accounted by a turbulence model. Assuming the ergodicity [15] of the system, the statistical averaging operation is often associated with a time-averaging to avoid the simulation of the temporal dynamics of

the system.

An alternative approach is the large eddy simulation which relies on the computation of the large flow structures directly and the modelling of the small ones, the scale separation being formally performed by filtering the macroscopic equations. Large-scale structures are obtained by the computed flow dynamics while the behaviour of subgrid scales and their interaction with large eddies are modelled by the additional terms arising from the filtering of the equations. The expression of the additional terms as functions of the resolved quantities is referred to as subgrid modelling.

1.5 Objectives and outline

Like for the model proposed by Joseph Smagorinsky [54] and its multiple subsequent variants, subgrid modelling in large eddy simulation classically relies on a functional modelling strategy, that is on the use of physical assumptions about the behaviour of the subgrid scales in order to approximate their action on the resolved ones. Most of these models only address the energetic aspects of the interaction thereby restricting the modelling to the balance of energy transfers between both scale ranges. The closure of these models is usually based on the theories of isotropic and homogeneous turbulence introduced by Andreï Kolmogorov in the case of Newtonian fluids.

In the particular context of fluid mechanics, turbulence can occur in very simple flow geometries, for fluids of simple rheology and without the need for additional flow conditions such as temperature gradients or chemical reactions. In standard cases, intuitive assumptions on the physics of the subgrid scales coupled with the classical theories of turbulence can be well suited for subgrid modelling. However, the trend in fluid mechanics is to study complex flows of complex fluids which reveals a substantial need for improvement in terms of subgrid modelling. For instance, in cases such as elastic or plasmas turbulence, the physics of the subgrid scales is not clearly identified, certainly not as intuitive and the corresponding theories are not available yet.

The question is how to proceed when the functional modelling, which imposes a known behaviour to the subgrid scales of the flow, is not possible. For instance, this issue could be overcome by the use of deconvolution-based models which aim at the partial recovery of the original quantities from their filtered counterparts. In principle, functional modelling is avoided by attempting to invert the filtering operator applied to the macroscopic equations. These models are purely algorithmic and do not require to resort to any *a priori* assumption about the function of the subgrid scales. But as noted by Julian Domaradzki and Nikolaus Adams [18], *"Since the need for the physical (*i.e. *functional) models is removed, this approach seems to be more promising than the classical models. However, this promise is not fulfilled if the effects of numerical discretization are not accounted for"*. Indeed, their advantage is completely lost since deconvolution models are usually supplemented by classical approaches based on functional modelling in order to account for the effects of the scales lost by numerical discretization on the resolved ones. This secondary modelling procedure actually prevents their use in complex situations, that is when the physics of the subgrid scales is not clearly identified.

The driving motivation of this work is to pave the way towards the suppression of the need for functional modelling which would allow to extend the use of deconvolution-based models to the large eddy simulation of more complex flows and fluids. But this way is certainly very long and probably not as straight as the one presented hereafter. However let us assume, but not swear, that we tell the truth and only the truth. . . Hence, considering the effects of the coarser numerical discretization as the only effective filter applied to the macroscopic equations, an interpretation to the use of deconvolution models as a way to approximate the effect of the scales lost by numerical discretization on the resolved scales of the flow is demonstrated. Consequently, a new category

of deconvolution-based subgrid models, the grid filter models, is defined and gives a theoretical justification to the use of deconvolution models for the entire subgrid modelling. In this perspective, a general method for the computation of the convolution filter which models the effect of the grid filter on the computable scales of the solution is proposed, thereby addressing the key issue of the numerical discretization in large eddy simulation.

The first step towards the validation of this subgrid modelling approach is the large eddy simulation of an inertial turbulence problem. Among such classical problems, the focus is put on the incompressible flow of a Newtonian fluid in a lid-driven cubical cavity. The direct numerical simulation of the flow is due to Emmanuel Leriche and Spiros Gavrilakis and detailed in [36]. Subgrid modelling in the case of a flow with coexisting laminar, transitional and turbulent zones such as the lid-driven cubical cavity flow represents a challenging problem, despite the simplicity of the geometry. Moreover, as the flow is confined and recirculating, any under- or over-dissipative character of the subgrid model can be clearly identified.

In order to extend the validity domain of the grid filter models, the large eddy simulation of an elastic turbulence problem is envisaged. Numerical simulations of elastic turbulence are limited by numerical instabilities which are particularly stringent at high elasticity. Moreover, the computational burden resulting from the required space-time resolutions is significantly increased as compared to the Newtonian case. Consequently, available direct numerical simulations are restricted to periodic and two-dimensional cases. Among these studies, the large eddy simulation of the viscoelastic Kolmogorov flow, already investigated by direct numerical simulation by Stefano Berti *et al.* in [5], is chosen as benchmark problem.

1.6   Software projects

As previously detailed, numerical simulation is multidisciplinary since it requires a knowledge in physics to deal with the modelling issues, in mathematics to develop or properly choose the resolution algorithms as well as in computer science for their implementation and execution on computers. The latter tasks are often completely neglected in the presentation of a work related to numerical simulation although the resolution of a particular problem commonly requires many thousands of hours for programming and computation. Moreover, modern computer architectures rely on distributed computing and memory units which are interconnected by a communication network. In order to fully benefit from the computational power, the algorithms must be parallelized in an efficient way which implies major additional issues.

The large eddy simulations of the lid-driven cavity flow reported hereafter are performed using the open source code SPECULOOS which stands for SPECtral Unstructured ELements Object-Oriented System. The development of this code was initiated by Michel Deville, Vincent Van Kamenade and Yves Dubois-Pèlerin [19]. It is an object-oriented toolbox written in C^{++} for the numerical solution of partial differential equations by the spectral and mortar elements method. For instance, specific modules for the simulation of Newtonian and viscoelastic fluid flows, multiphase flows and fluid-structure interaction have been developed. It can be used in sequential and parallel versions with the Linux environment.

The direct and large eddy simulations of the viscoelastic Kolmogorov flow are performed with the open source code FURKA, which stands for FoUrier Runge-KuttA. This project was initiated by Christoph Boeckle and Marc Habisreutinger in 2008 at the Ecole Polytechnique Fédérale de Lausanne with the aim of implementing the Fourier pseudo-spectral method for the spatial discretization coupled with adaptive Runge-Kutta schemes for the integration of ordinary differential equations. The first version of the code was written in Fortran 90 by Christoph Boeckle for the

direct numerical simulations of viscoelastic fluid flows reported in [7]. The extension for large eddy simulation and the parallel version of the code were subsequently written by Marc Habisreutinger and also translated into the Octave/Matlab language. The code has been originally developed on the Pleiades2[1] commodity cluster, then ported on the Cadmos Blue Gene/P[2].

[1] http://pleiades.epfl.ch/
[2] http://bluegene.epfl.ch/

Chapter 2

Governing equations

As suggested by the title of this chapter, avoiding the use of equations will be much more difficult. Indeed, this chapter contains more that sixty equations which means, following Hawking's law, that the proportion of potential readers would be reduced to 2^{-60}. If this law was true, writing this work would not be very useful and even the author would not be sure to reach the end of the chapter... In reality, the minimum amount of readers is seven and their names are actually available on the front page of this document.

The first issue involved in the numerical simulation is the definition of a mathematical model which allows to obtain the relevant information about the behaviour of the physical system. In the framework of numerical fluid dynamics, the aim is usually to compute the evolution of the macroscopic variables of the flow, such as the velocity, the temperature or the density. Therefore, the description presented hereafter relies on the continuous media mechanics and the macroscopic description which leads to a system of coupled partial differential equations, referred to as the Navier–Stokes model.

The equations used for the large eddy simulation, also referred to as filtered equations and describing the system at a coarser level, are derived in a general framework by filtering in space the equations resulting from the macroscopic description. This allows to deal with any set of equations and not only the particular Navier–Stokes model considered hereafter.

2.1 Modelling framework

As illustrated in figure 2.1, the laws of actual physics are able to describe a relatively wide range of phenomena which stretches from the length scale of elementary particles to the one of the universe, and from the slowest velocity scale to the one of particles travelling close to the speed of light c. While the aim is to discover universal laws, its theories usually lie in specific sub-domains of validity, sometimes for the sake of simplicity, some other times because of our incomplete understanding of nature.
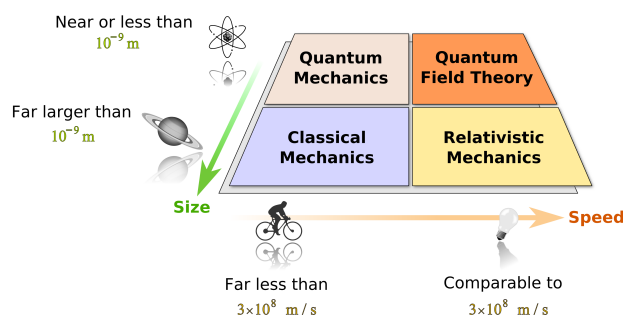

Fig. 2.1: Modern physics fields. Courtesy of wikipedia.org.

Loosely speaking, the laws of classical mechanics accurately describe systems whose length scales are much greater than the atomic one and whose motions are much slower than the speed of light. The motion of a particle in a d-dimensional space is described by its position

$$\boldsymbol{x}(t) = (x_1, x_2, \ldots, x_\mathrm{d}) \tag{2.1}$$

expressed as a function of time t which is supposed to be absolute, that is independent of the reference frame. While the number of space dimensions of our universe seems to be fixed to three, this quantity is introduced as a parameter since bi-dimensional fluid flows are also studied in this work. In the context of classical mechanics, the velocity of a particle is defined as the ratio

$$\dot{\boldsymbol{x}}(t) = \lim_{\Delta t \to 0} \frac{\Delta \boldsymbol{x}}{\Delta t} = \frac{d\boldsymbol{x}}{dt}, \tag{2.2}$$

where $\Delta \boldsymbol{x}$ and Δt respectively represent the variation of position and the corresponding time-interval.

An accurate description of systems whose components have speeds approaching the speed of light requires the use of relativistic mechanics, which basically replaces the notions of absolute time and space with a coupled space-time. The motion of a particle is described as a succession of events in a space-time of d+1 dimensions. The position of the particle is thus expressed by

$$\boldsymbol{s} = (\mathrm{c}t, x_1, x_2, \ldots, x_\mathrm{d}). \tag{2.3}$$

The description at the atomic and sub-atomic scales relies on the quantum mechanics which introduces a probabilistic description of the particles and of their interactions, while the quantum field theory aims at the unification of the quantum and relativistic mechanics, that is to the unification of the most general laws known to date.

As detailed by this brief and schematic overview, the description of a system requires to define a level of description, that is considering the phenomena at a given length scale, and to consider additional assumptions such as the characteristic speed as compared to the speed of light.

Although recent and very promising techniques used for the simulation of fluid flows rely on a mesoscopic description of the phenomena and the resolution of the Boltzmann equation, the common framework is still the continuous media mechanics. Moreover, the focus is put on flows whose local velocity is much smaller than the speed of sound and thereby negligible as compared to the speed of light.

In this case, the aim is to compute the time-evolution of the state variables of the flow in a given space domain, since space and time can be considered as decoupled. This can be done using a material or Lagrangian description which means that the physical phenomenon is studied describing each material particle of the flow, as introduced in (2.2) for the velocity. Conversely, the spatial or Eulerian description relies on the observation of the events occurring at a fixed point of space. In this case the velocity becomes

$$\boldsymbol{v}(\boldsymbol{x}, t) = (\dot{x}_1(\boldsymbol{x}, t), \dot{x}_2(\boldsymbol{x}, t), \ldots, \dot{x}_\mathrm{d}(\boldsymbol{x}, t)), \tag{2.4}$$

which expresses the velocity of the particle which is at the position $\boldsymbol{x}$ at time t. The other state variables of the flow such as the temperature or the density are described in the same way.

2.2 Conservation principles

In the framework of classical mechanics and the continuous description, the governing equations arise from the general conservation principles expressed in a continuous way in space and time.

Focusing on isothermal flows with a local velocity much smaller than the speed of sound, the fluid motion can be described by the principles of conservation of mass and momentum without the need to introduce the conservation of energy.

2.2.1   Conservation of mass

In classical mechanics, the general principle of mass conservation simply states that mass can not be created, destroyed or converted, it remains constant at all times. From a material point of view, this can be expressed following the material domain $\boldsymbol{\Omega}$ which deforms in time as

$$\frac{d}{dt} \int_{\boldsymbol{\Omega}(t)} \rho \, dV = 0, \tag{2.5}$$

where ρ and dV are the density and a differential element of the domain. This relation states that the mass contained in any time-deforming material volume is conserved. The material formulation can be converted into a spatial description using the Reynolds transport theorem [9], which gives

$$\int_{\boldsymbol{\Omega}} \partial_t \rho \, dV + \int_{\partial \boldsymbol{\Omega}} \rho \boldsymbol{v} \cdot \boldsymbol{n} \, dS = 0, \tag{2.6}$$

with ∂_t the partial derivative with respect to time and where $\boldsymbol{n}$ is the outward normal unit vector to the elementary surface dS of the spatial domain. In other words, this equation expresses that the mass variation inside any spatial domain is due to the mass flux through its boundaries. The surface integral can be replaced by a volume integral using the divergence theorem, which leads to

$$\int_{\boldsymbol{\Omega}} \partial_t \rho + \boldsymbol{\nabla} \cdot (\rho \boldsymbol{v}) \, dV = 0, \tag{2.7}$$

where $\boldsymbol{\nabla} = (\partial_{x_1}, \partial_{x_2}, \ldots, \partial_{x_d})$ and which must be verified for any elementary volume in such a way that

$$\partial_t \rho + \boldsymbol{\nabla} \cdot (\rho \boldsymbol{v}) = 0, \qquad \text{in } \boldsymbol{\Omega}, \tag{2.8}$$

thereby expressing the local or differential form of the conservation of mass.

2.2.2   Conservation of linear momentum

The principle of momentum conservation, also known as the Newton's second law, states that the momentum rate of change is due to the sum of the applied forces. Applying this principle to a time-dependent material domain and splitting the forces into the volume and surface contributions, represented by the vectors $\boldsymbol{g}$ and $\boldsymbol{t}(\boldsymbol{n})$ respectively, reads

$$\frac{d}{dt} \int_{\boldsymbol{\Omega}(t)} \rho \boldsymbol{v} \, dV = \int_{\boldsymbol{\Omega}(t)} \boldsymbol{g} \, dV + \int_{\partial \boldsymbol{\Omega}(t)} \boldsymbol{t}(\boldsymbol{n}) \, dS. \tag{2.9}$$

For instance, the volume force can be due to gravity or to an electromagnetic field if the fluid contains charged particles, whereas the contact forces can arise from the contribution of the pressure or the surface tension. Using the Reynolds transport theorem and the Cauchy's theorem [9] for the existence of a stress tensor $\boldsymbol{\sigma}$, such that the contact forces can be expressed as $\boldsymbol{t}(\boldsymbol{n}) = \boldsymbol{\sigma} \cdot \boldsymbol{n}$, yields

$$\int_{\boldsymbol{\Omega}} \partial_t (\rho \boldsymbol{v}) \, dV + \int_{\partial \boldsymbol{\Omega}} \rho \boldsymbol{v} \boldsymbol{v} \cdot \boldsymbol{n} \, dS = \int_{\boldsymbol{\Omega}} \boldsymbol{g} \, dV + \int_{\partial \boldsymbol{\Omega}} \boldsymbol{\sigma} \cdot \boldsymbol{n} \, dS, \tag{2.10}$$

where $(\boldsymbol{v}\boldsymbol{v})_{ij} = v_i v_j$ represents a dyadic product. Finally, the application of the divergence theorem gives

$$\int_{\boldsymbol{\Omega}} \partial_t(\rho \boldsymbol{v}) + \boldsymbol{\nabla} \cdot (\rho \boldsymbol{v}\boldsymbol{v}) \, dV = \int_{\boldsymbol{\Omega}} \boldsymbol{g} + \boldsymbol{\nabla} \cdot \boldsymbol{\sigma} \, dV, \tag{2.11}$$

which in the local form reads

$$\partial_t(\rho \boldsymbol{v}) + \boldsymbol{\nabla} \cdot (\rho \boldsymbol{v}\boldsymbol{v}) = \boldsymbol{g} + \boldsymbol{\nabla} \cdot \boldsymbol{\sigma}, \qquad \text{in } \boldsymbol{\Omega}. \tag{2.12}$$

2.2.3 Conservation of angular momentum

This conservation principle states that the rate of change of the angular momentum of a deforming material region is equal to the sum of applied torques. In other words, this principle reads

$$\frac{d}{dt} \int_{\boldsymbol{\Omega}(t)} \rho \boldsymbol{x} \times \boldsymbol{v} \, dV = \int_{\boldsymbol{\Omega}(t)} \boldsymbol{x} \times \boldsymbol{g} \, dV + \int_{\partial \boldsymbol{\Omega}(t)} \boldsymbol{x} \times (\boldsymbol{\sigma} \cdot \boldsymbol{n}) \, dS. \tag{2.13}$$

After some algebra, omitted for the sake of conciseness, it can be shown that this principle implies the symmetry of the Cauchy stress tensor, that is

$$\boldsymbol{\sigma} = \boldsymbol{\sigma}^{\mathrm{T}}, \tag{2.14}$$

where the superscript T denotes the transpose operation.

2.3 Incompressible and isothermal Navier–Stokes equations

The relative density variations inside a fluid flow are proportional to the square of the Mach number which is defined as the ratio of the local velocity and the local celerity of sound [51]. For sufficiently low values, that is much smaller than the unit, the general Navier–Stokes model can be replaced by its low Mach-number approximation.

In the sequel, the focus is put on the limit and ideal situation of vanishing Mach number, which means that the local velocity is assumed to be infinitely smaller than the celerity of sound, and which leads to the incompressibility assumption

$$\rho(\boldsymbol{x}, t) = \text{const.} \tag{2.15}$$

Moreover, focusing on isothermal flows, the general macroscopic model reduces to the so-called incompressible and isothermal Navier–Stokes equations which are obtained by applying the incompressibility assumption (2.15) to the equations of mass and momentum conservation (2.8) and (2.12)

$$\boldsymbol{\nabla} \cdot \boldsymbol{v} = 0, \tag{2.16}$$
$$\partial_t \boldsymbol{v} + \boldsymbol{\nabla} \cdot (\boldsymbol{v}\boldsymbol{v}) = \rho^{-1}(\boldsymbol{g} + \boldsymbol{\nabla} \cdot \boldsymbol{\sigma}). \tag{2.17}$$

This set of equations must only be augmented by a constitutive equation describing the rheology of the fluid to express the Cauchy stress tensor as function of the flow variables and the macroscopic properties of the fluid.

The Cauchy stress tensor is split into the spherical contribution due to the pressure p and the contribution represented by the extra-stress tensor $\boldsymbol{\tau}$ which characterises the fluid

$$\boldsymbol{\sigma} = \boldsymbol{\tau} - p\boldsymbol{I}. \tag{2.18}$$

In the case of compressible flows, the pressure is obtained through an equation of state such as the ideal gas law whereas, under the incompressibility assumption, it can be determined solving the conservation laws (2.16) and (2.17) directly.

In order to achieve the closure, the Newton's law is introduced to describe the rheology of Newtonian fluids while the Oldroyd-B constitutive model is considered in the case of polymer solutions.

2.3.1   Newtonian fluids

In the case of Newtonian fluids, the extra-stresses reduce to a shear contribution which is proportional to the velocity gradient, the proportionality constant being the dynamic viscosity of the fluid μ. By definition, this kind of fluids, such as air or water, obeys Newton's law which, using the incompressibility assumption (2.15), reduces to

$$\boldsymbol{\tau}_{\mathrm{n}} = 2\mu\dot{\boldsymbol{\gamma}} = \mu(\boldsymbol{\nabla}\boldsymbol{v} + \boldsymbol{\nabla}\boldsymbol{v}^{\mathrm{T}}), \tag{2.19}$$

with $\dot{\boldsymbol{\gamma}}$ the rate-of-strain tensor which is implicitly defined by this relation. The symmetry of the Cauchy stress tensor is trivially demonstrated since $\boldsymbol{\tau}_{\mathrm{n}}$ is symmetric and the pressure contribution is diagonal. The splitting (2.18) and the substitution of the Newtonian rheological model (2.19) into the expression of momentum conservation (2.17) allows to obtain the closed set of equations

$$\boldsymbol{\nabla} \cdot \boldsymbol{v} = 0, \tag{2.20}$$
$$\partial_t \boldsymbol{v} + \boldsymbol{\nabla} \cdot (\boldsymbol{v}\boldsymbol{v}) = \nu\boldsymbol{\nabla}^2\boldsymbol{v} + \rho^{-1}(\boldsymbol{g} - \boldsymbol{\nabla}p), \tag{2.21}$$

where $\nu = \mu/\rho$ is introduced as the kinematic viscosity since the density is assumed to be constant in space and time. The velocity field must be solenoidal as imposed by equation (2.16) arising from the principle of mass conservation.

2.3.2   Oldroyd-B fluids

In order to deal with the rheology of polymer solutions, the extra-stress tensor is first split as

$$\boldsymbol{\tau} = \boldsymbol{\tau}_{\mathrm{n}} + \boldsymbol{\tau}_{\mathrm{p}}, \tag{2.22}$$

where $\boldsymbol{\tau}_{\mathrm{p}}$ represents the additional contributions due to the polymer molecules. The simplest models for the description of such solutions are those of Oldroyd type. These models can be derived from a molecular description considering a suspension of dumbbells, which represent a simplified model of the polymer chains, in a Newtonian solvent.

As represented in figure 2.2, consider an isolated dumbbell, consisting of two beads of mass m_i and m_j whose interaction is represented by the force $\mathbf{F}$, and immersed in a Newtonian fluid at positions $\mathbf{x}_i$ and $\mathbf{x}_j$. The distance between the beads is denoted by $\boldsymbol{\delta} = \mathbf{x}_j - \mathbf{x}_i$. As detailed in [45], Larson [34] and Bird *et al.* [6] relate the extra-stress tensor defined in (2.18) to the ensemble average of the dyadic product $\boldsymbol{\delta}\mathbf{F}$ which is defined as the conformation tensor

$$\boldsymbol{\chi} = \langle\boldsymbol{\delta}\mathbf{F}\rangle. \tag{2.23}$$

The ensemble averaging enables the transition from the microscopic to the macroscopic description and thereby induces the loss of the information on the state of each dumbbell. In other words, the conformation tensor can be computed knowing the state of each dumbbell. However, knowing
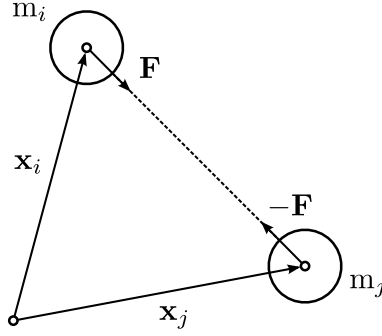
Fig. 2.2: The dumbbell model.

the conformation tensor does not allow to retrieve the state of the dumbbells since the ensemble-averaging operation erases this information.

In particular, the focus is put on the Oldroyd-B model which was first derived in the early 1950s [43] from a macroscopic viewpoint. Considering a linear Hookean spring which links the beads, the force is simply proportional to the gap from the equilibrium state, the proportionality constant being the stiffness of the spring. In this case, the governing equations can be expressed in terms of the conformation tensor by

$$\boldsymbol{\nabla} \cdot \boldsymbol{v} = 0, \tag{2.24}$$

$$\partial_t \boldsymbol{v} + \boldsymbol{\nabla} \cdot (\boldsymbol{v}\boldsymbol{v}) = \nu \boldsymbol{\nabla}^2 \boldsymbol{v} + \frac{\eta\nu}{\lambda} \boldsymbol{\nabla} \cdot \boldsymbol{\chi} + \rho^{-1}(\boldsymbol{g} - \boldsymbol{\nabla}p), \tag{2.25}$$

$$\partial_t \boldsymbol{\chi} + \boldsymbol{\nabla} \cdot (\boldsymbol{v}\boldsymbol{\chi}) = \boldsymbol{\nabla}\boldsymbol{v}^{\mathrm{T}} \cdot \boldsymbol{\chi} + \boldsymbol{\chi} \cdot \boldsymbol{\nabla}\boldsymbol{v} - \lambda^{-1}(\boldsymbol{\chi} - \boldsymbol{I}), \tag{2.26}$$

where λ is the stress-relaxation time, while the dimensionless parameter η represents the additional contribution of the polymers to the viscosity of the solution

$$\nu_{\mathrm{t}} = (1 + \eta)\nu. \tag{2.27}$$

In this particular case, the extra-stress tensor is related to the conformation tensor by the linear expression

$$\boldsymbol{\tau} = 2\mu\dot{\boldsymbol{\gamma}} + \lambda^{-1}(\boldsymbol{\chi} - \boldsymbol{I}), \tag{2.28}$$

where the first term is due to the Newtonian solvent, while the second one represents the additional stresses due to the polymer.

Considering that an ideal Hookean spring links the beads, the dumbbell can be infinitely stretched which induces an infinite linking force and unphysical predictions. Despite this major drawback and the major numerical issues encountered using this model, it is chosen because of its linearity with respect to the conformation tensor. This property allows to obtain analytical results such as those reported in chapter 6 which are particularly useful in a validation process.

More physically consistent models can be obtained from the same theory but imposing a more realistic interaction of the beads.

2.3.3   Dimensional analysis

The incompressible and isothermal Navier–Stokes equations derived in the Newtonian case (2.20)-(2.21) and for Oldroyd-B fluids (2.24)-(2.26) form a dimensional set of partial differential equations. The introduction of the corresponding sets of dimensionless equations allows to get insight

into the relative importance of the physical phenomena involved in the flow. As indicated by the Buckingham-Π theorem [40], the process of non-dimensionalization is not unique and depends on the definition of the dimensionless variables.

For instance, considering as references the length L, the velocity V and the inertial time L/V, the stresses are scaled by the dynamic pressure ρV^2 and the volume force by V^2/L. The introduction of these dimensionless variables into the Navier–Stokes equations (2.20)-(2.21) yields

$$\boldsymbol{\nabla} \cdot \boldsymbol{v} = 0, \tag{2.29}$$

$$\partial_t \boldsymbol{v} + \boldsymbol{\nabla} \cdot (\boldsymbol{vv}) = \mathrm{Re}^{-1}\boldsymbol{\nabla}^2 \boldsymbol{v} + \boldsymbol{g} - \boldsymbol{\nabla}p, \tag{2.30}$$

where the Reynolds number,

$$\mathrm{Re} = \frac{\mathrm{VL}}{\nu}, \tag{2.31}$$

is the ratio of inertia to viscous stresses which characterises a particular flow from a physical viewpoint. Moreover, the Reynolds number also measures the non-linear character of the equations since the convective term becomes dominant at large values.

Alternatively, considering as reference the diffusion-time L^2/ν, the stresses are scaled by $\rho\nu V/L$ and the equations (2.24)-(2.26) become

$$\boldsymbol{\nabla} \cdot \boldsymbol{v} = 0, \tag{2.32}$$

$$\partial_t \boldsymbol{v} + \mathrm{Re}\,\boldsymbol{\nabla} \cdot (\boldsymbol{vv}) = \boldsymbol{\nabla}^2 \boldsymbol{v} + \frac{\eta}{\mathrm{De}}\boldsymbol{\nabla} \cdot \boldsymbol{\chi} + \mathrm{Re}\,\boldsymbol{g} - \boldsymbol{\nabla}p, \tag{2.33}$$

$$\partial_t \boldsymbol{\chi} + \boldsymbol{\nabla} \cdot (\boldsymbol{v\chi}) = \boldsymbol{\nabla v}^{\mathrm{T}} \cdot \boldsymbol{\chi} + \boldsymbol{\chi} \cdot \boldsymbol{\nabla v} - \frac{1}{\mathrm{De}}(\boldsymbol{\chi} - \boldsymbol{I}), \tag{2.34}$$

where the Deborah number,

$$\mathrm{De} = \frac{\lambda \mathrm{V}}{\mathrm{L}}, \tag{2.35}$$

represents the ratio of the stress relaxation-time to the inertial time and thereby the importance of memory effects in the flow, that is the elasticity of the fluid. In this case, the non-linearity of the equations is proportional to both the Reynolds and Deborah numbers. Moreover, in order to fully characterise such fluid flows, the relative contribution of the polymers to the viscosity of the solution is required.

The Deborah number is a perfect illustration that everything flows, as quoted by Herakleitos of Ephesus. For large Deborah values, the inertial time L/V becomes small as compared to the stress relaxation-time. This means that the flow process stretches over a very long time period which could be too long to observe within a given time-scale. Such is the case of the formation of mountains or the movement of tectonic plates which are not observable in the time-scale of human life since they behave almost like perfectly elastic solids, that is with a relaxation time which tends to infinity.

2.4   Boundary and initial conditions

The mathematical models described above are not universal and are thus only valid to describe a particular range of events. Therefore, from a physical viewpoint, boundary conditions must be added to account for the interactions of this sub-domain of validity with the rest of the space-time. They are also introduced in order to restrict the size of the problem to a given sub-domain if the solution

is known on a given boundary. Boundary conditions are often associated to a constraint in space which results from the asymmetric description of the space-time adopted in classical mechanics.

Physical processes at the microscopic level are believed to be either entirely or mostly time symmetric, meaning that the theoretical statements that describe them remain true if the direction of time is reversed. However, at the macroscopic level, it often appears that there is an obvious direction of time. This implies that only initial conditions are imposed. From the relativistic viewpoint, the initial conditions must satisfy the boundary conditions to build a coherent event in the space-time.

For instance, consider the simplest case of a water flow in a pipe. Because of the assumptions considered for their derivation, the Navier–Stokes equations are only valid in the fluid domain. Boundary conditions are therefore required to describe the interaction between the fluid and the walls. Moreover, the relevant part of the physics to be studied in this framework is enclosed inside the pipe. Because of the fluid viscosity, the fluid sticks to the wall which allows to know the solution to impose on the boundaries of the fluid domain. Moreover, the boundary conditions must be supplemented by the initial state of the flow variables which is required to compute their time-evolution.

Considering the same problem for an Oldroyd-B fluid also requires to impose appropriate boundary conditions for the conformation tensor in order to obtain a well-posed problem, which still remains an open question. The reader may be referred to [45] for a discussion on this particular topic which extends beyond the limited scope of this work.

2.5 Large eddy simulation approximation

As compared to the macroscopic level, the coarser approximation introduced by the large eddy simulation relies on the computation of the large flow structures directly and the modelling of small ones. The basic idea is to consider that the large eddies are flow-dependent whereas the small structures have a more universal behaviour which enables them to be more easily modelled.

The scale separation is formally performed by filtering the equations which describe the dynamics at the macroscopic level. This operation requires the formal definition of the filtering operation as well as the introduction of the commutation operators.

2.5.1 Definition of the filter

A common way to express the removal of the small scales in large eddy simulation is to represent the filtering operation by a convolution product. The resolved part $\overline{u}(\boldsymbol{x}, t)$ of the space-time dependent field $u(\boldsymbol{x}, t)$ is formally defined by the relation

$$\overline{u}(\boldsymbol{x}, t) = \int_{-\infty}^{+\infty} u(\boldsymbol{x}', t') \, \mathcal{K}(\boldsymbol{x} - \boldsymbol{x}', t - t') \, d\boldsymbol{x}' dt', \tag{2.36}$$

where the convolution kernel $\mathcal{K}$ characterises the filter. Although some attempts were made in the field of the so-called temporal large eddy simulation, see for example Pruett *et al.* [48], the focus is put on large eddy simulations solely based on spatial filtering. In other words, time-filtering is assumed to be negligible which implies the use of a temporal discretization which captures all the time-scales of the flow. In this case, the general definition of the filtering operation (2.36) reduces to

$$\overline{u}(\boldsymbol{x}, t) = \int_{-\infty}^{+\infty} u(\boldsymbol{x}', t) \, \mathcal{K}(\boldsymbol{x} - \boldsymbol{x}') \, d\boldsymbol{x}', \tag{2.37}$$

which can also be written in the condensed form

$$\overline{u} = \mathcal{K} \star u, \tag{2.38}$$

where $\mathcal{K}\star$ is the operator describing the filtering operation (2.37), with the convolution kernel $\mathcal{K}$. The unresolved or subgrid part $\overline{u}'$ is defined as the complement

$$\overline{u}' = (\mathcal{I} - \mathcal{K}) \star u, \tag{2.39}$$

with the identity convolution kernel $\mathcal{I} = \delta(\boldsymbol{x} - \boldsymbol{x}')$ and δ the Dirac distribution, which satisfies the decomposition of the variable such that $u = \overline{u} + \overline{u}'$.

2.5.2 Fundamental properties of the filter

In order to be able to work on the equations after the application of a filter such as (2.37), the following properties are required.

Conservation of constants,

$$\int_{-\infty}^{+\infty} \mathcal{K}(\boldsymbol{x}) \, \boldsymbol{dx} = 1. \tag{2.40}$$

Linearity,

$$\overline{u + w} = \overline{u} + \overline{w}, \qquad \overline{cu} = c \, \overline{u}, \qquad c \in \mathbb{R}. \tag{2.41}$$

Commutation with differentiation,

$$\overline{\partial_{s_i} u} = \partial_{s_i} \overline{u}, \qquad \forall i. \tag{2.42}$$

The linearity property is automatically satisfied since the convolution product satisfies (2.41) independently of the convolution kernel.

2.5.3 Projection operators

An application $\mathcal{P}$ is defined as a projector if $\mathcal{P}^2 = \mathcal{P} \circ \mathcal{P} = \mathcal{P}$ which is idempotent since it satisfies the general relation

$$\mathcal{P}^n = \mathcal{P} \circ \mathcal{P} \circ \ldots \circ \mathcal{P} = \mathcal{P}, \qquad \forall n \in \mathbb{N}^+. \tag{2.43}$$

Such operators are of crucial importance in the case of the grid filter models introduced in this work.

However, the filters verifying the properties detailed in section 2.5.2 are not in general projective operators. In other words, this implies that

$$\overline{\overline{u}} = \mathcal{K} \star \circ \mathcal{K} \star u \neq \mathcal{K} \star u = \overline{u}. \tag{2.44}$$

When $\mathcal{K}\star$ is not projective, the filtering can be interpreted as a change of variable, can be inverted and induces no loss of information. The kernel of the application is then reduced to the null element, *i.e.* $\ker(\mathcal{K}\star) = \{0\}$.

2.5.4   Commutation operator

The derivation of the large eddy simulation equations in a general framework requires the use of the commutator and its properties are useful for the derivation of the subgrid models. Let f, g and h be three operators. The commutator of f and g applied to a given variable u is defined as

$$[f, g](u) = f \circ g(u) - g \circ f(u), \tag{2.45}$$

and satisfies the properties of skew-symmetry, Leibniz and Jacobi which are respectively given by

$$[f, g] + [g, f] = 0, \tag{2.46}$$

$$[f \circ g, h] - [f, h] \circ g - f \circ [g, h] = 0, \tag{2.47}$$

$$[f, [g, h]] + [g, [h, f]] + [h, [f, g]] = 0. \tag{2.48}$$

As an example, the Leibniz identity (2.47) is referred to as the multiplicative Germano identity in large eddy simulation and is applied for the computation of the subgrid viscosity constant in the dynamic version of the Smagorinsky model [20].

2.5.5   Filtered equations

A large class of governing equations, and for instance those considered for Newtonian fluids (2.20)-(2.21) and for Oldroyd-B fluids (2.24)-(2.26), can be recast in the generic form

$$\boldsymbol{M}\,\partial_t \boldsymbol{u} + \boldsymbol{A}(\boldsymbol{u}) = \boldsymbol{f}, \tag{2.49}$$

introducing $\boldsymbol{M}$ as a second-order mass tensor, identifying the unknown as $\boldsymbol{u} \equiv (p, \boldsymbol{v})$ in the Newtonian case and as $\boldsymbol{u} \equiv (p, \boldsymbol{v}, \boldsymbol{\chi})$ for Oldroyd-B. The operator $\boldsymbol{A}$ represents the corresponding differential operator in space and $\boldsymbol{f}$ the data which do not depend on the state of the system. As an example, considering the Navier-Stokes equations in either the Newtonian or Oldroyd-B case, the mass tensor can be illustrated by the block-matrix representation

$$\boldsymbol{M} = \begin{pmatrix} 0 & \boldsymbol{0} \\ \boldsymbol{0} & \boldsymbol{I} \end{pmatrix}. \tag{2.50}$$

The singularity of the mass tensor is due to the mass conservation equation which becomes a constraint in the incompressible case. Consequently, the pressure is not given by an evolution equation but is determined in order to constraint the velocity field to be solenoidal.

The large eddy simulation equations are obtained by applying the convolution filter $\mathcal{K}\star$ to the generic governing equations (2.49), which formally reads

$$\boldsymbol{M}\,\partial_t \overline{\boldsymbol{u}} + \overline{\boldsymbol{A}(\boldsymbol{u})} = \overline{\boldsymbol{f}}, \tag{2.51}$$

where the mass tensor is assumed to be constant in space. This equation may also be rewritten in the form

$$\boldsymbol{M}\,\partial_t \overline{\boldsymbol{u}} + \boldsymbol{A}(\overline{\boldsymbol{u}}) = \overline{\boldsymbol{f}} + [\boldsymbol{A}, \mathcal{K}\star](\boldsymbol{u}), \tag{2.52}$$

introducing the subgrid commutator

$$[\boldsymbol{A}, \mathcal{K}\star](\boldsymbol{u}) = \boldsymbol{A}(\overline{\boldsymbol{u}}) - \overline{\boldsymbol{A}(\boldsymbol{u})}. \tag{2.53}$$

The closure of the filtered equations (2.52) requires the subgrid commutator to be expressed in terms of the filtered field which reflects the required modelling of the subgrid scales and the interaction among all space-scales of the solution.

An illustration of subgrid commutator is obtained by filtering the Navier–Stokes equations in the Newtonian case

$$[\boldsymbol{A}, \mathcal{K}\star](\boldsymbol{u}) = \begin{pmatrix} 0 \\ \boldsymbol{\nabla} \cdot (\overline{\boldsymbol{v}}\ \overline{\boldsymbol{v}} - \overline{\boldsymbol{v}\boldsymbol{v}}) \end{pmatrix}. \tag{2.54}$$

The first term of the commutator vanishes by linearity of the equation of mass conservation (2.20), whereas the second contribution arise from the non-linear and non-commuting term of (2.21). In the case of the Oldroyd-B constitutive equation (2.26) which comprises three non-linear terms, the filtering operation produces an additional six-term contribution

$$[\boldsymbol{A}, \mathcal{K}\star](\boldsymbol{u}) = \begin{pmatrix} 0 \\ \boldsymbol{\nabla} \cdot (\overline{\boldsymbol{v}}\ \overline{\boldsymbol{v}} - \overline{\boldsymbol{v}\boldsymbol{v}}) \\ \boldsymbol{\nabla} \cdot (\overline{\boldsymbol{v}}\ \overline{\boldsymbol{\chi}} - \overline{\boldsymbol{v}\boldsymbol{\chi}}) - (\boldsymbol{\nabla}\overline{\boldsymbol{v}}^{\mathrm{T}} \cdot \overline{\boldsymbol{\chi}} + \overline{\boldsymbol{\chi}} \cdot \boldsymbol{\nabla}\overline{\boldsymbol{v}}) + (\overline{\boldsymbol{\nabla}\boldsymbol{v}^{\mathrm{T}} \cdot \boldsymbol{\chi}} + \overline{\boldsymbol{\chi} \cdot \boldsymbol{\nabla}\boldsymbol{v}}) \end{pmatrix}. \tag{2.55}$$

In section 1.2, a phenomenological characterisation of turbulence has been discussed. In the large eddy simulation framework, a turbulent flow can be defined as having a non-vanishing subgrid part which implies a non-vanishing subgrid commutator in the filtered equations. In other words, this means that the coarser level of approximation induces a loss of information which shall be at least partially retrieved in a modelling process.

2.6   Why turbulence?

From a physical viewpoint, incompressible and isothermal flows of Newtonian and Oldroyd-B fluids are mainly characterised by the dimensionless numbers of Reynolds and Deborah. As detailed in section 1.2, the onset of inertial and elastic turbulence occurs at high values of the Reynolds and the Deborah numbers which corresponds, from a mathematical viewpoint, to a strong non-linear character of the equations. Moreover, the commutator of the filtered equations arises from the non-linear terms of the governing equations.

As a matter of fact, turbulence appears as a paradigm of non-linearity which translates the reported quote by Werner Heisenberg about the origins of turbulence onto the origins of non-linearity. This link can be illustrated by the following trivial example. Consider the one-dimensional Burgers equation given by

$$\partial_t v = \nu\ \partial_x^2 v - v\ \partial_x v. \tag{2.56}$$

Assuming that the solution at a given time t reads

$$v = \cos(\mathrm{k}x), \tag{2.57}$$

where k is the wave-number, the time-derivative of the solution becomes

$$\partial_t v = -\nu \mathrm{k}^2 v + \frac{\mathrm{k}}{2} \sin(2\mathrm{k}x), \tag{2.58}$$

where the non-linear contribution gives rise to the growth of a term with double spatial frequency. This term will in turn generate higher frequency structures and thereby start an energy cascade process referred to as the Richardson cascade in fluid mechanics. The balance between the production of high frequencies and their dissipation only occurs at high wave-numbers depending on the value of the viscosity, as suggested by equation (2.58). More detailed considerations on this topic can be found in [33].

Despite its strong assimilation to fluid mechanics, the turbulence phenomenon is therefore expected to appear in any physical system which is governed by strongly non-linear equations.

Chapter 3

Numerical approximation of partial differential equations

After the definition of a model describing the dynamics of the system, the second issue involved in numerical simulation is the solution of the corresponding equations with appropriate algorithms and sufficient accuracy in order to preserve the level of precision required on the model. Since they are based on the continuous media mechanics, the Navier–Stokes equations and their filtered counterpart used for the large eddy simulation are systems of coupled partial differential equations. Their numerical solution requires the spatial discretization in order to retrieve a finite system of coupled differential and algebraic equations which can be numerically integrated in time.

The grid filter models which are briefly presented in the introduction and further detailed in chapter 4 rely on the interpretation of the coarser spatial discretization used for large eddy simulation as the only effective filter applied to the governing equations. As a consequence, subgrid modelling explicitly depends on the spatial discretization method. For the sake of generality, the aim is therefore to provide a general method for the computation of the grid filter associated with a large range of discretization methods and for the modelling of its effect on the computable scales of the solution. This requires the unified presentation of a large class of methods used for the spatial discretization of partial differential equations. The presentation is restricted to general and useful elements and the reader may be referred to [50] for more detailed aspects.

After this general presentation, the focus is put on the spectral/finite elements methods and the Fourier collocation method which are respectively used for the simulation of the lid-driven cubical cavity flow presented in chapter 5 and for the Kolmogorov flow in chapter 6. In both cases, suitable filtering techniques required for subgrid modelling in the case of the grid filter models are presented.

In order to solve the ordinary differential equations arising from the spatial discretization, the methods used in the simulations reported hereafter are only briefly presented since time-integration algorithms do not play any role for subgrid modelling in the case of the grid filter models, as assumed in equation (2.37).

3.1   General presentation

Classical methods used for the spatial discretization of partial differential equations, such as the finite volumes, the finite/spectral elements and the Fourier methods, are either implicitly or explicitly based on the definition of a finite dimensional space of basis functions in order to approximate the variables as a linear combination of the basis elements, often referred to as shape functions. The difference among these methods essentially relies on the definition of the basis and the formulation of the fundamental equations.

3.1.1   Formulation

A large class of partial differential equations systems can be written in the following form which is recalled from equation (2.49)

$$\boldsymbol{M}\ \partial_t \boldsymbol{u} + \boldsymbol{A}(\boldsymbol{u}) = \boldsymbol{f}, \tag{3.1}$$

also referred to as the strong formulation and which expresses the conservation and constitutive laws at the local scale. The methods based on this formulation are referred to as collocation methods.

The equations can also be expressed with an integral formulation which is obtained by the introduction of a scalar product with a test function $\boldsymbol{w}$ and by the integration over the whole domain, which yields

$$\int_{\boldsymbol{\Omega}} [\boldsymbol{M}\ \partial_t \boldsymbol{u} + \boldsymbol{A}(\boldsymbol{u})] \cdot \boldsymbol{w}\ dV = \int_{\boldsymbol{\Omega}} \boldsymbol{f} \cdot \boldsymbol{w}\ dV, \qquad \forall \boldsymbol{w}. \tag{3.2}$$

The methods relying on this formulation are referred to as weighted residual methods. Depending on the functional space to whom the test functions belong, different approaches can be defined. For instance, the Galerkin method is retrieved choosing the test functions in the same space as the shape functions. Moreover, an integration by parts is performed on the integral formulation in order to obtain the so-called weak formulation and thereby enlarge the functional space of the solution.

Alternatively, the equations can be expressed in the conservative formulation which is derived from the strong formulation by integration over the domain and using the divergence theorem in order to replace the volume integral of the spatial operator by a surface integral

$$\int_{\boldsymbol{\Omega}} \boldsymbol{M}\ \partial_t \boldsymbol{u}\ dV + \int_{\partial \boldsymbol{\Omega}} \boldsymbol{F}(\boldsymbol{u}) \cdot \boldsymbol{n}\ dS = \int_{\boldsymbol{\Omega}} \boldsymbol{f}\ dV, \tag{3.3}$$

where $\boldsymbol{F}(\boldsymbol{u})$ represents the fluxes of the variable through the boundary of the domain and which implies $\boldsymbol{A} = \boldsymbol{\nabla} \cdot \boldsymbol{F}$. This formulation is mostly used for the finite volumes and the discontinuous Galerkin methods. It can also be retrieved from the integral formulation (3.2) by imposing $\boldsymbol{w} = 1$, and be interpreted as a weak formulation since the maximum order of differentiation is lower as compared to (3.1).

3.1.2   Approximation bases

In order to discretize in space the governing equations expressed in either the strong, integral, weak or conservative formulations, usual methods rely on the definition of a space of basis functions

$$\mathbb{F} = \{\phi_1, \phi_2, \dots, \phi_{\mathrm{q}}, \dots\} \tag{3.4}$$

defined in the domain in such a way that any variable can be expressed as a linear combination in this space. Considering a single spatial dimension for the sake of conciseness and without major loss of generality, such an expansion can be written in the form

$$u(x,t) = \sum_{j=1}^{\infty} \underline{u}_j(t)\phi_j(x) = \sum_{j=1}^{\mathrm{q}} \underline{u}_j(t)\phi_j(x) + \varepsilon_x(x,t,\mathrm{q}), \tag{3.5}$$

where ε_x and $\underline{u}_j$ represent the truncation error at order q and the modal coefficient of the expansion associated with the basis function of order j. The difference among all the numerical methods is related to the spatial dependence of the basis functions. For instance and as illustrated in figure 3.1,
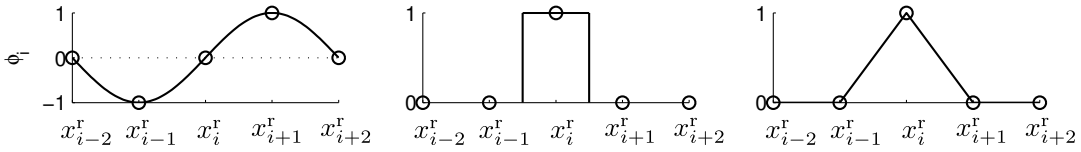
Fig. 3.1: Approximation bases associated to the Fourier methods (left), finite volumes (centre) and linear finite/spectral elements (right).

the finite volumes method uses piecewise constant functions, the finite and spectral elements use Lagrange polynomials of variable degree, while Fourier methods use a hierarchical set of trigonometric functions.

In the framework of a direct numerical simulation, the choice of the truncation parameter is a crucial issue. From a purely mathematical viewpoint, the truncation order should tend to infinity in order to obtain the exact solution of the governing equations. However, due to the limited computational resources available, only a finite number of modes can be retained in order to achieve the computation in a finite time. Moreover, if the relevant structures of the flow dynamics extend to an infinitely small scale, the Navier–Stokes model which is based on the continuous media mechanics is no more applicable.

Hence, the truncation parameter is chosen based on the following criteria. First, the relevant flow structures must be represented. In the Newtonian case, this range extends from the large eddies of the flow to the so-called Kolmogorov length-scale, that is to the structures which are mainly responsible for the energy dissipation. Second, the truncation order must be chosen in order to guarantee the numerical stability of the global solution algorithm. And third, the truncation error (3.5) must remain negligible at all times as compared to the represented part of the variable. The quality of a direct numerical simulation is certainly and closely related to the arbitrary definition of this criteria.

In any case, assuming that these constraints are well-defined and satisfied allows to introduce the approximation

$$u(x,t) \simeq \sum_{j=1}^{q} \underline{u}_j(t)\phi_j(x), \tag{3.6}$$

where q can be a variable parameter depending on the state of the system when considering adaptive spatial discretizations. Using the approximation (3.6) and defining a set of r interpolation points distributed inside the computational domain

$$\mathbb{X}_r = \{x_1^r, x_2^r, \ldots, x_r^r\}, \qquad x_i^r \in \Omega, \ \forall i \in \{1, \ldots, r\}, \tag{3.7}$$

allows to express the value of the variable on each point as

$$\mathrm{u}_i(t) = u(x_i^r, t) = \sum_{j=1}^{q} \underline{u}_j(t)\phi_j(x_i^r), \tag{3.8}$$

which are referred to as the nodal values. They can also be formulated using the following vector expression

$$\mathbf{u} = \mathbf{\Phi}_q^r \underline{\mathbf{u}}, \qquad (\mathbf{\Phi}_q^r)_{ij} = \phi_j(x_i^r), \tag{3.9}$$

which represents the transformation operation of the variable between physical and modal spaces. As suggested by equation (3.9), this transformation is bijective and can be inverted if the number

of basis functions in the linear combination equals the number of interpolation points in physical space in such a way that the transformation matrix be square. Moreover, the transformation matrix must be regular which implies the linear independence of the basis functions. In this case, the modal coefficients can be obtained from the nodal values by the inverse operation

$$\underline{\mathbf{u}} = (\mathbf{\Phi}_{\mathrm{q}}^{\mathrm{q}})^{-1}\mathbf{u} = \underline{\mathbf{\Phi}}_{\mathrm{q}}^{\mathrm{q}}\mathbf{u}, \tag{3.10}$$

thereby implicitly introducing the shorthand notation

$$\underline{\mathbf{\Phi}}_{\mathrm{q}}^{\mathrm{q}} = (\mathbf{\Phi}_{\mathrm{q}}^{\mathrm{q}})^{-1}. \tag{3.11}$$

3.1.3   Semi-discrete equations

The spatial discretization is performed by introducing the approximation (3.6) into equations (3.1), (3.2) or (3.3). For any of these formulations, the resulting space-discretized equations can be written in the generic vector form

$$\underline{\mathbf{M}}\,\underline{\dot{\mathbf{u}}} + \underline{\mathbf{A}}\,\underline{\mathbf{u}} = \underline{\mathbf{M}}\,\underline{\mathbf{f}}. \tag{3.12}$$

where the upper dot represents a time-derivative and which forms a finite set of differential and algebraic equations for the modal coefficients. The operator $\underline{\mathbf{A}}$ represents in modal space the discretized version of the differential operator $\boldsymbol{A}$ which depends on the discrete unknown $\underline{\mathbf{u}}$ for non-linear equations, while $\underline{\mathbf{M}}$ is the discrete and modal mass operator.

In a second step, the set of equations arising from the spatial discretization has to be integrated in time to compute the evolution of the system. This operation is detailed in section 3.4. However, if a steady-state solution is sought, equation (3.12) reduces to the following set of fully algebraic equations

$$\underline{\mathbf{A}}\,\underline{\mathbf{u}} = \underline{\mathbf{M}}\,\underline{\mathbf{f}}, \tag{3.13}$$

which may be non-linear and solved using appropriate algorithms.

3.2   Finite and spectral elements methods

According to the previous presentation, the definition of a particular discretization method essentially relies on the choice of the shape and test functions and the use of a particular formulation of the governing equations.

In this section, the aim is to give some useful details about the finite and spectral elements methods which form a family of approximation schemes based on the Galerkin method, and usually on the weak formulation of the problem. The reader is referred to specialised monographs such as [17, 22] for further details.

3.2.1   Approximation basis

The basis is presented in its one-dimensional version, the extension to three dimensions being straightforward by tensor product. It is built up on a reference parent element $\hat{\Omega}$ in such a way that

$$u(\xi, t) \simeq \sum_{j=1}^{\mathrm{q}} \underline{\mathbf{u}}_j(t)\psi_j(\xi), \qquad \xi \in \hat{\Omega} = [-1, 1], \tag{3.14}$$

and the basis functions are defined as Lagrange polynomials

$$\psi_j(\xi) = \prod_{i=1, i\neq j}^{q} \frac{\xi - \xi_i^q}{\xi_j^q - \xi_i^q}, \tag{3.15}$$

which require the introduction of a set of q interpolation points $\hat{\mathbb{X}}_q = \{\xi_i^q\}$ inside the parent element for their definition.

In the case of the finite elements, the points are evenly distributed in the parent element, which reads

$$\hat{\mathbb{X}}_q^f = \{\xi_i^q\} = \{\xi \mid (1+\xi) - 2\tfrac{i-1}{q-1} = 0\}, \qquad \xi \in \hat{\Omega}. \tag{3.16}$$

For the spectral elements, the set of points is chosen as the Gauss–Lobatto–Legendre nodes which are given by the solutions of the equation

$$\hat{\mathbb{X}}_q^s = \{\xi_i^q\} = \{\xi \mid (1-\xi^2)\partial_\xi L_{q-1}(\xi) = 0\}, \qquad \xi \in \hat{\Omega}, \tag{3.17}$$

where $\partial_\xi L_{q-1}$ is the first-order derivative of the Legendre polynomial of degree $q-1$. The difference on the set of interpolation points engenders two different bases which can be qualitatively compared in figure 3.2.
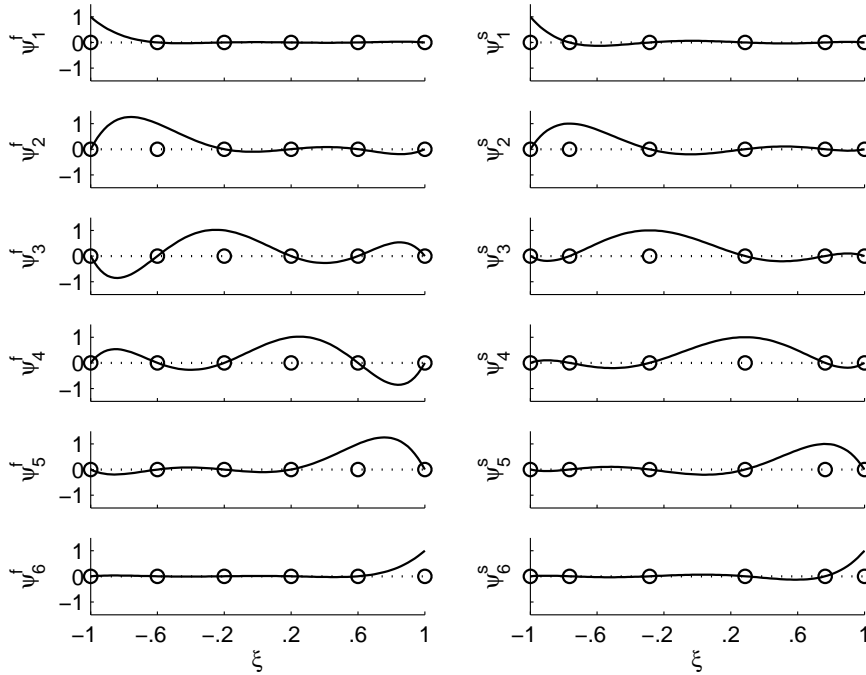

Fig. 3.2: Lagrangian bases associated to the finite (left) and spectral (right) elements shown on the parent element $\hat{\Omega}$ with the respective interpolation points and q = 6.

According to equation (3.15), the use of Lagrangian basis functions generally imposes the so-called cardinality property

$$(\mathbf{\Psi}_q^q)_{ij} = \psi_j(\xi_i^q) = \delta_{ij}, \tag{3.18}$$

which can also be observed in figure 3.2 and which means that the nodal and modal coefficients are equal, that is

$$\mathbf{u} = \underline{\mathbf{u}}. \tag{3.19}$$

The Lagrange basis is therefore a nodal and not a modal basis. Consequently, the integration of the system of differential and algebraic equations (3.12) provides the approximate solution of the problem at the discretization points without the need to perform any transformation from modal space. In other words, equation (3.12) is strictly equivalent to

$$\mathbf{M}\dot{\mathbf{u}} + \mathbf{A}\mathbf{u} = \mathbf{M}\mathbf{f}. \tag{3.20}$$

3.2.2   Semi-discrete equations

Introducing the discrete divergence and gradient operators respectively represented by $\mathbf{D}$ and $\mathbf{D}^{\mathrm{T}}$, the Navier–Stokes equations for Newtonian fluids (2.20)-(2.21) can be formally written in the form

$$\begin{pmatrix} \mathbf{M} & \mathbf{0} \\ \mathbf{0} & \mathbf{0} \end{pmatrix} \begin{pmatrix} \dot{\mathbf{v}} \\ \dot{\mathbf{p}} \end{pmatrix} + \begin{pmatrix} \mathbf{A} & \mathbf{D}^{\mathrm{T}} \\ \mathbf{D} & \mathbf{0} \end{pmatrix} \begin{pmatrix} \mathbf{v} \\ \mathbf{p} \end{pmatrix} = \begin{pmatrix} \mathbf{M}\mathbf{f} \\ \mathbf{0} \end{pmatrix}, \tag{3.21}$$

which is not a set of ordinary differential equations but a set of differential and algebraic equations since the mass operator is singular. This system can not be solved using standard time-integration techniques which implies to decouple the computation of the velocity and the pressure. The decoupling is presented in a two-step procedure. First, applying the constraint arising from the mass conservation to the equation of momentum conservation yields the decoupled algebraic system

$$\begin{pmatrix} \mathbf{M} & \mathbf{0} \\ \mathbf{D} & \mathbf{D}\mathbf{M}^{-1}\mathbf{D}^{\mathrm{T}} \end{pmatrix} \begin{pmatrix} \check{\mathbf{v}} \\ \mathbf{p} \end{pmatrix} = \begin{pmatrix} \mathbf{A}\mathbf{v} \\ \mathbf{D}\mathbf{f} \end{pmatrix}, \tag{3.22}$$

where $\check{\mathbf{v}}$ is an intermediate velocity field and which allows to compute the pressure in such a way to maintain the velocity field solenoidal. In a second step, the time-integration of the system is performed using

$$\mathbf{M}\dot{\mathbf{v}} + \mathbf{D}^{\mathrm{T}}\mathbf{p} = \mathbf{M}(\mathbf{f} - \check{\mathbf{v}}), \tag{3.23}$$

which is of the required form (3.12) with an invertible mass operator. However, the Poisson-type equation for the pressure in (3.22) is elliptic and requires the introduction of boundary conditions to be solved. In order to overcome this issue, the usual algorithms, such as the Uzawa or the projection methods [17], rely on the decoupling of the fully discretized equations following the same strategy as the one presented here on the semi-discrete problem.

3.2.3   Filtering

As already discussed by Habisreutinger *et al.* in [25], filtering techniques suited to the finite and spectral elements methods must be applicable at the element-level. Moreover, for mathematical consistency reasons, the C^0-continuity of the filtered variables across the elements is required.

For the finite and spectral elements methods, performing the filtering operations in the Lagrangian basis (3.15) would therefore seem a rather straightforward and natural choice. However, this basis is nodal, *i.e.* not modal, and all the basis functions represent spatial structures of the same size. Consequently, this choice would not allow to directly and independently act on a given range of space-scales as required for a filtering operation.

In order to overcome this issue and satisfy the previous constraints, the filtering process requires the use of an auxiliary polynomial basis whose elements form a hierarchical set of functions

representing different length-scales. The filtering operations are therefore performed in a modal polynomial basis which was proposed in the framework of the finite elements method and first used by Boyd [12] as a filtering technique. The modal basis is built up on the reference parent element $\hat{\Omega}$ as

$$\phi_1 = \frac{1 - \xi}{2}, \qquad \phi_2 = \frac{1 + \xi}{2},$$
$$\phi_j = L_{j-1}(\xi) - L_{j-3}(\xi), \qquad 3 \leq j \leq q, \tag{3.24}$$

where L_j is the Legendre polynomial of degree j. As illustrated in figure 3.3 and unlike the Lagrangian nodal basis, this one forms a hierarchical set of polynomials allowing to define in an explicit and straightforward manner a filtering operation. It is performed in the modal polynomial space through a filtering matrix $\underline{\mathbf{K}}$, characterising a the convolution filter $\mathcal{K}\star$. The filtering process
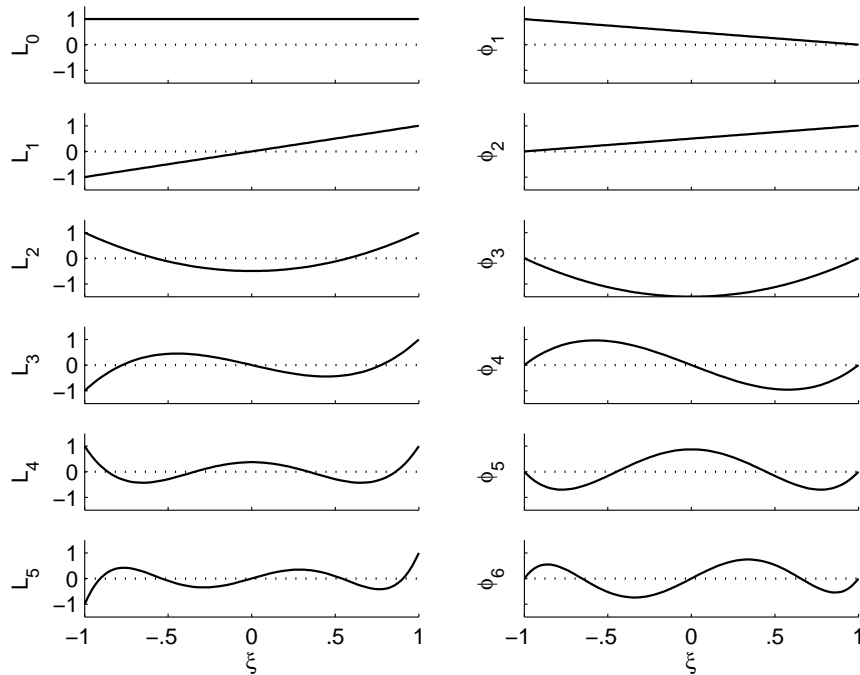

Fig. 3.3: The Legendre (left) and the modal polynomials (right) shown on the parent element $\hat{\Omega}$ with q = 6.

is presented in its one-dimensional version, the extension to three dimensions being straightforward by tensor product, and reads

$$\overline{\mathbf{u}} = \mathbf{K}\mathbf{u} = \mathbf{\Phi}_q^q \, \underline{\mathbf{K}} \, \underline{\mathbf{\Phi}}_q^q \, \mathbf{u}. \tag{3.25}$$

The original variable is first sent from the nodal basis to the modal one, then filtered using the modal filtering matrix and finally brought back to the nodal basis. It is worth noticing that the transform matrix $\mathbf{\Phi}_q^q$ depends on the distribution of interpolation points in the parent element $\hat{\mathbb{X}}_q$. This matrix is therefore not the same for the finite and spectral elements since the corresponding interpolation points are respectively given by equations (3.16) and (3.17).

The C^0-continuity of the filtered variables is preserved if and only if the filter does not affect the values at the boundaries of the elements. As it can be noticed in figure 3.3, the only basis functions having non-zero contributions at the boundaries are ϕ_1 and ϕ_2. As a consequence, in order to

guarantee the C^0-continuity across the elements, the filtering matrix must satisfy the property

$$\underline{\mathrm{K}}_{ij} = \delta_{ij}, \qquad \forall i \leq 2. \tag{3.26}$$

3.3   Fourier collocation method

The Fourier collocation method relies on the strong formulation of the problem and the use of complex trigonometric basis functions for the expression of the variables. Like in the case of the finite and spectral elements, the presentation is restricted to the useful concepts and the reader is referred to [14] for more details.

3.3.1   Approximation basis

The basis functions are defined in a global way over a fully periodic domain $\boldsymbol{\Omega} = [0, \mathrm{L}[^\mathrm{d}$, where L represents its size and d the number of spatial dimensions. Restricting the presentation to the one-dimensional case, the generalisation to the multi-dimensional one being straightforward by tensor product properties, the basis functions are given by

$$\phi_j = \cos(\mathrm{k}_j x) + \mathrm{i}\sin(\mathrm{k}_j x) = \mathrm{e}^{\mathrm{ik}_j x}, \tag{3.27}$$

with the imaginary number $\mathrm{i} = \sqrt{-1}$ and the wave-number k_j associated to the basis function j defined as

$$\mathrm{k}_j = \frac{2\pi j}{\mathrm{L}}, \qquad j \in \mathbb{Z}, \tag{3.28}$$

which is quantified in order to only retain the periodic functions over the length of the domain. The variables are therefore expanded into discrete Fourier series, which reads

$$u(x,t) \simeq \sum_{j=-\mathrm{q}/2}^{\mathrm{q}/2-1} \underline{u}_\mathrm{k}(t)\mathrm{e}^{\mathrm{ik}_j x}, \tag{3.29}$$

where the shorthand notation $\underline{u}_\mathrm{k} \equiv \underline{u}_j$ is used considering the bijection between the wave-number k_j and the index j. The interpolation points in physical space are uniformly distributed and given by

$$\mathbb{X}_\mathrm{q}^\mathrm{F} = \{x_i^\mathrm{q}\} = \{x \mid \tfrac{x}{\mathrm{L}} - \tfrac{i-1}{\mathrm{q}} = 0\}, \qquad x \in \Omega, \qquad i \in \{1, \dots, \mathrm{q}\}. \tag{3.30}$$

Real-valued functions in physical space such as those expected in this framework have to abide to the symmetry property

$$\underline{u}_\mathrm{k} = \underline{u}_{-\mathrm{k}}^*, \tag{3.31}$$

where the star denotes the complex conjugate value, in such a way that the imaginary parts of the sum (3.29) cancel out two by two. This also shows that modes go in pairs of opposite signs to represent the phase and thus the number of space-scales that are represented is actually divided by two.

In this formalism, the derivative of a function reduces to the single multiplication by the corresponding wave-number

$$\partial_x u(x,t) \simeq \sum_{j=-\mathrm{q}/2}^{\mathrm{q}/2-1} \mathrm{ik}_j \underline{u}_\mathrm{k}(t)\mathrm{e}^{\mathrm{ik}_j x}, \tag{3.32}$$

which means that the modal differentiation operator $\underline{\mathbf{D}}^\mathrm{T}$ is diagonal, thereby leading to considerable simplifications. Indeed, for linear differential operators, the resulting semi-discrete equations are decoupled in modal space, which once again showcases the close link of non-linearity and turbulence.

3.3.2 Semi-discrete equations

Since the modal coefficients are decoupled for linear differential operators, the semi-discrete counterpart of the Navier–Stokes equations (2.20)-(2.21) can be written for each modal coefficient as

$$\dot{\underline{v}}_{\mathbf{k}} + i\mathbf{k} \cdot \underline{\mathbf{vv}}_{\mathbf{k}} = -\mathrm{Re}^{-1}\mathbf{k}^2\underline{v}_{\mathbf{k}} + \underline{g}_{\mathbf{k}} - i\mathbf{k}\underline{p}_{\mathbf{k}}, \tag{3.33}$$

$$i\mathbf{k} \cdot \underline{v}_{\mathbf{k}} = \mathbf{0}, \tag{3.34}$$

where $\mathbf{k}$ is a wave-vector. In this case, the modal coefficients are coupled by the non-linear contribution in the momentum equations. This non-linear product is obtained by a pseudo-spectral approach as detailed by Orszag in [44]. The multiplications are actually performed in physical space and the product is transformed back to modal space, that is

$$\underline{\mathbf{vv}} = \underline{\boldsymbol{\Phi}}_{\mathrm{q}}^{\mathrm{q}}(\boldsymbol{\Phi}_{\mathrm{q}}^{\mathrm{q}}\underline{v} \cdot \boldsymbol{\Phi}_{\mathrm{q}}^{\mathrm{q}}\underline{v}). \tag{3.35}$$

In order to avoid the aliasing errors associated with the straightforward use of this method, a generalisation of the three-half rule presented in [14] is considered and expressed by the relation

$$\underline{\mathbf{vv}} = \underline{\mathbf{G}}_{\mathrm{r}}^{\mathrm{q}}\underline{\boldsymbol{\Phi}}_{\mathrm{r}}^{\mathrm{r}}(\boldsymbol{\Phi}_{\mathrm{q}}^{\mathrm{r}}\underline{v} \cdot \boldsymbol{\Phi}_{\mathrm{q}}^{\mathrm{r}}\underline{v}). \tag{3.36}$$

The variables are first evaluated in physical space on r points from the modal space of size q. Then, the product is transferred back to a modal space of size r and is finally projected through the rectangular matrix $\underline{\mathbf{G}}_{\mathrm{r}}^{\mathrm{q}}$, of size (q,r), with

$$(\underline{\mathbf{G}}_{\mathrm{r}}^{\mathrm{q}})_{ij} = \delta_{ij}, \tag{3.37}$$

onto the modal space of size q, thereby cutting off the additional high-frequency modes. The formal definition of this operation is presented in chapter 4. In practice, the parameter r is chosen as

$$3\mathrm{q}/2 \leq \mathrm{r} \leq 2\mathrm{q}, \tag{3.38}$$

the standard three-half rule being recovered for the lowest value. Since multiplying two functions with the same frequency generates a product of doubled frequency, as illustrated in equation (2.58), it is useless to choose r > 2q, which motivates the choice of the upper limit.

Like the system (3.21), equations (3.33)-(3.34) form a set of differential and algebraic equations. But applying the constraint arising from the mass conservation principle to the momentum equation allows to obtain the following Poisson-type equation for the pressure

$$\underline{p}_{\mathbf{k}} = \frac{1}{\mathbf{k}^2}i\mathbf{k} \cdot (i\mathbf{k} \cdot \underline{\mathbf{vv}}_{\mathbf{k}} - \underline{g}_{\mathbf{k}}), \tag{3.39}$$

which is equivalent to the pressure equation in (3.22). However, in this case, the periodic boundary conditions allow for a straightforward solution of this equation and the elimination of the pressure term in (3.33). Thus, the problem that remains is a system of ordinary differential equations which can be solved using standard techniques.

The corresponding set of equations for the Oldroyd-B constitutive model is obtained using the same strategy but starting from equations (2.32)-(2.34)

$$\dot{\underline{v}}_{\mathbf{k}} + \mathrm{Re}\, i\mathbf{k} \cdot \underline{\mathbf{vv}}_{\mathbf{k}} = -\mathbf{k}^2\underline{v}_{\mathbf{k}} + \frac{\eta}{\mathrm{De}}i\mathbf{k} \cdot \underline{\boldsymbol{\chi}}_{\mathbf{k}} + \mathrm{Re}\,\underline{g}_{\mathbf{k}} - i\mathbf{k}\underline{p}_{\mathbf{k}}, \tag{3.40}$$

$$\dot{\underline{\boldsymbol{\chi}}}_{\mathbf{k}} + i\mathbf{k} \cdot \underline{\mathbf{v\chi}}_{\mathbf{k}} = \underline{\boldsymbol{\gamma}^{\mathrm{T}} \cdot \boldsymbol{\chi}}_{\mathbf{k}} + \underline{\boldsymbol{\chi} \cdot \boldsymbol{\gamma}}_{\mathbf{k}} - \frac{1}{\mathrm{De}}(\underline{\boldsymbol{\chi}}_{\mathbf{k}} - \underline{\mathbf{I}}_{\mathbf{k}}), \tag{3.41}$$

$$\underline{p}_{\mathbf{k}} = \frac{1}{\mathbf{k}^2}i\mathbf{k} \cdot (i\mathbf{k} \cdot \underline{\mathbf{vv}}_{\mathbf{k}} - i\mathbf{k} \cdot \underline{\boldsymbol{\chi}}_{\mathbf{k}} - \mathrm{Re}\,\underline{g}_{\mathbf{k}}), \tag{3.42}$$

with the velocity gradient $\boldsymbol{\gamma} = \boldsymbol{\nabla}\boldsymbol{v}$ also evaluated in the Fourier basis.

3.3.3 Filtering

In the case of the Fourier collocation method, the basis used to express the variables already forms a hierarchical set of functions representing scales of different size. The filtering operations are therefore directly performed in this basis without the need to resort to an auxiliary basis as required for the finite and spectral elements. Thus, the filtering process formally reads

$$\overline{\mathbf{u}} = \mathbf{K}\mathbf{u} = \mathbf{\Phi}_{\mathrm{q}}^{\mathrm{q}} \, \underline{\mathbf{K}} \, \underline{\mathbf{\Phi}}_{\mathrm{q}}^{\mathrm{q}} \, \mathbf{u}, \tag{3.43}$$

where the modal filtering matrix $\underline{\mathbf{K}}$ characterises the filter. This definition is formally equivalent to (3.25) but the transformation matrices are built-up with the Fourier basis functions instead of the modal polynomials. However, this is the occasion to explicitly express the link between the modal and the nodal filters which is implicitly defined in the last equation

$$\mathbf{K} = \mathbf{\Phi}_{\mathrm{q}}^{\mathrm{q}} \, \underline{\mathbf{K}} \, \underline{\mathbf{\Phi}}_{\mathrm{q}}^{\mathrm{q}}, \tag{3.44}$$

$$\underline{\mathbf{K}} = \underline{\mathbf{\Phi}}_{\mathrm{q}}^{\mathrm{q}} \, \mathbf{K} \, \mathbf{\Phi}_{\mathrm{q}}^{\mathrm{q}}. \tag{3.45}$$

Despite its presentation in the framework of the filtering operation, the transformation rules between the modal and the nodal forms are valid for any type of operator. Furthermore, they will be generalised to the case of projective operators in chapter 4.

3.4 Time-integration

In order to compute the temporal evolution of the system, the semi-discrete equations (3.12) which form a set of ordinary differential equations shall be solved numerically. Since the large eddy simulations considered in this work only rely on spatial filtering, as assumed in equation (2.37), the grid filter models do not depend on the temporal discretization but solely on the spatial discretization. Therefore, the algorithms used in the simulations reported hereafter, that is the backward differentiation formulae and the Runge–Kutta methods, are only briefly described without the need to resort to a unified presentation. For instance, more detailed considerations can be found in [26, 49].

3.4.1 Backward differentiation formulae

The large eddy simulations of the lid-driven cavity flow presented in chapter 5 are performed using implicit backward differentiation formulae. Applying these algorithms on the semi-discrete equations (3.12) gives the multi-step method

$$\mathbf{M}(\beta_0 \mathbf{u}_{n+1} + \beta_1 \mathbf{u}_n + \ldots + \beta_{\mathrm{s}} \mathbf{u}_{n+1-\mathrm{s}}) = \Delta t (\mathbf{M}\mathbf{f}_{n+1} - \mathbf{A}\mathbf{u}_{n+1}). \tag{3.46}$$

where s and n represent the order of the method and the time-level. More precisely,

$$\mathbf{u}_n = \mathbf{u}(t_n) = \mathbf{u}(t_0 + n\Delta t), \tag{3.47}$$

where t_0 and Δt are the initial time and the typical time-sampling interval. In this framework, the choice of the order and the time-sampling directly defines the accuracy and the stability properties of the method. The reader is referred to the monograph by Deville *et al.* [17] for more detailed aspects on this topics.

3.4.2   Runge–Kutta methods

The simulations of viscoelastic fluid flows reported in chapter 6 are performed using Runge–Kutta methods with adaptive time-step.

Considering a general system of the form (3.12) which only includes differential equations, and which has therefore an invertible mass operator, the system can be recast into the generic form

$$\dot{\mathbf{u}} = \mathbf{h}(\mathbf{u}, t) = \mathbf{M}^{-1}(\mathbf{Mf} - \mathbf{Au}). \tag{3.48}$$

Using this expression, the Runge–Kutta methods can be expressed by the general formulation

$$\mathbf{u}_{n+1} = \mathbf{u}_n + \Delta t\, \mathbf{i}(\mathbf{u}_n, t_n, \Delta t, \mathbf{h}), \tag{3.49}$$

where the increment function is given by

$$\mathbf{i} = \sum_{i=1}^{s} b_i \mathbf{w}_i, \tag{3.50}$$

$$\mathbf{w}_i = \mathbf{h}(\mathbf{u}_n + \Delta t \sum_{j=1}^{s} a_{ij} \mathbf{w}_j, t_n + c_i \Delta t). \tag{3.51}$$

Hence, a given method is completely defined by the number of sub-steps s, and the coefficients a_{ij}, b_i, c_i which are usually summarised in the so-called Butcher table

$$
\begin{array}{c|c}
c_i & a_{ij} \\
\hline
 & b_i
\end{array}
\quad \equiv \quad
\begin{array}{c|cccc}
c_1 & a_{11} & a_{12} & \ldots & a_{1s} \\
c_2 & a_{21} & a_{22} & \ldots & a_{2s} \\
\vdots & \vdots & & \ddots & \vdots \\
c_k & a_{s1} & a_{s2} & \ldots & a_{ss} \\
\hline
 & b_1 & b_2 & \ldots & b_s
\end{array}
\tag{3.52}
$$

Three classes of Runge–Kutta methods can be distinguished. If the matrix of the coefficients a_{ij} is upper-triangular and has null diagonal coefficients, each $\mathbf{w}_i$ can be explicitly computed as a function of those already known. The method becomes diagonally implicit if the diagonal coefficients are not null which implies the solution of s non-linear equations of the form

$$\mathbf{w}_i = \mathbf{h}(\mathbf{u}_n + \Delta t \sum_{j=1}^{i} a_{ij} \mathbf{w}_j, t_n + c_i \Delta t), \tag{3.53}$$

while a non-linear system of dimension s has to be solved in the general and fully implicit case.

Since the Runge–Kutta schemes are single-step methods, the dynamic adaptation of the time-step is straightforward if the local integration error can be efficiently estimated. Standard strategies are based on the *a posteriori* estimation of the error using two Runge–Kutta schemes having the same number of steps but a different order of accuracy. If both methods have the same coefficients a_{ij} and c_i, the $\mathbf{w}_i$ are the same and no additional functional evaluations are required. Since only the coefficients b_i are different, the coupled method is represented by the augmented Butcher table

$$
\begin{array}{c|c}
c_i & a_{ij} \\
\hline
 & b_i \\
 & \tilde{b}_i \\
\hline
 & \tilde{e}_i
\end{array}
\tag{3.54}
$$

with $\tilde{e}_i = b_i - \tilde{b}_i$. The difference between both increment functions gives an estimate of the local integration error which is given by

$$\epsilon_t = \Delta t \sum_{i=1}^{s} \tilde{e}_i \mathbf{w}_i. \tag{3.55}$$

Different strategies used to adapt the time-step as a function of the estimated integration error are described in [26].

3.5   Velocity-pressure decoupling

Considering non-periodic domains, the pressure equation in (3.22) is difficult to solve since it requires the introduction of boundary conditions. In order to overcome this issue, the velocity-pressure decoupling is performed on the fully discretized equations. For instance, using the backward differentiation formulae, the fully discrete system corresponding to (3.21) can be formally written in the form

$$\left(\begin{array}{cc} \mathbf{H} & \mathbf{D}^{\mathrm{T}} \\ \mathbf{D} & \mathbf{0} \end{array} \right) \left(\begin{array}{c} \mathbf{v} \\ \mathbf{p} \end{array} \right)_{n+1} = \left(\begin{array}{c} \mathbf{Mf} \\ \mathbf{0} \end{array} \right)_{n+1}, \tag{3.56}$$

where the source term on the right-hand side is redefined in order to include all known contributions coming from the left-hand side of (3.46). In this particular case, the so-called Helmholtz operator reads

$$\mathbf{H} = \frac{\beta_0}{\Delta t} \mathbf{M} + \mathbf{A}. \tag{3.57}$$

In order to carry out the decoupling-error study, the previous formulation is generalised by the introduction of an arbitrary operator $\mathbf{Q}$ which yields

$$\left(\begin{array}{cc} \mathbf{H} & \mathbf{HQD}^{\mathrm{T}} \\ \mathbf{D} & \mathbf{0} \end{array} \right) \left(\begin{array}{c} \mathbf{v} \\ \mathbf{p} \end{array} \right)_{n+1} = \left(\begin{array}{c} \mathbf{Mf} \\ \mathbf{0} \end{array} \right)_{n+1} + \left(\begin{array}{c} \mathbf{Mr} \\ \mathbf{0} \end{array} \right)_{n+1}. \tag{3.58}$$

The term $\mathbf{r}$ is a residual accounting for the difference between (3.56) and (3.58), and it will be discarded in the sequel. Like for (3.22), the solution of the block decomposition of (3.58) is presented in a two-step procedure

$$\left(\begin{array}{cc} \mathbf{H} & \mathbf{0} \\ \mathbf{D} & \mathbf{DQD}^{\mathrm{T}} \end{array} \right) \left(\begin{array}{c} \check{\mathbf{v}} \\ \mathbf{p} \end{array} \right)_{n+1} = \left(\begin{array}{c} \mathbf{Mf} \\ \mathbf{0} \end{array} \right)_{n+1}, \tag{3.59}$$

and

$$\left(\begin{array}{cc} \mathbf{I} & \mathbf{QD}^{\mathrm{T}} \\ \mathbf{0} & \mathbf{I} \end{array} \right) \left(\begin{array}{c} \mathbf{v} \\ \mathbf{p} \end{array} \right)_{n+1} = \left(\begin{array}{c} \mathbf{M}\check{\mathbf{v}} \\ \mathbf{p} \end{array} \right)_{n+1}. \tag{3.60}$$

The intermediate velocity $\check{\mathbf{v}}$ is not divergence-free. The second step (3.60) performs the projection to obtain a divergence-free velocity. The system (3.59)–(3.60) covers a large class of so-called projection techniques depending on the choice of $\mathbf{Q}$. Choosing

$$\mathbf{Q} = \mathbf{H}^{-1}, \tag{3.61}$$

allows to recover the Uzawa algorithm and no decoupling error is introduced, because the two-step projection is formally equivalent to the original system (3.56).

However, the Uzawa algorithm is known to converge slowly at large computational expense. Therefore, it is usual to resort to a decoupling algorithm. In this perspective, the choice of $\mathbf{Q}$ directly defines the accuracy and stability properties of the algorithm. For instance, choosing

$$\mathbf{Q} = \frac{\Delta t}{\beta_0} \mathbf{M}^{-1}, \tag{3.62}$$

the so-called fractional-step method of first-order time-accuracy is obtained. This method can be very efficient if the mass operator is diagonal. This is the case for many numerical methods such as the finite differences, the finite volumes and the spectral elements if the numerical quadrature required for the evaluation of the weak formulation (3.2) is performed using the same Gauss–Lobatto–Legendre points as the one used for the definition of the basis functions (3.17).

Using this method, the decoupling error does not vanish when the problem reaches a steady-state solution. This may be detrimental, because converged solutions might depend on the time-step and change with it. To escape from this dismal performance and remove the decoupling error for steady problems, the fractional-step method can be modified introducing a pressure correction

$$\begin{pmatrix} \mathbf{H} & \mathbf{HQD}^{\mathrm{T}} \\ \mathbf{D} & \mathbf{0} \end{pmatrix} \begin{pmatrix} \mathbf{v}_{n+1} \\ \mathbf{p}_{n+1} - \mathbf{p}_n \end{pmatrix} = \begin{pmatrix} \mathbf{Mf}_{n+1} + \mathbf{D}^{\mathrm{T}}\mathbf{p}_n \\ \mathbf{0} \end{pmatrix} + \begin{pmatrix} \mathbf{Mr}_{n+1} \\ \mathbf{0} \end{pmatrix}. \tag{3.63}$$

The block decomposition of (3.63) with the operator $\mathbf{Q}$ given by (3.62) leads to a second order scheme whose decoupling error vanishes for a steady solution. More details on this topic can be found in [16, 17, 46].

Chapter 4

Subgrid modelling

The Navier–Stokes model introduced in chapter 2 describes the fluid dynamics at the macroscopic level whereas the filtered equations, which are used for large eddy simulation, introduce a coarser level of approximation. Large-scale structures are obtained by the computed flow dynamics while the behaviour of the subgrid scales and their interaction with the large eddies are modelled by the additional terms arising from the filtering operation. The expression of these terms as functions of the resolved quantities is referred to as subgrid modelling.

Usual approaches used for subgrid modelling, such as the subgrid viscosity models detailed in [52], usually rely on simplified theories of turbulence which are applicable for relatively simple flows and only available for the simplest case of the Newtonian fluids. The recent extension of numerical fluid dynamics to the study of biological systems, plasma physics or geophysics reveals a substantial need for improvement in terms of subgrid modelling for complex flows and complex fluids. For such cases, the physics of the subgrid scales is not clearly understood which prevents the use of functional models, that is to impose a known physical behaviour to the subgrid scales in order to model their action on the resolved ones.

This issue could be overcome by the deconvolution-based subgrid models which aim at a partial recovery of the original quantities from their filtered counterpart. In principle, functional modelling is avoided by attempting to invert the filtering operator applied to the governing equations. However, this apparent advantage is completely lost since these models are usually coupled with auxiliary approaches, based on functional models, in order to account for the interactions with the unrepresentable scales of the solution, *i.e.* not representable on the coarser spatial discretization used for the large eddy simulation.

By interpreting the spatial discretization of the equations as the only effective filter applied in the framework of a large eddy simulation, the grid filter models first introduced by Habisreutinger in [24] and further detailed hereafter allow to totally suppress the need for functional modelling. Indeed, when no explicit filter is applied but only the implicit grid filter is considered, deconvolution models can actively contribute to subgrid modelling but in a very different way than the one associated with large eddy simulations relying on explicit filtering. The grid filter models enable the interpretation of deconvolution models when used with implicit filtering as a way to approximate the effect of the grid filter on the resolved scales of the solution. This approach gives therefore a theoretical justification to the use of deconvolution models without explicit filtering of the solution and explains how these models can be effective in this context.

4.1   General statement of the deconvolution problem

As detailed by Domaradzki and Adams in [18], subgrid modelling in the framework of deconvolution-based models is classically decomposed into the soft and the hard deconvolution problems which correspond to the primary modelling performed by the deconvolution procedure and the auxiliary modelling performed using functional approaches.

4.1.1 Soft deconvolution problem

The deconvolution procedure is usually restricted to the reconstruction of the scales that are computable with the coarser spatial discretization used for the large eddy simulation, which is referred to as the soft deconvolution problem. In (2.52), the filtered equations were formally written in the strong form

$$\boldsymbol{M}\,\partial_t\overline{\boldsymbol{u}} + \boldsymbol{A}(\overline{\boldsymbol{u}}) = \overline{\boldsymbol{f}} + [\boldsymbol{A}, \mathcal{K}\star](\boldsymbol{u}). \tag{4.1}$$

In the case of the Navier–Stokes equations for Newtonian fluids, the subgrid commutator on the right-hand side is given by equation (2.54) while (2.55) represents this quantity for Oldroyd-B fluids. The exact subgrid contribution appears as a function of the non-filtered field, which is not computed when performing a large eddy simulation. This field being unknown, the idea is to approximate it using a deconvolution procedure such as

$$\boldsymbol{u} \simeq \mathcal{K}' \star \overline{\boldsymbol{u}} = \mathcal{K}' \star \circ\, \mathcal{K} \star \boldsymbol{u}, \tag{4.2}$$

where $\mathcal{K}'\star$ represents an exact or approximate inverse of the filter $\mathcal{K}\star$ such that

$$\mathcal{K}' \star \circ\, \mathcal{K} \star \simeq \mathcal{I}\star, \tag{4.3}$$

$\mathcal{I}\star$ being the identity filtering operator. The subgrid term is then approximated as

$$[\boldsymbol{A}, \mathcal{K}\star](\boldsymbol{u}) \simeq [\boldsymbol{A}, \mathcal{K}\star](\mathcal{K}' \star \overline{\boldsymbol{u}}). \tag{4.4}$$

Several types of deconvolution procedures have been considered in the past, such as discrete-kernel and polynomial regularisation by Shah and Ferziger [53], Geurts [21] and Kuerten *et al.* [31]. Stolz and Adams [55] also introduced approximate deconvolution models based on the van Cittert method.

4.1.2 Hard deconvolution problem

However, reconstructing the computable scales is not sufficient for subgrid modelling because the interactions with the non-computable ones are not taken into account. To solve this issue, the deconvolution is usually supplemented with a secondary procedure, which is referred to as the hard deconvolution and which is achieved by the use of functional models. This procedure is formally performed introducing an additional term to (4.4)

$$[\boldsymbol{A}, \mathcal{K}\star](\boldsymbol{u}) \simeq [\boldsymbol{A}, \mathcal{K}\star](\mathcal{K}' \star \overline{\boldsymbol{u}}) + \overline{\boldsymbol{a}}(\overline{\boldsymbol{u}}). \tag{4.5}$$

For instance, Stolz *et al.* [56] introduced a relaxation term in order to account for energy transfers with the scales which are not recovered by the deconvolution procedure. Deconvolution models were also coupled with the Smagorinsky model by Winckelmans *et al.* [61] and with the dynamic mixed-scale model by Habisreutinger *et al.* [25].

4.2 Grid filter models

The motivations for the introduction of the grid filter models as a particular class of subgrid models arise from the following issues involved in the use of deconvolution-based models.

First, the soft deconvolution problem only relies on the definition of the convolution filter without the need to resort to any functional modelling. The definition of the filter is therefore the

first central issue involved in the use of such models. The question is then, how to properly define this convolution filter?

Second, the apparent advantage of deconvolution models over classical approaches is to avoid the need for functional modelling. However, since functional models are required for the hard deconvolution problem, this advantage vanishes. The question is then, would it be possible to use the deconvolution approach for both the soft and the hard deconvolution problems?

As further detailed hereafter, the answer to both questions is given by the introduction of the grid filter models and is based on taking explicitly into account the major role played by the spatial discretization in large eddy simulation, which is not explicitly done in the previous formal developments.

4.2.1 Definition

The central idea relies on the interpretation of the effect of the spatial discretization as an implicit filter which is applied to the governing equations. In this case, the filter $\mathcal{K}\star$ to consider in practical simulations is a composition of an explicit filter $\mathcal{L}\star$ and the projective grid filter $\mathcal{G}\star$ associated to the spatial discretization, which reads

$$\mathcal{K}\star = \mathcal{L}\star \circ \mathcal{G}\star. \tag{4.6}$$

Hence, considering the grid filter in equation (4.1) leads to

$$\boldsymbol{M}\,\partial_t\overline{\boldsymbol{u}} + \boldsymbol{A}(\overline{\boldsymbol{u}}) = \overline{\boldsymbol{f}} + [\boldsymbol{A}, \mathcal{L}\star \circ \mathcal{G}\star](\boldsymbol{u}). \tag{4.7}$$

In the sequel, the focus is put on the particular case where no explicit filter $\mathcal{L}\star$ is applied, that is on large eddy simulations solely based on implicit filtering, which allows to obtain

$$\boldsymbol{M}\,\partial_t\hat{\boldsymbol{u}} + \boldsymbol{A}(\hat{\boldsymbol{u}}) = \hat{\boldsymbol{f}} + [\boldsymbol{A}, \mathcal{G}\star](\boldsymbol{u}), \tag{4.8}$$

where $\hat{\boldsymbol{u}} = \mathcal{G}\star\boldsymbol{u}$ is the grid-filtered unknown, or in other words the part of the unknown field that can be resolved by the spatial discretization used to perform the large eddy simulation. In this framework, subgrid modelling based on deconvolution models would require the subgrid commutator of the previous equation to be expressed solely in terms of the known grid-filtered fields, which formally reads

$$[\boldsymbol{A}, \mathcal{G}\star](\boldsymbol{u}) \simeq [\boldsymbol{A}, \mathcal{G}\star](\mathcal{G}' \star \hat{\boldsymbol{u}}), \tag{4.9}$$

where the reconstruction operator $\mathcal{G}'\star$ is the approximate inverse of the grid filtering operation to be devised. The problem with equation (4.9) is that the reconstructed field $\mathcal{G}' \star \hat{\boldsymbol{u}}$ is not representable with the spatial discretization used for the large eddy simulation. Therefore, a direct reconstruction model based on the approximate inversion of the grid filter would require the use of the full spatial discretization to evaluate the subgrid commutator. This issue explains why the deconvolution procedure is usually restricted to the computable scales.

In order to solve this issue, the idea introduced by Habisreutinger [24] and Bouffanais [10] is to replace the grid filter by an invertible modelling filter $\tilde{\mathcal{G}}\star$ which reproduces its effect on the computed modes of the solution. This is formally expressed by

$$[\boldsymbol{A}, \mathcal{G}\star](\boldsymbol{u}) \simeq [\boldsymbol{A}, \tilde{\mathcal{G}}\star](\tilde{\mathcal{G}}^{-1} \star \hat{\boldsymbol{u}}) = [\boldsymbol{A}, \tilde{\mathcal{G}}\star](\tilde{\boldsymbol{u}}). \tag{4.10}$$

Compared to (4.4), this relation gives a formal definition in order to design the convolution filter which has to approximate the effect of the grid filter on the computable modes. Moreover, and

compared to (4.9), the deconvoluted field $\tilde{\boldsymbol{u}}$ shall be representable on the spatial discretization used for the large eddy simulation. Since the modelling filter has to be invertible, it can be interpreted as a change of variable whose physical meaning is detailed in sections 4.2.4 and 4.2.5. The approximation (4.10) being the only required modelling, the subgrid models arising from this new approach are referred to as grid filter models.

This new interpretation builds a theoretical basis which enables the use of deconvolution-based subgrid models without any explicit filtering. The grid filter models use therefore the deconvolution approach originally meant to solve the soft deconvolution problem, that is the inversion of the explicit filter, to solve the hard deconvolution one which corresponds to model the effect of the scales lost by spatial discretization on the resolved ones. Consequently, the classical distinction between the soft and hard deconvolution problems becomes useless.

The governing equations to be solved in the framework of the grid filter models are obtained by combining the equation (4.8) with the approximation (4.10), and read

$$\boldsymbol{M}\,\partial_t \hat{\boldsymbol{u}} + \boldsymbol{A}(\hat{\boldsymbol{u}}) = \hat{\boldsymbol{f}} + [\boldsymbol{A}, \tilde{\mathcal{G}}\star](\tilde{\boldsymbol{u}}), \tag{4.11}$$

thereby achieving the general definition of this particular class of deconvolution models for large eddy simulation.

4.2.2   Grid filter

Before any attempt to model the grid filter, it should be first formally defined. Considering the expansion (3.6) of the unknown into a linear combination of basis functions, which is a common framework among a broad range of spatial discretization methods, the splitting between resolved and subgrid fields is expressed in physical space by

$$u(x,t) = \hat{u} + \hat{u}' = \sum_{j=1}^{\mathrm{p}} \underline{u}_j(t)\phi_j(x) + \sum_{j=\mathrm{p}+1}^{\mathrm{q}} \underline{u}_j(t)\phi_j(x). \tag{4.12}$$

In other words, the coarser level of approximation and the reduction of the computational costs are respectively introduced and achieved by only computing the evolution of the first p modes of the unknown instead of the q ones required to express all the space-scales of the solution.

Modal formulation

In modal space, the application of the grid filter $\mathcal{G}\star$ is represented by the following linear and projective transformation

$$\hat{\underline{u}} = \underline{\mathbf{G}}\,\underline{u}, \tag{4.13}$$

where the vector $\hat{\underline{u}}$ contains the p computable modes while $\underline{u}$ contains all the modes of the solution, that is the $\mathrm{q} \geq \mathrm{p}$ ones. The rectangular projection matrix $\underline{\mathbf{G}}$ associated to the grid filter is of size (p, q) and is given by

$$\underline{\mathbf{G}}_{ij} = \delta_{ij}, \tag{4.14}$$

representing therefore a top-hat filter in modal space which cuts off the high-frequency modes of the solution, as illustrated in figure 4.1. Perhaps more explicitly, the grid filter matrix is composed by an identity matrix of size p on the left-hand side and by null entries on the right-hand side, which can be illustrated by the block representation

$$\underline{\mathbf{G}} = (\mathbf{I} \mid \mathbf{0}). \tag{4.15}$$

Consequently, the p modes of the grid-filtered signal are equal to the first p ones of the original field. However, as noticed in figure 4.1, the nodal values are different in physical space.
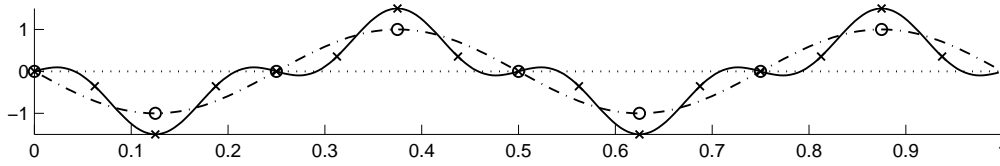
Fig. 4.1: In the Fourier basis (3.27) of size q = 16, the original field (solid line) is defined as $u = -\sin(4\pi x) + .5\sin(12\pi x)$. The corresponding filtered signal (dash-dotted line), projected onto a basis of size p = 8, becomes $\hat{u} = -\sin(4\pi x)$ which represents the loss of the high-frequency contribution associated with the grid-filtering operation.

Nodal formulation

In other words, the grid filter conserves the modes but alters the nodal values of the signal. This statement can be better understood considering the grid filter matrix in physical space. Hence, using a generalisation of the transformation rule (3.44), the nodal representation of the grid filter is given by

$$\mathbf{G} = \mathbf{\Phi}_{\mathrm{p}}^{\mathrm{p}} \, \underline{\mathbf{G}} \, \underline{\mathbf{\Phi}}_{\mathrm{q}}^{\mathrm{q}}, \tag{4.16}$$

and represented in figure 4.2 for the Fourier basis and in the case of the finite and spectral elements. In all cases, the simple modal formulation (4.15) becomes a basis-dependent and full matrix whose interpretation is not straightforward. Moreover, it is worth noticing that the boundary values are not affected by the grid filtering in the case of the finite and spectral elements. This comment does not apply in the case of the Fourier basis since only periodic functions are representable.
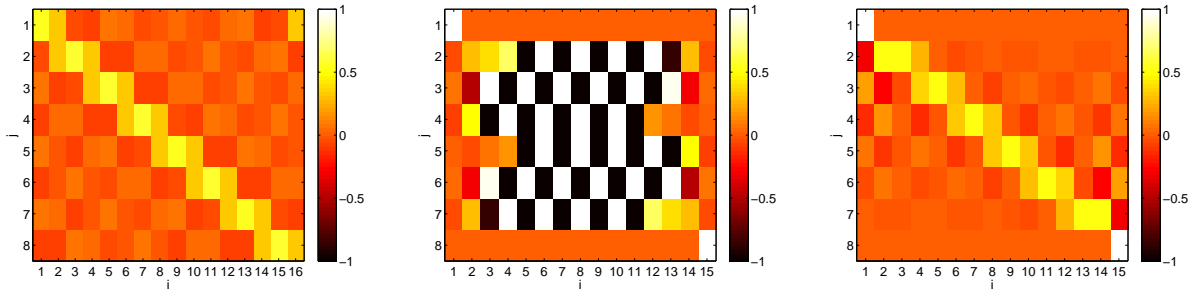
Fig. 4.2: Nodal grid filter for p = 8 and q = 16 in the case of the Fourier basis (left). For the finite elements (centre) and the spectral elements (right) q = 15.

At this stage, it is of crucial importance to note that the effect of the grid filter only depends on the couple (p, q) and on the numerical method, *i.e.* the approximation basis, that is on the under-resolution generated by the coarser spatial discretization.

4.2.3   Sampling filter

As detailed in section 4.2.4, modelling the effect of the grid filter on the resolved scales requires the definition of the sampling filter. And as mentioned in section 3.1.2, the original field approximated with a q-dimensional set of basis functions is bijectively associated with q interpolation points. By definition, the sampling filter $\mathcal{S}\star$ performs the interpolation of the original field on a subset of p points, which is illustrated in figure 4.3.
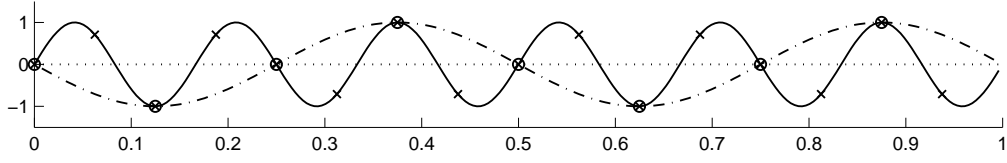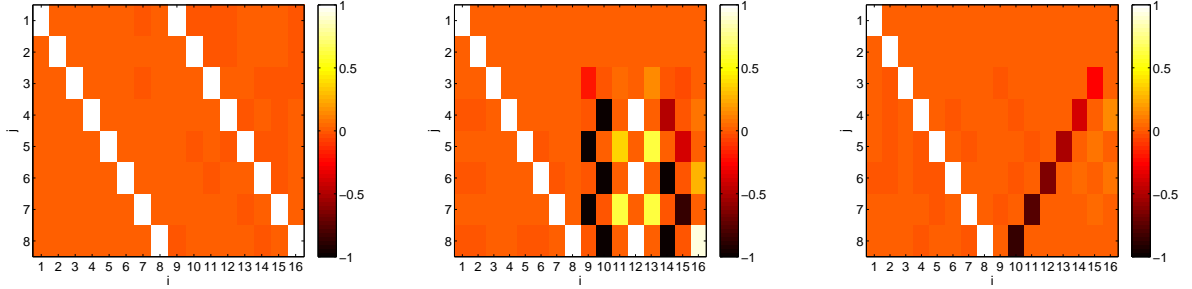
Fig. 4.3: Using the Fourier basis (3.27), the original field $u = \sin(12\pi x)$ based on q = 16 points (solid line) is sampled with p = 8 points. The resulting under-sampled signal (dash-dotted line) becomes $\tilde{u} = -\sin(4\pi x)$ which represents the aliasing phenomenon associated with the sampling operation.

Modal formulation

In modal space, the application of the sampling filter is expressed by the following linear and projective transformation

$$\underline{\tilde{u}} = \underline{S}\,\underline{u}, \tag{4.17}$$

where the vector $\underline{\tilde{u}}$ contains the p modes associated to the under-sampled field. Consequently, the rectangular sampling matrix $\underline{S}$ associated to the sampling filter is of size (p, q). Using equations (3.9) and (3.11), the sampling matrix is easily determined according to the definition of the sampling operation

$$\underline{\tilde{u}} = \underline{\Phi}_p^p \Phi_q^p \underline{u}. \tag{4.18}$$

In other words, the original field is first evaluated from the q-dimensional modal basis onto p points in physical space, then brought back into the corresponding modal space of size p. Hence, comparing equations (4.17) and (4.18) implies

$$\underline{S} = \underline{\Phi}_p^p \Phi_p^q. \tag{4.19}$$

In order to illustrate the dependence on the discretization method, the sampling matrix is illustrated in figure 4.4 for the Fourier basis and in the cases of the finite and the spectral elements. For all cases, the matrices are composed by the identity on the left-hand part. This simply means

Fig. 4.4: Modal sampling filter for p = 8 and q = 16 in the case of the Fourier basis (left), the finite elements (centre) and the spectral elements (right).

that the first p modes of the original signal are preserved during the sampling process since they are bijectively associated with p interpolation points. Using again the block representation introduced for the grid filter, the sampling matrix can be schematically represented by

$$\underline{S} = (\mathbf{I} \mid \underline{F}), \tag{4.20}$$

where the right-hand part of the matrix, which is strongly basis-dependent, expresses the aliasing phenomenon, that is the folding of the high-order modes onto the low-order ones, which was illustrated in figure 4.3.
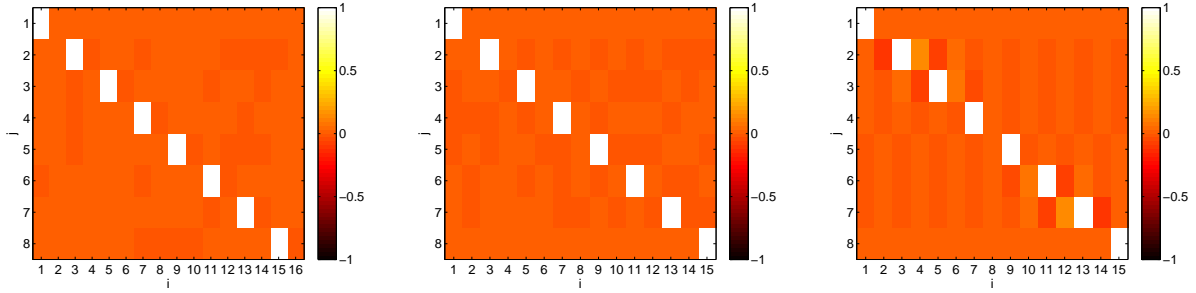
Fig. 4.5: Nodal sampling filter for p = 8 and q = 16 in the case of the Fourier basis (left). For the finite elements (centre) and the spectral elements (right) q = 15.

For the Fourier basis, the aliasing part of the matrix is the identity which shows that any mode $i \leq \mathrm{p}$ is only aliased by the modes $i+n\mathrm{p}$ with $n \in \mathbb{N}^+$. In the case of the Lagrange bases, the coupling between the modes is very different and much stronger in the case of the finite elements. The formal demonstration of these comments seems quite involved since the definition of the sampling operation relies on the inversion of a full matrix, see equation (4.19). The reader, and the author, are thus already left with an open question which is however very interesting to investigate.

Nodal formulation

Because of the folding phenomenon, the p modes of the sampled signal are not equal to the first p ones of the original field. However, as noticed in figure 4.3, the nodal values are conserved during the sampling operation. The behaviour is therefore opposite compared to the grid filter, since the nodal values are conserved and the modes are altered.

This statement is further explained considering the nodal expression of the sampling filter which is formulated by

$$\mathbf{S} = \mathbf{\Phi}_\mathrm{p}^\mathrm{p} \, \underline{\mathbf{S}} \, \underline{\mathbf{\Phi}}_\mathrm{q}^\mathrm{q} = \mathbf{\Phi}_\mathrm{p}^\mathrm{q} \underline{\mathbf{\Phi}}_\mathrm{q}^\mathrm{q}, \tag{4.21}$$

and represented in figure 4.5. In the case of the Fourier basis and for the finite elements, the p points associated with the sampled signal also belong to the original set of q points. Consequently, the nodal sampling matrix has only Boolean entries. In other words, the information is exactly conserved for the remaining points while it is erased for the discarded ones. For the spectral elements, the p interpolation points are not present in the original set which leads to a nodal sampling matrix whose interpretation is not as straightforward.

4.2.4   Modelling filter

At this point, the effect of the grid filter is exactly determined through the definition of the grid filter matrix introduced in equation (4.13). However, when performing a large eddy simulation, the filtering operation has to be restricted to the computable modes because the original field composed of q modes can not be represented by the spatial discretization.

For this purpose, let the matrix $\mathbf{S}'$ of size (q, p) denote an approximate inverse of the sampling operation such that

$$\mathbf{u} \simeq \mathbf{S}' \tilde{\mathbf{u}}, \tag{4.22}$$

where $\tilde{\mathbf{u}}$ is the under-sampled field of equation (4.17). Using the approximate inverse of the sampling

filter, the grid-filtering operation can be approximated as

$$\hat{\mathbf{u}} = \mathbf{G}\mathbf{u} \simeq \mathbf{G}\mathbf{S}'\tilde{\mathbf{u}} = \tilde{\mathbf{G}}\tilde{\mathbf{u}}, \tag{4.23}$$

where the square matrix $\tilde{\mathbf{G}}$ of size (p, p) represents the modelling filter $\tilde{\mathcal{G}}\star$ introduced in equation (4.10). Hence, the approximate inversion of the sampling filter bears the entire subgrid modelling in the particular framework of the grid filter models.

Equation (4.23) reveals the approximate character of the grid filter models and defines the modelling filter. This filter actually models the effect of the grid filter on the resolved modes using the sampled field which is representable on the spatial discretization used for the large eddy simulation. The application of the modelling filter can therefore be interpreted as the approximate and bijective change of variable between the sampled and grid-filtered quantities, both being representable on the coarse spatial discretization which only retains the first p modes.

4.2.5 Physical interpretation

In order to better understand the idea of the grid filter models, it is of crucial importance to understand the physical meaning of the change of variable associated with the modelling filter. For this purpose, recall from sections 4.2.2 and 4.2.3 that the grid filter conserves the modal values and the sampling filter conserves the nodal ones.

Considering the Navier–Stokes operator in the Newtonian case, the governing equations of the grid filter models (4.11), written in the semi-discrete form and using the Fourier basis, read

$$\dot{\underline{\hat{\mathbf{v}}}}_{\mathbf{k}} + i\mathbf{k} \cdot \widehat{\underline{\tilde{\mathbf{v}}}\underline{\tilde{\mathbf{v}}}}_{\mathbf{k}} = -\mathrm{Re}^{-1}\mathbf{k}^2 \underline{\hat{\mathbf{v}}}_{\mathbf{k}} + \underline{\hat{\mathbf{g}}}_{\mathbf{k}} - i\mathbf{k}\underline{\hat{\mathbf{p}}}_{\mathbf{k}}, \tag{4.24}$$

$$i\mathbf{k} \cdot \underline{\hat{\mathbf{v}}}_{\mathbf{k}} = \mathbf{0}, \tag{4.25}$$

which are similar to (3.33)-(3.34). In this framework, the goal of the large eddy simulation is to correctly compute the time-evolution of the first p modes of the solution which would be decoupled in linear cases. But the non-linear contribution couples the modes and would require the use of the original quantities to be evaluated. As noticed in equation (4.24), the original quantities are replaced by the sampled ones to evaluate the non-linear terms. In other words, in order to correctly compute the evolution of the first p modes, the non-linear terms have to be computed based on the right nodal values.

Hence, the goal of the modelling filter, is to retrieve the right nodal values from the right modes. However, as suggested in equation (4.23), this change of variable is only approximate. Therefore, the accuracy of this approximation directly governs the quality of subgrid modelling for the grid filter models.

In consequence, the grid filter models can be interpreted as a deconvolution approach since the sampled original quantities are sought from their grid-filtered counterpart.

4.3 Approximate inverses of projective operators

As mentioned in section 4.2.4, following up on the idea of the grid filter models requires to face the difficult problem of approximating the inverse of the sampling filter, which is a projective operator. This results from the loss of information due to the coarser spatial discretization used for the large eddy simulation.

In order to deal with this major issue, the so-called consistency constraint and the accuracy of the approximate inverse have to be introduced. Furthermore, a general method of approximation is proposed.

4.3.1   Consistency

For the definition of the consistency constraint in a general framework, let the rectangular matrix $\mathbf{P}$ of size (p, q), similar to the grid and sampling filters, characterise the general projective operation

$$\bar{\mathbf{u}} = \mathbf{P}\mathbf{u}. \tag{4.26}$$

As illustrated in figure 4.6 with a trivial two-dimensional example, and because of its projective nature, this operation has an infinite number of possible inverses which lie on the dash-dotted line parallel to the direction of projection, referred to as the admissible subspace.
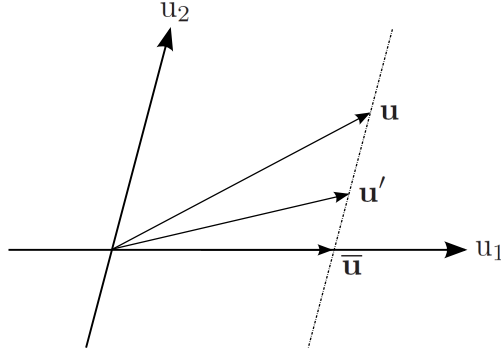
Fig. 4.6: Two-dimensional example of a projective operation using $\mathbf{P} = (\ 1\ \ 0\ )$, its associated approximate inverse and the subspace of possible inverses represented by the dash-dotted line.

Introducing the matrix $\mathbf{P}'$ of size (q, p) as an approximate inverse of $\mathbf{P}$, an approximation $\mathbf{u}'$ of the original quantity is expressed by the relation

$$\mathbf{u} \simeq \mathbf{u}' = \mathbf{P}'\bar{\mathbf{u}}, \tag{4.27}$$

and has to belong to the admissible subspace represented by the dash-dotted line in figure 4.6. In order to guarantee this constraint, the projected quantity must be retrieved by re-projecting the approximation, which can also be expressed in the form

$$\bar{\mathbf{u}} = \mathbf{P}\mathbf{u}' = \mathbf{P}\mathbf{P}'\bar{\mathbf{u}}. \tag{4.28}$$

The approximate inverse operator has therefore to abide to the consistency constraint which arises from the previous equation

$$\mathbf{P}\mathbf{P}' = \mathbf{I}. \tag{4.29}$$

In other words, and for any variable, re-projecting the approximation must remain the identity operation. This constraint allows to *a priori* satisfy the three first properties of the Moore–Penrose pseudo-inverse

$$\mathbf{P}\mathbf{P}'\mathbf{P} = \mathbf{P}, \tag{4.30}$$
$$\mathbf{P}'\mathbf{P}\mathbf{P}' = \mathbf{P}', \tag{4.31}$$
$$(\mathbf{P}\mathbf{P}')^* = \mathbf{P}\mathbf{P}', \tag{4.32}$$
$$(\mathbf{P}'\mathbf{P})^* \neq \mathbf{P}'\mathbf{P}, \tag{4.33}$$

where the star denotes the conjugate transpose operation, but the fourth is not guarantied. While the four properties uniquely define the approximate inverse as the particular Moore–Penrose pseudo-inverse, not satisfying the last constraint leaves a degree of freedom for subgrid modelling. Indeed,

this purely mathematically defined inverse is not necessarily the best to use for the approximation of physical phenomena. It is worth stressing that this point is of crucial importance to understand the concepts presented in the sequel. In other words, subgrid modelling will not be performed using Moore–Penrose pseudo-inverses.

4.3.2 Accuracy

In the perspective of an approximate inversion, the other crucial issue is expressed in terms of accuracy, which can be quantified introducing the inversion error

$$\mathbf{e} = \mathbf{u} - \mathbf{u}' = (\mathbf{I} - \mathbf{P}'\mathbf{P})\mathbf{u}. \tag{4.34}$$

Consequently, defining the square matrix $\mathbf{Q} = \mathbf{P}'\mathbf{P}$, of size q and that characterises the approximation, the aim is to obtain

$$\mathbf{E} = \mathbf{I} - \mathbf{Q} \simeq \mathbf{0}, \tag{4.35}$$

where the matrix $\mathbf{E}$ represents the error associated with the approximate inversion.

However, this property can not be exactly satisfied which is explained by acknowledging the irrecoverable loss of information induced by the projective operation associated with the application of the matrix $\mathbf{P}$. Indeed, the approximation matrix can not be invertible, and consequently not be equal to the identity. The reader may be convinced of this statement by considering the relation

$$\mathbf{Q}^2 = \mathbf{P}'\mathbf{P}\mathbf{P}'\mathbf{P} = \mathbf{P}'\mathbf{P} = \mathbf{Q}, \tag{4.36}$$

which is obtained using the consistency constraint (4.29). In consequence, $\mathbf{Q}$ is a projector since it verifies the general property presented in equation (2.43), that is

$$\mathbf{Q}^n = \mathbf{Q}, \qquad \forall n \in \mathbb{N}^+. \tag{4.37}$$

4.3.3 Approximation methods

As previously mentioned, a projective operator has an infinite number of possible inverses and can not be exactly inverted. However, in order to approximate its inverse, the strategy which is introduced herein is to build a basis of the admissible subspace and to express the approximation of the original quantity as a linear combination of the basis elements. In order to understand this
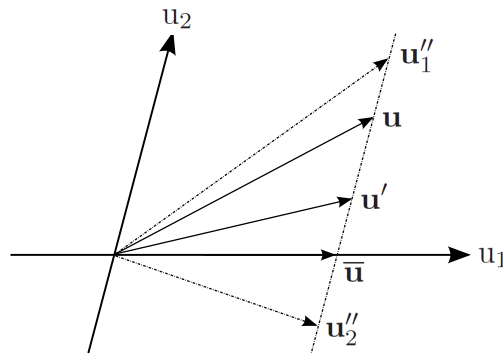

Fig. 4.7: Two-dimensional example of a projective operation using $\mathbf{P} = (\ 1\ \ 0\ )$. Approximation of the original quantity as a linear combination in the basis of the admissible subspace.

idea, the intuitive two-dimensional example introduced in figure 4.6 is reproduced in figure 4.7. In

this case, any approximation of the original quantity can be expressed as a linear combination of two other elements, $\mathbf{u}_1''$ and $\mathbf{u}_2''$, which build a basis of the subspace.

Following up on this idea, and according to equation (4.27), any admissible approximation of the original quantity is given by the expression

$$\mathbf{u}_j'' = \mathbf{P}_j'' \overline{\mathbf{u}}, \tag{4.38}$$

where the index j denotes one of the possible approximations and where any basis matrix $\mathbf{P}_j''$ must satisfy the consistency constraint (4.29), that is $\mathbf{PP}_j'' = \mathbf{I}$. Hence, a particular approximation of the original quantity is expressed as a linear combination of the form

$$\mathbf{u}' = \sum_{j=1}^{n} \omega_j \mathbf{u}_j'' = \sum_{j=1}^{n} \omega_j \mathbf{P}_j'' \, \overline{\mathbf{u}}. \tag{4.39}$$

By comparing equations (4.27) and (4.39), the approximate inverse of the projective operator is identified as

$$\mathbf{P}' = \sum_{j=1}^{n} \omega_j \mathbf{P}_j''. \tag{4.40}$$

The direct improvement in terms of accuracy related to this method may not be obvious. However, building a complete basis of the admissible subspace allows to express every possible inverse of the projector. Finally, applying the consistency constraint to equation (4.40) implies to satisfy

$$\sum_{j=1}^{n} \omega_j = 1. \tag{4.41}$$

This method therefore translates the inversion problem onto the definition of an approximation basis and an appropriate set of coefficients for the linear combination. Considering the large variety of possible projectors, already illustrated by the grid and sampling filters, it seems that this problem shall be handled case by case, using purely algorithmic approaches or assumptions related to the physics of the particular problem which is studied.

In any case, the basis and the coefficients have to be defined solely using the projected signal, which is the only available information. In order to clarify this idea, the dependence of the approximate inverse on the projected quantities shall be explicitly written. Hence, in the most general case, equation (4.40) reads

$$\mathbf{P}'(\overline{\mathbf{u}}) = \sum_{j=1}^{n} \omega_j(\overline{\mathbf{u}}) \mathbf{P}_j''(\overline{\mathbf{u}}), \tag{4.42}$$

where both the basis and the coefficients depend on the projected quantities, and which is referred to as the dynamic-basis approximation. On the other hand, the dependence can be restricted to the coefficients, which yields

$$\mathbf{P}'(\overline{\mathbf{u}}) = \sum_{j=1}^{n} \omega_j(\overline{\mathbf{u}}) \mathbf{P}_j'', \tag{4.43}$$

and which is referred to as the static-basis approximation. This case is similar to the so-called numerical approximation introduced for the spatial discretization in equation (3.6) and the underlying idea is really similar. However, the space which has to be approximated here is of finite dimension.

4.4   Approximate inverse of the sampling filter

As mentioned in section 4.2.4, subgrid modelling in the framework of the grid filter models exclusively relies on the approximate inversion of the sampling filter which folds the lost modes onto the computable ones.

Up to now, the grid filter models have been presented as a straightforward and one-way approach of subgrid modelling. But, from now on, the presentation relies on modelling assumptions which could be enhanced or modified. Consequently, this point is marked as a possible start for further research and a bifurcation of many modelling ways. In other words, the stage is just set, and it is only the opening of the show...

4.4.1   Approximation basis

Because of the aliasing phenomenon associated to the sampling operation, the p modes of the sampled signal are polluted and completely loose their physical meaning, the spectral information being destroyed. Therefore, the approximation basis proposed herein relies on a purely algorithmic and intuitive approach to unfold the modes.

A rough estimate of the unfolding operation is given by the transpose of the modal sampling matrix. Indeed, applying this matrix to the sampled signal only reconstructs the modes which could have been present in the original signal, however with the wrong magnitude and not necessarily satisfying the consistency constraint. In order to overcome these issues, a given basis matrix is expressed by pre- and post-multiplying the transpose of the sampling matrix

$$\underline{\mathbf{S}}_j'' = \mathbf{W}_j \underline{\mathbf{S}}^{\mathrm{T}} \mathbf{C}_j, \tag{4.44}$$

where $\mathbf{W}_j$ is a square matrix of size q which weights the modes after the unfolding, while $\mathbf{C}_j$ is a square matrix of size p which allows to ensure the consistency of the approximation. Hence, using the consistency property (4.29) yields

$$\underline{\mathbf{S}}\ \underline{\mathbf{S}}_j'' = \underline{\mathbf{S}}\mathbf{W}_j \underline{\mathbf{S}}^{\mathrm{T}} \mathbf{C}_j = \mathbf{I}, \tag{4.45}$$

and allows to find the relation between the weight and consistency matrices formulated by

$$\mathbf{C}_j = (\underline{\mathbf{S}}\mathbf{W}_j \underline{\mathbf{S}}^{\mathrm{T}})^{-1}, \tag{4.46}$$

which finally leads to the expression

$$\underline{\mathbf{S}}_j'' = \mathbf{W}_j \underline{\mathbf{S}}^{\mathrm{T}} (\underline{\mathbf{S}}\mathbf{W}_j \underline{\mathbf{S}}^{\mathrm{T}})^{-1}. \tag{4.47}$$

A given basis matrix is therefore exclusively defined by the corresponding weight matrix. If they were available, an intuitive strategy would be to weight the unfolding operation by the original quantities, that is using the diagonal matrix

$$\mathbf{W}_j = \underline{\mathbf{U}}, \qquad \underline{\mathbf{U}}_{ik} = \delta_{ik}\underline{\mathbf{u}}_k. \tag{4.48}$$

With this choice, *a posteriori* numerical experiments show that the first p modes are perfectly recovered for any of the bases considered, *i.e.* for the Fourier basis and for the finite and spectral elements. In other words, choosing the weight matrix according to (4.48) implies

$$\underline{\mathbf{u}}_i = (\underline{\mathbf{S}}_j'')_{ik}\underline{\tilde{\mathbf{u}}}_k, \qquad 1 \leq i \leq \mathrm{p}. \tag{4.49}$$

Moreover, and quite surprisingly, the subgrid modes are also perfectly recovered for the Fourier basis. But this is not the case for the other discretization methods and the error strongly depends on the original signal.

Despite many attempts, the formal demonstration of these observations could not be achieved, which leads to a second unanswered question. However, in order to give some clues of the proof, it might be interesting to note that the relation

$$\mathbf{E}\,\underline{\mathbf{U}}\,\underline{\mathbf{S}}^{\mathrm{T}} = \mathbf{0} \tag{4.50}$$

is verified by this particular inverse, but this property is not equivalent to (4.35) since $\underline{\mathbf{S}}^{\mathrm{T}}$ is not invertible. In order to shed some light onto the possible mathematical meaning of this relation, consider the definition of the matrix of the sampled elementary signals

$$\tilde{\underline{\mathbf{U}}} = \underline{\mathbf{S}}\,\underline{\mathbf{U}}, \tag{4.51}$$

and the approximate inverse operation

$$\underline{\mathbf{S}}''_j\tilde{\underline{\mathbf{U}}} \simeq \underline{\mathbf{U}}. \tag{4.52}$$

The explicit formulation of an approximate inverse of the sampling filter can be obtained multiplying this relation by a regularisation matrix $\mathbf{H}''_j$ of size (q, p) in such a way that the product $\tilde{\underline{\mathbf{U}}}\mathbf{H}''_j$ be invertible

$$\underline{\mathbf{S}}''_j\tilde{\underline{\mathbf{U}}}\mathbf{H}''_j = \underline{\mathbf{U}}\mathbf{H}''_j. \tag{4.53}$$

Among the possibilities for such a regularisation, relying on the straightforward choice $\mathbf{H}''_j = \underline{\mathbf{S}}^{\mathrm{T}}$ yields

$$\underline{\mathbf{S}}''_j = \underline{\mathbf{U}}\,\underline{\mathbf{S}}^{\mathrm{T}}(\underline{\mathbf{S}}\,\underline{\mathbf{U}}\,\underline{\mathbf{S}}^{\mathrm{T}})^{-1}, \tag{4.54}$$

which corresponds to the formulation (4.47) with the weight matrix given by (4.48). Hence, the intuitive approach meant to unfold and weight the modes simply represents the regularisation of equation (4.52) with the transpose of the sampling matrix.

In this framework, the definition of a particular approximate inverse corresponds to the choice of a particular regularisation of equation (4.52). Similarly, equation (4.50) represents the regularisation of (4.35) by the product $\underline{\mathbf{U}}\,\underline{\mathbf{S}}^{\mathrm{T}}$.

4.4.2 Closure of the approximation

Considering the satisfying accuracy of the approximation obtained with the single basis matrix defined by (4.47) and using (4.48), the approximate inverse of the sampling filter which will be used in the test cases presented hereafter is chosen as

$$\underline{\mathbf{S}}' = \underline{\mathbf{U}}\,\underline{\mathbf{S}}^{\mathrm{T}}(\underline{\mathbf{S}}\,\underline{\mathbf{U}}\,\underline{\mathbf{S}}^{\mathrm{T}})^{-1}, \tag{4.55}$$

which corresponds to the dynamic-basis approximation (4.42) with n = 1. In this case, the single coefficient of the linear combination is trivially given by (4.41).

However, this approximation requires the use of the original signal which is not known when performing a large eddy simulation. Therefore, using this particular approximate inverse of the sampling filter implies the additional approximation of the original variable from its grid-filtered counterpart, that is

$$\underline{\mathbf{U}}_{ij} = \underline{\mathbf{u}}_i\delta_{ij} \simeq \underline{\mathbf{G}}'_{ik}\hat{\underline{\mathbf{u}}}_k\delta_{ij}, \tag{4.56}$$

where the reconstruction matrix $\underline{\mathbf{G}}'$ represents in modal space the reconstruction operator, that is the inverse of the grid filter appearing in equation (4.9). This relation shows that the approximate inverse of the sampling filter is a non-linear operator which depends on the grid-filtered field, and on the approximate inverse of the grid filter.

4.5 Approximate inverse of the grid filter

Considering the approximate inverse of the sampling filter proposed in section 4.4, the modelling issues are reported into the approximate inversion of the grid filter, which seems rather logical in this framework since the only available information on the system are the grid-filtered quantities.

The grid filter is a cutting-projector which induces the sharp loss of the high-frequency information. In this case, the approximate inverse can not be expressed in terms of the transpose grid filter matrix, as done for the sampling filter, since it does not bear any information on the coupling between the modes.

However, the remaining modes are not polluted by any aliasing contribution. This clean information on the low-order modes can therefore be used to approximate the inverse using physical considerations on the coupling between the modes. In consequence, here is the point where physics comes back into the play. . .

4.5.1 Approximation basis

Like for the sampling filter, the first aim is to provide a general method in order to generate a basis of possible inverses. For this purpose, assume that any elementary increment of the original field can be approximated from the increment of its grid-filtered counterpart, which reads

$$\mathbf{d\underline{u}} \simeq \underline{\mathbf{G}}''_j \mathbf{d\underline{\hat{u}}}. \tag{4.57}$$

In other words, an approximation of the q existing increments $\mathbf{d\underline{u}}$ is sought only knowing the first p computed ones $\mathbf{d\underline{\hat{u}}}$. In order to comply with the consistency constraint (4.29), the approximate inverse of the grid filter has to take the general form

$$\underline{\mathbf{G}}''_j = \begin{pmatrix} \mathbf{I} \\ \underline{\mathbf{R}}''_j \end{pmatrix}, \tag{4.58}$$

where the block matrix $\underline{\mathbf{R}}''_j$ is responsible for the approximate reconstruction of the subgrid modes based on the computed ones. Let

$$\mathbb{Q} = \{1, \ldots, i, \ldots, q\} \tag{4.59}$$

be the space of the indexes corresponding to the existing modes of the solution. Assuming that each increment $\mathrm{d}\underline{u}_i$ can be retrieved from all the others implies the existence of the matrix of coupling functions κ_{ij} such that

$$\mathrm{d}\underline{u}_i \simeq \kappa_{ij}(\{\underline{u}_k, \mathrm{d}\underline{u}_k\}). \qquad \forall i, k \in \mathbb{Q}, \tag{4.60}$$

In this case, any approximated increment of the mode $\underline{u}_i$ becomes

$$\mathrm{d}\underline{u}_i \simeq \sum_{k \in \mathbb{Q}_i} \frac{\partial \underline{u}_i}{\partial \underline{u}_k} \, \mathrm{d}\underline{u}_k = \sum_{k \in \mathbb{Q}_i} \mathrm{J}_{ik} \, \mathrm{d}\underline{u}_k, \tag{4.61}$$

with $\mathbb{Q}_i = \mathbb{Q} \setminus \{i\}$ and J_{ik} the Jacobian component which expresses the link between the increments of the modes i and k. Then, considering the first p increments $\mathrm{d}\underline{u}_k$ to be known, that is

$$\mathrm{d}\underline{\hat{u}}_i = \sum_{k=1}^{q} \underline{\mathbf{G}}_{ik} \, \mathrm{d}\underline{u}_k = \sum_{k=1}^{q} \delta_{ik} \, \mathrm{d}\underline{u}_k = \mathrm{d}\underline{u}_i, \qquad 1 \le i \le \mathrm{p}, \tag{4.62}$$

equation (4.61) is reduced and split as follows

$$\mathrm{d}\underline{u}_i \simeq \sum_{k=1}^{p} \mathrm{J}_{ik}\,\mathrm{d}\underline{\hat{u}}_k + \sum_{l=p+1, l\neq i}^{q} \mathrm{J}_{il}\,\mathrm{d}\underline{u}_l, \qquad p < i \leq q, \tag{4.63}$$

where the increment $\mathrm{d}\underline{u}_l$ in the second term of the right-hand side is rewritten in terms of the basis matrix using equation (4.57)

$$\mathrm{d}\underline{u}_i \simeq \frac{1}{2}(\sum_{k=1}^{p} \mathrm{J}_{ik}\,\mathrm{d}\underline{\hat{u}}_k + \sum_{l=p+1}^{q} \mathrm{J}_{il} \sum_{k=1}^{p} \underline{\mathrm{G}}''_{lk}\,\mathrm{d}\underline{\hat{u}}_k), \qquad p < i \leq q, \tag{4.64}$$

since $\mathrm{J}_{ii} = 1$ and where the subscript j is temporarily omitted to simplify notations. Reorganising the last equation gives

$$\mathrm{d}\underline{u}_i \simeq \sum_{k=1}^{p} \frac{1}{2}(\mathrm{J}_{ik} + \sum_{l=p+1}^{q} \mathrm{J}_{il}\underline{\mathrm{G}}''_{lk})\,\mathrm{d}\underline{\hat{u}}_k, \qquad p < i \leq q, \tag{4.65}$$

from which the entries of the basis matrix are identified with respect to equations (4.57) and (4.62) as

$$\underline{\mathrm{G}}''_{ik} = \begin{cases} \delta_{ik}, & 1 \leq i \leq p, \\ \dfrac{1}{2}\left(\mathrm{J}_{ik} + \displaystyle\sum_{l=p+1}^{q} \mathrm{J}_{il}\underline{\mathrm{G}}''_{lk}\right), & p < i \leq q, \end{cases} \tag{4.66}$$

which is of the required form defined in equation (4.58). For a given Jacobian matrix, equation (4.66) expresses how the entries of the basis matrix must be constructed to approximate the unknown increments from the p computed ones.

Since the expression of the components takes into account the existence of both the lower and the higher order modes, as suggested by the sum over q in equation (4.66), it should be noted that the resulting process is implicit. Introducing the matrices $\mathbf{X}$ of size (q, q) and $\mathbf{Y}$ of size (q, p) whose components are respectively given by

$$\mathrm{X}_{ik} = \begin{cases} 0, & 1 \leq i \vee k \leq p, \\ \mathrm{J}_{ik}, & p < i \wedge k \leq q, \end{cases} \qquad \mathrm{Y}_{ik} = \begin{cases} 2\delta_{ik}, & 1 \leq i \leq p, \\ \mathrm{J}_{ik}, & p < i \leq q, \end{cases} \tag{4.67}$$

where the symbols $\vee$ and $\wedge$ mean *or* and *and* respectively, a given basis matrix $\underline{\mathbf{G}}''_j$ is implicitly expressed by

$$2\underline{\mathbf{G}}''_j = \mathbf{X}\underline{\mathbf{G}}''_j + \mathbf{Y}, \tag{4.68}$$

and computed by solving this linear system, which achieves the description of the method. However, the central issue still remains on the definition of the coupling function (4.60), or alternatively of the Jacobian in (4.61), in order to obtain a given basis matrix.

In the sequel, three intuitive and physical interpretations of these quantities are given but this does not represent an exhaustive presentation of all the possible solutions.

No-coupling

In the general case, the Jacobian matrix depends on the signal itself which leads to the definition of a dynamic basis matrix. In the sequel, the focus is put on static cases, that is considering a constant Jacobian, which allows to simplify equation (4.61) as

$$\underline{u}_i \simeq \sum_{k \in \mathbb{Q}_i} \mathrm{J}_{ik} \, \underline{u}_k, \tag{4.69}$$

and which leads to a linear reconstruction operation of the form

$$\underline{\mathbf{u}} \simeq \underline{\mathbf{G}}_j'' \hat{\underline{\mathbf{u}}}, \tag{4.70}$$

obtained from equation (4.57). The first trivial possibility is to consider that the modes are completely decoupled, which reads

$$\mathbf{J} = \mathbf{0}. \tag{4.71}$$

In this case, solving equation (4.68) gives

$$\underline{\mathrm{G}}_{1,ik}'' = \delta_{ik}. \tag{4.72}$$

Perhaps more explicitly, using the block representation introduced for the grid and sampling filters in (4.15) and (4.20) yields

$$\underline{\mathbf{G}}_1'' = \underline{\mathbf{G}}^\mathrm{T} = \begin{pmatrix} \mathbf{I} \\ \mathbf{0} \end{pmatrix}, \tag{4.73}$$

which means that all the estimated subgrid modes are null. It is worth noticing that this inverse satisfies the Moore–Penrose property (4.33)

$$(\underline{\mathbf{G}}_1'' \underline{\mathbf{G}})^* = \underline{\mathbf{G}}_1'' \underline{\mathbf{G}} = \begin{pmatrix} \mathbf{I} & \mathbf{0} \\ \mathbf{0} & \mathbf{0} \end{pmatrix}, \tag{4.74}$$

and is therefore the pseudo-inverse of the grid filter. As mentioned, this particular inverse is not the best to use for subgrid modelling. However, the physical meaning corresponds to the prediction of a fully resolved flow which can be instrumental for the large eddy simulation of transitional, or locally turbulent flows.

Probabilistic coupling

In order to generate an other basis matrix, a statistical approximation of the unknown high-frequency field which is based on a reciprocal probabilistic coupling between every pair of modes in the spectrum is introduced.

Integrating equation (4.61) and assuming that an elementary increment on any mode $\underline{u}_k$ has the probability $\mathbb{P}\left(i \mid k\right)$ to induce an increment on $\underline{u}_i$ implies

$$\underline{u}_i \simeq \sum_{k \,\in\, \mathbb{Q}_i} \mathbb{P}\left(i \mid k\right) \underline{u}_k, \tag{4.75}$$

which once again leads to a linear reconstruction of the form (4.70). The interpretation of this relation is that every existing mode $\underline{u}_k$ gives a probability of existence to the mode $\underline{u}_i$, $i \neq k$. For $\mathbb{P}\left(i \mid k\right)$ to be considered as a probability, it must satisfy the properties

$$\mathbb{P}\left(i \mid k\right) \in [0,1], \qquad\qquad\qquad \forall i, k \in \mathbb{Q}, \tag{4.76a}$$

$$\mathbb{P}\left(i\right) = \mathbb{P}\left(i \mid i\right) = \sum_{k \,\in\, \mathbb{Q}_i} \mathbb{P}\left(i \mid k\right) = 1, \qquad\qquad \forall i \in \mathbb{Q}. \tag{4.76b}$$

The condition (4.76b) expresses that every mode $\underline{u}_i$ does in fact exist. The discrete conditional probability $\mathbb{P}(i \mid k)$ can be mapped by some probability density function f

$$\mathbb{P}(i \mid k) = f(i, k), \tag{4.77}$$

which needs to be defined in order to obtain a given basis matrix. The probability density function must necessarily feature a number of properties to be mathematically and physically consistent.

1. f returns values comprised between 0 and 1 to comply with condition (4.76a)

$$f : \mathbb{R} \times \mathbb{R} \to [0, 1]. \tag{4.78}$$

2. Referring to (4.76b) and writing this condition in terms of the probability density function gives

$$\sum_{k \in \mathbb{Q}_i} f(i, k) = 1. \tag{4.79}$$

3. The probability for a mode $\underline{u}_i$ to exist, if mode $\underline{u}_k$ does, vanishes as the spectral distance between the modes tends to infinity, which reads

$$\lim_{|i-k| \to \infty} f(i, k) = 0. \tag{4.80}$$

4. The probability for the mode $\underline{u}_i$ to exist if it actually does is maximal, which implies

$$f(i, i) = 1, \qquad \partial_k f(i, k)|_{k=i} = 0, \qquad \partial_{kk} f(i, k)|_{k=i} < 0. \tag{4.81}$$

5. The probability for a mode $\underline{u}_i$ to exist if mode $\underline{u}_k$ monotonly decreases as the spectral distance between the modes increases, that is

$$\partial_k f(i, k)|_{k<i} > 0, \qquad \partial_k f(i, k)|_{k>i} < 0, \tag{4.82}$$

which is consistent with properties (3) and (4).

The mapping function could be determined analytically using simplified theories of turbulence, or empirically using reference data obtained by direct numerical simulation and experimental measurements, but also heuristically having some intuitions on the physics of the problem and satisfying the previous constraints.

However, for the sake of generality, this definition is temporarily left as a degree of freedom of the model and as a possible subject of further researches.

Linear-correlation coupling

Alternatively and starting again from equation (4.61), another approximation of the unknown high-frequency field can be obtained considering the Jacobian as a matrix of linear correlation coefficients between the modes

$$C_{ik} = \frac{\langle \underline{u}_i \underline{u}_k \rangle - \langle \underline{u}_i \rangle \langle \underline{u}_k \rangle}{[(\langle \underline{u}_i^2 \rangle - \langle \underline{u}_i \rangle^2)(\langle \underline{u}_k^2 \rangle - \langle \underline{u}_k \rangle^2)]^{1/2}}, \tag{4.83}$$

where the brackets denote an ensemble average which is equivalent to a time-average for ergodic systems. In other words, assuming that an elementary increment on any mode $\underline{u}_k$ is linearly correlated to the increment of $\underline{u}_i$ with C_{ik} as correlation coefficient allows to write (4.61) as

$$\underline{u}_i = \sum_{k \in \mathbb{Q}_i} C_{ik} \underline{u}_k, \tag{4.84}$$

which leads to a linear reconstruction like (4.70). The correlation coefficient C_{ik} can be mapped by some appropriate function g

$$C_{ik} = g(i, k), \tag{4.85}$$

which must satisfy the following properties for mathematical and physical consistency reasons.

1. g returns values comprised between -1 and 1 to comply with the definition of the correlation coefficient (4.83)

$$g : \mathbb{R} \times \mathbb{R} \rightarrow [-1, 1]. \tag{4.86}$$

2. The correlation coefficient between the modes $\underline{u}_i$ and $\underline{u}_k$ vanishes as the spectral distance between the modes tends to infinity, which reads

$$\lim_{|i-k| \rightarrow \infty} g(i, k) = 0. \tag{4.87}$$

3. The correlation of any mode $\underline{u}_i$ with itself is maximal, which implies

$$g(i, i) = 1, \qquad \partial_k g(i, k)|_{k=i} = 0, \qquad \partial_{kk} g(i, k)|_{k=i} < 0. \tag{4.88}$$

As mentioned in the case of the probabilistic coupling, the possible ways to define the mapping function are multiple. The choice among the possibilities is again delayed to preserve the generality of the approach within this theoretical presentation.

4.5.2 Closure of the approximation

Considering either the dynamic-basis (4.42) or the static-basis approximation (4.43), the use of multiple matrices to build an approximation of the admissible subspace requires to find an appropriate set of coefficients for the linear combination. Since the grid-filtered variables are the only available information about the state of the system, their determination can only rely on these quantities.

In the mono-element case $n = 1$, the single coefficient of the linear combination is trivially given by (4.41). Hence, the focus is put on the determination of the coefficients for $n \geq 2$.

Two-element basis

In the case of a two-element basis, the determination of the coefficients can be achieved introducing an additional filter, referred to as the test filter and represented by the matrix $\underline{\mathbf{T}}$ in such a way that the explicitly test-filtered variable reads

$$\overline{\underline{u}} = \underline{\mathbf{T}} \, \hat{\underline{u}} = \underline{\mathbf{T}} \, \underline{\mathbf{G}} \, \underline{u}, \tag{4.89}$$

where the test-filter matrix is of size (r, p), with $r \leq p$, and given by

$$\underline{\mathbf{T}}_{ij} = \delta_{ij}, \tag{4.90}$$

which represents therefore the equivalent of the grid filter at a coarser level. Assuming the scale similarity hypothesis which was first introduced in the framework of large eddy simulation by Bardina *et al.* [3], the same set of coefficients ω_i can be used for the approximate inversion of the

test and the grid filters. Considering that the matrix $\underline{\mathbf{T}}'$ represents the approximate inverse of the test filter, the error associated to the approximate inversion reads

$$\hat{\underline{\mathbf{e}}} = \hat{\underline{\mathbf{u}}} - \underline{\mathbf{T}}'\overline{\underline{\mathbf{u}}}, \tag{4.91}$$

where

$$\underline{\mathbf{T}}' = \omega_1\underline{\mathbf{T}}_1'' + \omega_2\underline{\mathbf{T}}_2'' = (1 - \theta)\underline{\mathbf{T}}_1'' + \theta\underline{\mathbf{T}}_2'', \tag{4.92}$$

with $\theta \in \mathbb{R}$ the weight parameter. In order to determine this parameter, as proposed by Lilly [37] in the framework of the dynamic Smagorinsky model [20], a least-squares minimisation of the form

$$\partial_\theta(\hat{\underline{\mathbf{e}}} \cdot \hat{\underline{\mathbf{e}}}) = 0 \tag{4.93}$$

is introduced. After some algebra, omitted for the sake of conciseness, the least-squares minimisation of the error (4.91) leads to

$$\theta = \frac{(\hat{\underline{\mathbf{u}}} - \breve{\underline{\mathbf{u}}}) \cdot \underline{\boldsymbol{\Delta}}\,\overline{\underline{\mathbf{u}}}}{\underline{\boldsymbol{\Delta}}\,\overline{\underline{\mathbf{u}}} \cdot \underline{\boldsymbol{\Delta}}\,\overline{\underline{\mathbf{u}}}}, \tag{4.94}$$

where the following definitions have been used

$$\underline{\boldsymbol{\Delta}} = \underline{\mathbf{T}}_2'' - \underline{\mathbf{T}}_1'', \tag{4.95}$$

$$\breve{\underline{\mathbf{u}}} = \underline{\mathbf{T}}_1''\overline{\underline{\mathbf{u}}}. \tag{4.96}$$

Following up on the idea of the scale similarity hypothesis, a possibility to define the test filter parameter is to conserve the ratio r/p = p/q, which trivially leads to

$$\mathrm{r} = \frac{\mathrm{p}^2}{\mathrm{q}}. \tag{4.97}$$

General case

Comparing the cases of the mono- and two-elements basis, the exponential growth of complexity for the determination of the coefficients is obvious. The generalisation to the n-dimensional basis is therefore quite involved.

However, one possibility is to obtain an adequate system of algebraic equations considering the partial derivatives of the inversion error (4.93) with respect to each coefficient, that is

$$\partial_{\omega_j}(\hat{\underline{\mathbf{e}}} \cdot \hat{\underline{\mathbf{e}}}) = 0, \qquad j \in \{1, \ldots, \mathrm{n} - 1\}, \tag{4.98}$$

which is currently the subject of further investigations. It is also possible to think that such an approach could require the use of n − 1 nested test-filtering levels. In any case, this extension seems mandatory for the improvement of the grid filter models.

4.6   Sampling filter models

This chapter is concluded by extending the view to another modelling strategy which is the dual version of the grid filter models. However, in a first lecture of this work, this last section could be considered as an appendix and be skipped to avoid confusions since it is not applied for subgrid modelling in the test cases presented hereafter.

In this perspective, recall from section 4.2.1, and more precisely from equation (4.8) that the evolution of the grid-filtered variables is sought in the framework of the grid filter models. Hence,

the dual approach would be to consider the evolution of the sampled variables. For this purpose, the sampled equations must be derived from the macroscopic equations (2.49) and are simply obtained by formally replacing the grid filter by the sampling filter in equation (4.8)

$$M\,\partial_t \tilde{u} + A(\tilde{u}) = \tilde{f} + [A, \mathcal{S}\star](u). \tag{4.99}$$

Recalling from sections 4.2.2 and 4.2.3 that the grid filter conserves the modal values and the sampling filter conserves the nodal ones, the right nodal values are sought instead of the right modes.

Following the approach introduced in equation (4.10), an approximation of the subgrid commutator can be obtained by introducing the approximate sampling filter $\tilde{\mathcal{S}}\star$, dual of the modelling filter $\tilde{\mathcal{G}}\star$, which yields

$$[A, \mathcal{S}\star](u) \simeq [A, \tilde{\mathcal{S}}\star](\tilde{\mathcal{S}}^{-1} \star \hat{u}) = [A, \tilde{\mathcal{S}}\star](\hat{u}). \tag{4.100}$$

Using an approximation of the original quantities obtained from their grid-filtered counterpart

$$\mathbf{u} \simeq \mathbf{G}'\hat{\mathbf{u}}, \tag{4.101}$$

an approximation of the sampling filter is given by

$$\tilde{\mathbf{u}} = \mathbf{Su} \simeq \mathbf{SG}'\hat{\mathbf{u}} = \tilde{\mathbf{S}}\hat{\mathbf{u}}, \tag{4.102}$$

which formally represents the inverse change of variable compared to equation (4.23). However, in order to be strictly equivalent, the following properties have to be satisfied

$$\tilde{\mathbf{S}}\tilde{\mathbf{G}} = \mathbf{SG}'\mathbf{GS}' \simeq \mathbf{I}, \tag{4.103}$$

$$\tilde{\mathbf{G}}\tilde{\mathbf{S}} = \mathbf{GS}'\mathbf{SG}' \simeq \mathbf{I}, \tag{4.104}$$

which is not exactly achievable considering equations (4.29) and (4.35). Hence, the grid filter models and the sampling filter models can not and do not lead to the same modelling.

This last section raises a fundamental and open question about the information which is sought in the framework of a large eddy simulation. Is the aim to obtain the right modes, or alternatively the right nodal values? Answering this key question defines the filter which shall be applied to the macroscopic equations and thereby the modelling approach which is required.

However and as mentioned above, the modelling strategy which is retained in the sequel relies on the grid filter models exclusively. The dual approach represented by the sampling filter models is thus left as a subject of further investigations.

Chapter 5

Large eddy simulation of inertial turbulence

The validation of subgrid models and their underlying hypotheses requires the use of reference data which shall be an exact solution of the macroscopic equations. These data can be obtained by direct numerical simulation or by experimental measurements and be used in two different ways, *i.e. a priori* or *a posteriori*. In the sequel the focus is put on the *a posteriori* validation method which is briefly discussed in the particular case of the grid filter models. For a more general description, the reader is referred to [52].

In the framework of the *a posteriori* validation, the results of the large eddy simulation are directly compared to the grid-filtered exact solution arising from a direct numerical simulation or experimental data. In contrast with the *a priori* method, this procedure takes into account the effect of the modelling errors on the evolution of the system to be described. As detailed by Piomelli *et al.* [47], models yielding poor *a priori* results can be satisfactory *a posteriori* and inversely. It is therefore more pertinent to validate the models *a posteriori* since this corresponds to their final use.

As a first step towards the validation of the grid filter models and the corresponding modelling approach described in chapter 4, the direct numerical simulation of a classical problem of inertial turbulence is considered. Moreover, applying the grid filter models for such a classical problem allows to compare their efficiency with the modelling methods partially or fully based on functional modelling, which are specifically meant for the modelling of inertial turbulence.

Among all benchmark problems which could be chosen, the focus is put on the lid-driven cavity flow considering a Newtonian fluid and that the flow is isothermal and incompressible in such a way that the particular Navier–Stokes model (2.20)-(2.21) is applicable. Although the geometry is very simple, the flow presents complex physical phenomena, no direction of homogeneity and a large variety of flow conditions, which represents a challenging problem in terms of subgrid modelling.

5.1 Lid-driven cubical cavity flow

The large eddy simulation presented hereafter refer to the flow in the lid-driven cubical cavity performed at Reynolds number of 12'000. This particular choice is motivated by the availability of large eddy simulation results obtained with other subgrid models, which enables a better assessment of the relative performance of the grid filter models. Hence, it clearly appears that this case only represents a first validation step of the approach presented herein.

The direct numerical simulation was performed by Leriche and Gavrilakis and was reported in [35, 36]. The flow domain consists in a cubical cavity $\mathbf{\Omega} = [-\mathrm{L}, \mathrm{L}]^3$, the axis origin being assigned at the centre of the domain represented in figure 5.1.

The flow is driven by imposing a non-zero velocity parallel to the x-axis on the "top" wall. On the other walls, no-slip conditions are imposed. The moving wall will be referred to as the lid while the faces normal to the z-axis will be referred to as side walls. The upstream and downstream walls are normal to the x-axis and characterised by their relative position with respect to the lid motion.
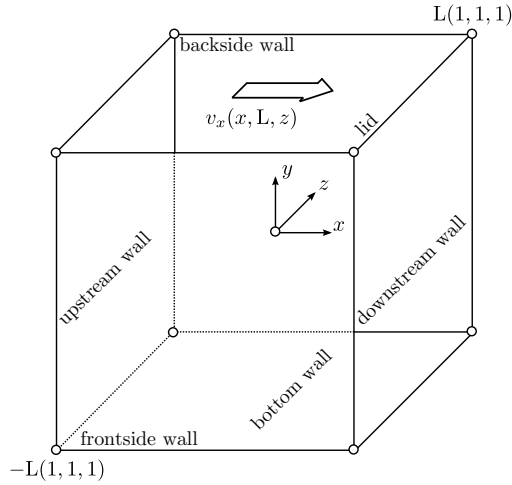
Fig. 5.1: Lid-driven cubical cavity. Geometry and definitions.

The opposite face to the lid is called the bottom wall. As far as the velocity imposed on the lid is concerned, the unit velocity induces severe discontinuities along the top edges. In order to avoid these defects, the imposed velocity on the lid is given by the regularised polynomial expression

$$v_x(x, \mathrm{L}, z) = \mathrm{V}(1 - (x/\mathrm{L})^{\mathrm{r}})^2(1 - (z/\mathrm{L})^{\mathrm{r}})^2, \tag{5.1}$$

$$v_y(x, \mathrm{L}, z) = 0, \tag{5.2}$$

$$v_z(x, \mathrm{L}, z) = 0, \tag{5.3}$$

with V the reference velocity and the regularisation parameter chosen as r = 18 for the sake of consistency with the direct numerical simulation [35]. According to equation (2.31), the Reynolds number is defined as

$$\mathrm{Re} = \frac{2\mathrm{LV}}{\nu} = 12'000. \tag{5.4}$$

For such Reynolds numbers, the flow over most of the domain is laminar and turbulence develops near the cavity walls. Its main feature is a large scale recirculation which spans the cavity in the z-direction. Aside this large flow structure, the relatively high momentum fluid near the lid is deviated by the downstream wall into a down flowing nonparallel wall jet which separates ahead of the bottom wall. A region of high pressure and dissipation located at the top of the downstream wall results from this deviation. The energy resulting from the impingement of the separated layer against the bottom wall is lost to turbulence and partly recovered by an emerging wall jet near the upstream wall where the flow slows down and relaminarizes during the fluid rise. The flow is also characterised by multiple counter-rotating and recirculating regions at the corners and edges of the cavity.

The large eddy simulation is started from an instantaneous velocity field obtained from the reference data in the statistically-steady range. This field is projected onto the spatial discretization used for the large eddy simulation. The projective grid filter representing this operation induces the unrecoverable loss of the subgrid scales.

5.2   Numerical method

As detailed throughout this work, subgrid modelling in the case of the grid filter models is closely linked to the numerical method and more precisely to the spatial discretizations of the direct and

the large eddy simulations which define the grid filter itself. Therefore, the brief description given hereafter is mandatory in the perspective of the required grid filter modelling.

5.2.1 Direct numerical simulation

As reported in table 5.1, the reference data were obtained with a mono-domain Chebyshev collocation method on a grid composed of 129 collocation points in each spatial direction, which means that the size of the functional space (3.4) is $q_i = 129$.

	(E_x, E_y, E_z)	(q_x, q_y, q_z)	(p_x, p_y, p_z)	Δt
SEM	$(8, 8, 8)$	$(17, 17, 17)$	$(9, 9, 9)$	$2.0\ 10^{-3}$
CCM	$(1, 1, 1)$	$(129, 129, 129)$	$-$	$2.5\ 10^{-3}$

Table 5.1: Numerical parameters of the direct numerical simulation (q_i) and large eddy simulation (p_i) for the Chebyshev collocation method (CCM) and the spectral elements method (SEM).

The reference data are re-interpolated from the Chebyshev grid onto a spectral elements grid composed of 8 elements with 17 interpolation points in each direction, leading to a global number interpolation points of 129^3. The loss of information due to this re-interpolation is negligible compared to the effect of the grid filter associated with the large eddy simulation, the number of interpolation points being conserved.

5.2.2 Large eddy simulation

For the large eddy simulation, the spatial discretization has 8 elements with 9 interpolation points in each direction, that is 65^3 grid points in total, which is equivalent the discretization used for the large eddy simulation reported by Zang *et al.* [62] for a slightly lower Reynolds number. This grid has therefore twice less points per spatial direction than the direct numerical simulation grid. As shown in figure 5.2, the spectral elements are unevenly distributed in order to resolve the boundary layers along the lid and the downstream wall.
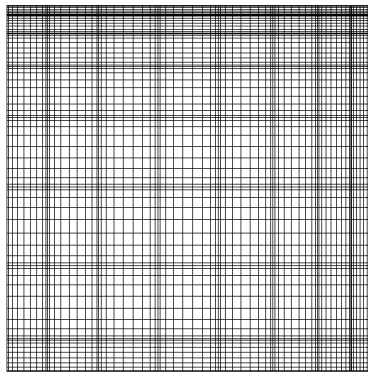
Fig. 5.2: Spectral elements grid in any z-normal plane.

The interpolation points and numerical quadratures rules are based on the Gauss–Lobatto–Legendre distribution with p_i points for the velocity and on the Gauss–Legendre rule with $p_i - 2$ points for the pressure. This spectral elements method avoids the presence of spurious pressure modes as proved by Maday and Patera [38, 39].

Standard time-integrators used with the spectral elements method handle the viscous linear term and the pressure implicitly by a backward differentiation formula of order two in order to avoid stability restrictions such that $\nu \Delta t \leq \mathrm{C}/\mathrm{p}_i^4$, while all non-linear contributions, including the discretized subgrid commutator, are computed explicitly by a second-order extrapolation method which has to abide to the Courant–Friedrichs–Lewy restrictions of the form

$$\max(||\boldsymbol{v}||)\Delta t \leq \mathrm{C}/\mathrm{p}_i^2. \tag{5.5}$$

For these reasons, the time-step chosen for the large-eddy simulation is smaller than the one of the direct numerical simulation, see table 5.2. Moreover, this allows to ensure that the filtering associated to the temporal discretization is negligible, as assumed in equation (2.37) and required for the grid filter models.

The implicit part is solved by a generalised block decomposition with the pressure correction algorithm described in section 3.5 and the splitting operator given in (3.62). The overall accuracy-order in time of the method is two.

5.3   Grid filter modelling

According to the approach described in chapter 4, grid filter modelling exclusively relies on the approximate inversion of the sampling filter which allows to compute the modelling filter defined in equation (4.23).

However, using the particular sampling filter inverse proposed in section 4.4 also requires to find an approximate inverse of the grid filter for the approximation of the weight matrix in equation (4.56). Hence, th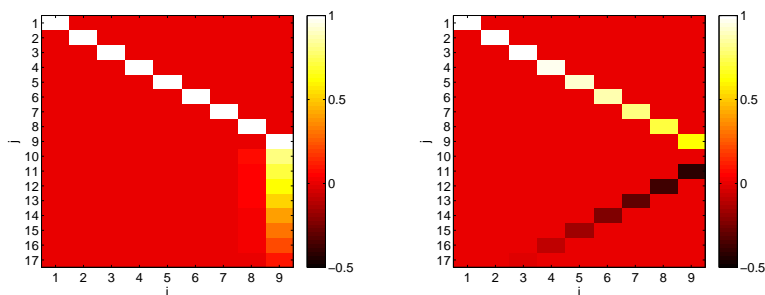e approximate inverse of the grid and sampling filters used for the large eddy simulation of the lid-driven cavity flow are presented hereafter.

5.3.1   Approximate inverse of the sampling filter

Since the initial condition of the large eddy simulation is a velocity field taken from the statistically-steady-state range of the direct numerical simulation, it is reasonable to also assume that the large eddy simulation will reach a statistically-steady state very quickly, but only if subgrid modelling is efficient which was already discussed by Bouffanais in [11].

In this case, time-averaging can be considered as equivalent to an ensemble-averaging. Hence, introducing the Reynolds statistical decomposition for the approximate inverse of the sampling filter reads

$$\underline{\mathbf{S}}' = \langle \underline{\mathbf{S}}' \rangle + \underline{\mathbf{S}}'^{\circ}. \tag{5.6}$$

Neglecting the fluctuating part of the operator and approximating the averaged counterpart using the initial conditions of the large eddy simulation allows to write

$$\underline{\mathbf{S}}' \simeq \langle \underline{\mathbf{S}}' \rangle \simeq \underline{\mathbf{U}}_0 \mathbf{S}^{\mathrm{T}} (\mathbf{S}\,\underline{\mathbf{U}}_0 \mathbf{S}^{\mathrm{T}})^{-1}, \tag{5.7}$$

which is obtained using equation (4.55) and where the subscript 0 denotes the initial time-level, that is the initial conditions. According to equation (4.56), the initial weight matrix is given by

$$\underline{\mathbf{U}}_{0,ij} \simeq \underline{\mathbf{G}}'_{ik}\hat{\underline{\mathbf{u}}}_{0,k}\delta_{ij}. \tag{5.8}$$

The approximations in (5.7) allow to obtain a linearised inverse of the sampling filter which does not require to be re-evaluated as the state of the system changes, thereby diminishing the overall computational costs of the large eddy simulation.

It is worth noticing that this approach will be used for the large eddy simulation reported hereafter but would not be applicable for transitional flows, that is for flows which are not in a statistically-steady state.

5.3.2   Approximate inverse of the grid filter

In order to evaluate the weight matrix with equation (5.8), the approximate inverse of the grid filter must also be defined. As a first validation step, the straightforward case of the single element and static-basis approximation (4.43) is considered.

This modelling choice prevents the use of the Moore–Penrose pseudo-inverse obtained by the no-coupling approach described in section 4.5.1 since a null subgrid field would always be predicted. Instead, the focus could be put either on the probabilistic or the linear-correlation coupling between the modes which requires the definition of the mapping function appearing in equation (4.77) or (4.85).

The coupling approach based on the linear correlation between the modes is discarded since an appropriate mapping function could not be heuristically defined based on the three required properties (4.86)-(4.88). This modelling strategy therefore requires more advanced theoretical investigations based on theories of turbulence or on the analysis of direct numerical simulation data.

In the probabilistic case, the mapping function has to abide to the five constraints (4.78)-(4.82) which enables a straightforward and heuristic definition. Moreover, and according to the central limit theorem, which states that the sum of a large number of independent and identically-distributed random variables are approximated by a normal distribution, the probability density function can be chosen as

$$f(i,j) = \exp\left[-\tfrac{1}{2}\left(\tfrac{j-i}{\sigma_i}\right)^2\right],\tag{5.9}$$

which matches the required constraints and where the parameters σ_i are determined according to property (4.79). This definition allows to obtain the approximate inverse of the grid and sampling filters which are shown in figure 5.3. As it can be noticed on this figure, the subgrid field predicted

Fig. 5.3: Approximate inverse of the grid (left) and sampling (right) filters used for the large eddy simulation of the lid-driven cavity flow.

with this approximate inverse of the grid filter mainly depends on the high-frequency part of the computed modes. In consequence, the subgrid model vanishes in the regions where the flow is fully resolved, which is mandatory since the lid-driven cavity flow is only locally turbulent for the moderate Reynolds number chosen in this study.

5.3.3   Modelling filter

Using the approximate inverse of the sampling filter represented in figure 5.3 allows to compute the modelling filter according to equation (4.23)

$$\underline{\tilde{\mathbf{G}}} = \underline{\mathbf{G}}\,\underline{\mathbf{S}}'. \tag{5.10}$$

The modelling filter obtained by this procedure is represented in figure 5.4 for the finite and the spectral elements methods in order to illustrate the major dependency of the modelling on the spatial discretization method. Moreover, the filters arising from this approach are compared with
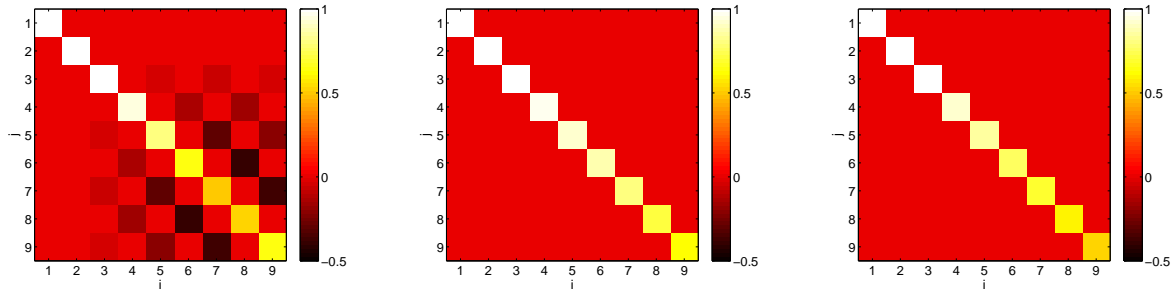
Fig. 5.4: Modelling filter obtained for the finite elements (left) and for the spectral elements (centre) compared to the empirical filter (right).

the empirical filter used by Habisreutinger *et al.* in [25] for an approximate deconvolution model and for the identical large eddy simulation. This filter is defined by the diagonal matrix

$$\underline{\mathbf{K}}_{ij} = \frac{\delta_{ij}}{1 + \left(\frac{\eta\,\max(0, i-2)}{\mathrm{p}_i}\right)^{\gamma}}, \qquad \eta, \gamma \in \mathbb{R}^{+}, \tag{5.11}$$

where the filtering rate $\eta = 1.25$ and the filtering exponent $\gamma = 2.0$ are empirically chosen. The first important observation on these figures is that the continuity constraint (3.26) is satisfied in all cases.

   The correspondence between the empirical filter and the modelling filter obtained in the case of the spectral elements is quite impressive, especially considering that the modelling filter depends on the spatial discretizations of both the direct and large eddy simulations but also on the approximate inverse of the sampling filter and the statistically-steady state of the flow. While the empirical filter is by definition diagonal, this property seems quite involved to demonstrate for the modelling filter since the definition of the sampling operation relies on the inversion of a full matrix, see equation (4.19).

   Since the modelling and the empirical filters are diagonal, they can be quantitatively compared in figure 5.5 which represents their diagonal coefficients. As one can notice, the coefficients are relatively close, the maximum relative difference being of the order of 17%. The grid filter model approximately corresponds to the empirical filter with a filtering rate of 1.05 and an exponent of 2.5. This strong result already indicates that the grid filter models are consistent since the results obtained by Habisreutinger *et al.* in [25] are satisfying in terms of accuracy.

5.4   *A posteriori* validation

In this section, the results of the large eddy simulation obtained using the grid filter model described above are compared with the grid-filtered reference results by analysing the first- and the second-
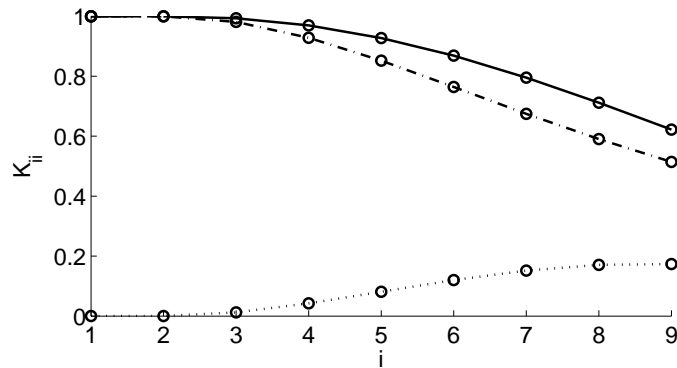
Fig. 5.5: Diagonal coefficients of the modelling filter obtained using the grid filter model (solid line) compared to the empirical filter (dash-dotted line). The relative difference between the grid filter model and the empirical filter is represented with a dotted line.

order statistics of the flow. The measurements reported by Leriche and Gavrilakis [36] were taken in the mid-plane $z/L = 0$, which is the statistical symmetry plane of the flow domain.

The statistics for the large eddy simulation are based on a sampling approximately 10 times smaller than the one of the reference data. More precisely 400 samples are collected over 80 adimensional time units, while the reference statistics were obtained using 4'000 samples extracted over an integration range of 1'000 adimensional time units. Therefore, the large eddy simulation statistics are not expected to be identical to the reference ones, especially the second-order ones.

5.4.1   Comparison of the first-order statistics

In order to verify that the spatial discretization used for the large eddy simulation is coarse enough and does not resolve all scales of the flow, an implicit large eddy simulation of the lid-driven cubical cavity flow was performed with exactly the same physical and numerical parameters as the ones reported in table 5.1. In this particular context, the implicit large eddy simulation corresponds to the resolution of

$$\boldsymbol{M} \, \partial_t \hat{\boldsymbol{u}} + \boldsymbol{A}(\hat{\boldsymbol{u}}) = \hat{\boldsymbol{f}} \tag{5.12}$$

instead of (4.11), that is performing a large eddy simulation without model. The reader is referred to [52] for more details about the possible interpretations of the implicit large eddy simulation in a more general framework. The resolution of (5.12) can also be interpreted as an under-resolved direct numerical simulation.

The comparisons with the reference results are performed by plotting identical series of contour levels of the average velocity. As it can be observed on figure 5.6, the implicit large eddy simulation is totally inoperative in the particular context of this simulation. Even first-order statistics are far from being well predicted, not to mention second-order ones. These results allow to confirm the sufficient under-resolution of the flow using the same spatial discretization that Zang *et al.* [62] used for a lower Reynolds number.

Figure 5.6 also displays the average values of the velocity field obtained with the grid filter model in the mid-plane of the cavity. A rapid overview of these figures indicates that this approach provides results very close to the reference, which is even highlighted by the huge difference with the implicit large eddy simulation. Secondary corner eddies located above the bottom wall and below the lid next to the upstream wall are correctly predicted in the mean flow.
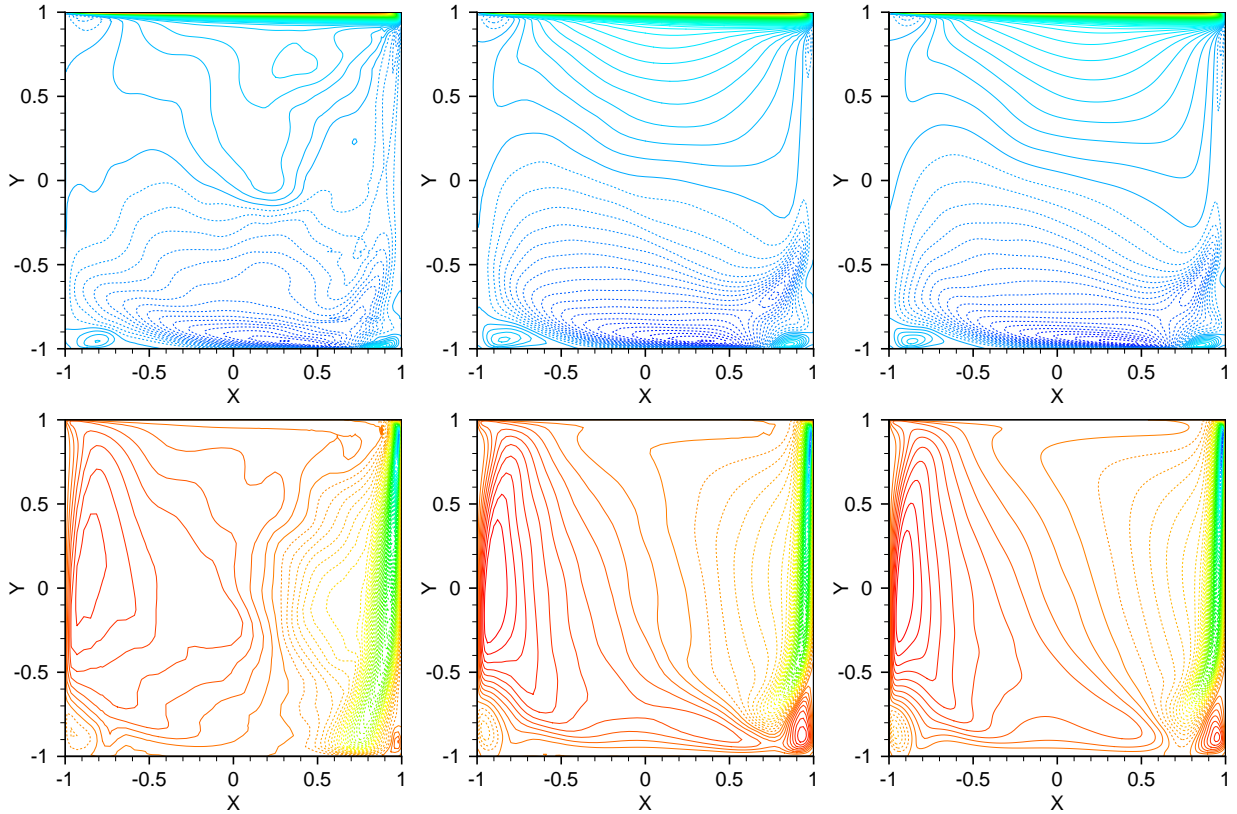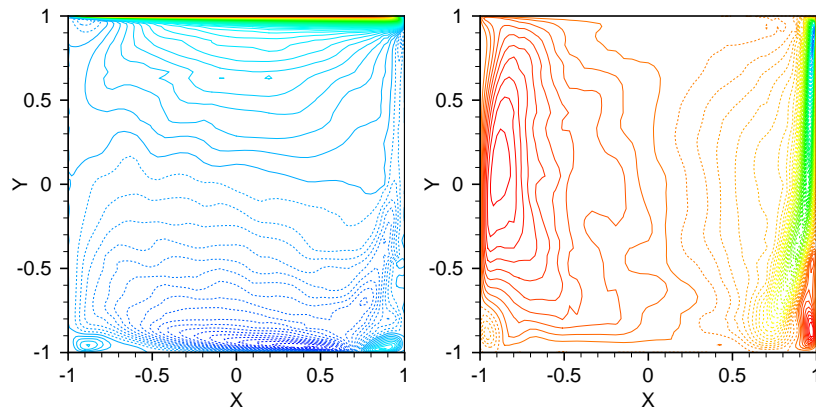
Fig. 5.6: Contours of $\langle \hat{v}_x \rangle$ from $-.2$ to 1 by increments of $.01$ (top), contours of $\langle \hat{v}_y \rangle$ from $-.7$ to $.1$ by increments of $.01$ (bottom). Implicit large eddy simulation (left), large eddy simulation with the grid filter model (centre), direct numerical simulation (right). Colour scale from blue to red. Dashed contours correspond to negative levels.

5.4.2 Comparison of the second-order statistics

In order to assess the relative performance of the grid filter models, the comparison with classical modelling approaches is presented for the second-order statistics. A classical approximate deconvolution model coupled with the dynamic mixed-scale model [25] for the hard-deconvolution problem is considered. Moreover, in order to perform comparisons with fully functional modelling approaches, the results obtained with the dynamic mixed-scale model [52] are also reported.

In an attempt to provide a comprehensive assessment of the performances of the considered subgrid models, the determination of the Reynolds stress tensor components has been envisaged as a challenge in the framework of the lid-driven cubical cavity flow.

In particular, figure 5.7 displays the very low-amplitude cross-term $\langle \hat{v}_x^\circ \hat{v}_y^\circ \rangle^{1/2}$ in the symmetry plane of the cavity. The analysis of these results showcases the improvement achieved in terms of subgrid modelling by both deconvolution-based approaches as compared to the purely functional modelling, which was already observed in [25]. Indeed, the deconvolution-based models reproduce quite accurately the intense-fluctuations zones in the mid-plane $z/h = 0$, and more specifically in the vicinity of the downstream corner eddy.

Moreover, comparing the deconvolution-based approaches between themselves shows that the grid filter models provide a better modelling in the high-intensity region located near the bottom-right edge of the cavity. The same tendencies are observed for all the other components of the
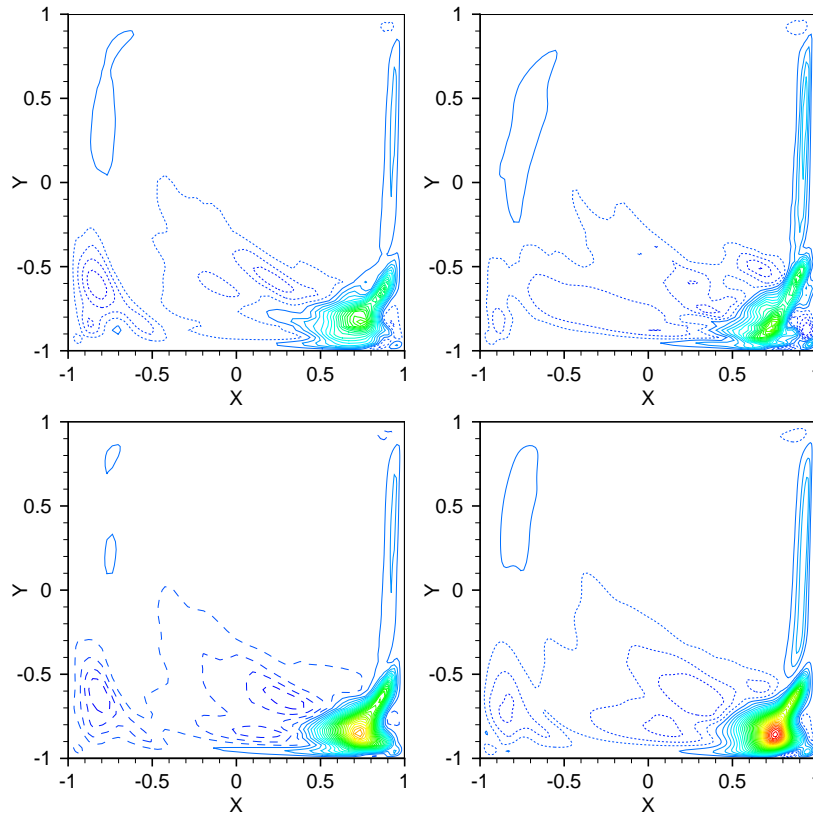
Fig. 5.7: Contours of $\langle \hat{v}_x^{\circ} \hat{v}_y^{\circ} \rangle$ from $-.0007$ to $.0065$ by increments of $.0002$. Approximate deconvolution model coupled with the dynamic mixed-scale model (top-left), dynamic mixed-scale model (top-right), grid filter model (bottom-left), direct numerical simulation (bottom-right). Colour scale from blue to red. Dashed contours correspond to negative levels.

Reynolds-stress tensor.

In consequence, gradually removing functional modelling seems to provide subgrid modelling of increasing quality. However, it is worth stressing that this comment only applies to this particular case and is certainly not a general statement.

5.5 Further decreasing the spatial resolution

In order to provide a clearer picture of the modelling performance related to the grid filter models, the Reynolds number could be increased or the spatial discretization could be further coarsened. Due to the availability of the direct numerical simulation data, the second option is considered hereafter.

However, coarsening of the spatial discretization in the particular case of the lid-driven cavity flow raises a fundamental question. Figure 5.8 displays the error on the representation of the regularised velocity profile

$$\hat{e}(x, z) = \hat{v}_x(x, \mathrm{L}, z) - v_x(x, \mathrm{L}, z), \tag{5.13}$$

which is imposed on the lid for different values of p_i. While the boundary conditions are almost exactly represented in the reference case $\mathrm{p}_i = 9$, an error on the definition of the problem is clearly introduced for lower polynomial degrees. In this case, how to justify the *a posteriori* comparison
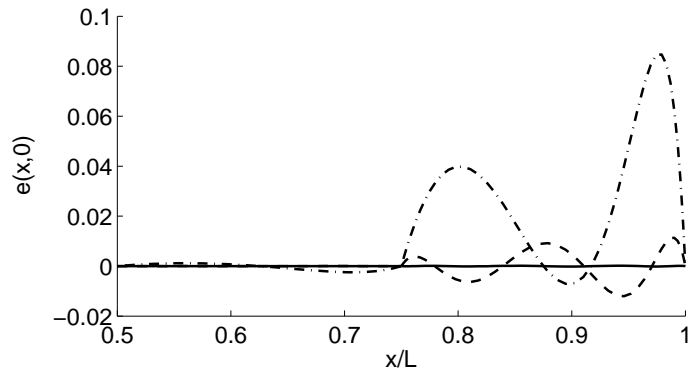
Fig. 5.8: Error on the representation of the regularised velocity profile for different values of p_i and in the mid-plane of the cavity. The reference case $p_i = 9$ is represented with a solid line, $p_i = 6$ with a dashed line and $p_i = 3$ with a dash-dotted line.

of the results if the definition of the problem, *i.e.* the boundary conditions, is not the same for the direct and the large eddy simulation. Moreover, since turbulent flows display a chaotic behaviour, the slightest disturbance in the initial or boundary conditions can lead to enormous differences in the evolution of the system. In order to overcome this issue and efficiently compare the results, one possibility would be to perform a direct numerical simulation with a lower regularisation parameter in such a way that the velocity profile would be correctly represented even at low resolution.

For instance, the first-order statistics obtained in the case $p_i = 6$ are presented in figure 5.9, which corresponds to a 41^3 spatial discretization, thereby retaining approximately 3% of the nodes present in the direct numerical simulation grid. The corresponding implicit large eddy simulation can not be presented since the 80 adimensional time units could not be computed due to numerical instabilities arising from the too important under-resolution of the flow. While the subgrid modelling performed by the grid filter models allows to maintain the stability of the simulation, the first-order statistics are not accurately predicted. Focusing on the wiggles of $\langle \hat{v}_y \rangle$ located near the top-right

Fig. 5.9: Contours of $\langle \hat{v}_x \rangle$ from $-.2$ to 1 by increments of $.01$ (left), contours of $\langle \hat{v}_y \rangle$ from $-.7$ to $.1$ by increments of $.01$ (right) for $p_i = 6$. Colour scale from blue to red. Dashed contours correspond to negative levels.

edge of the cavity, the influence of the boundary conditions appears clearly. Hence, the low accuracy of the first-order statistics is assumed to be partly induced by the incorrect representation of the

boundary conditions and by the dismal performance of the subgrid model. However, this analysis still provides a clear illustration of the remaining challenges in terms of improvement of the grid filter modelling.

Chapter 6

Simulation of elastic turbulence

The results reported in chapter 5 allow to validate the grid filter models for the large eddy simulation of a complex flow, however only considering a Newtonian fluid. As a next step, the aim is to extend the approach to other fluids and analyse its ability for the modelling of subgrid scales which do not behave like in a Newtonian fluid flow.

Among the earliest observations of turbulence occurring in flows of more complex fluids, Toms [59] experimentally discovered that the addition of a small amount of polymer into a Newtonian solvent can reduce the frictional drag. This is known as the drag reduction phenomenon which occurs in the high-Reynolds regime and for small Deborah numbers, namely for weakly elastic fluids. Hence, the physics involved in such cases only represents a slight modification as compared to the one of the purely inertial turbulence.

More recently, Groisman and Steinberg [23] observed the development of an elastic turbulence regime in flows of highly viscous polymer solutions and in the limit of strong elasticity, that is at very low Reynolds and high Deborah numbers. In this case, the development of turbulence is not governed by inertial effects but by the elastic stresses of the flow. Since this phenomenon relies on a physics which is radically different from the one of the inertial turbulence, it represents a very challenging problem in terms of subgrid modelling, which has never been addressed to the author's knowledge and which is well suited to extend the validity domain of the grid filter models.

The first issues to face in the simulation of elastic turbulence are the numerical instabilities which are particularly important at large Deborah numbers. This chapter is thus presented in close connection with this topic which is known as the high-Deborah or high-Weissenberg number problem.

6.1 Direct numerical simulation in periodic domains

The difficulty to compute numerically viscoelastic fluid flows is expressed in terms of the dimensionless Deborah number (2.35) which is a measure of the elasticity of the fluid. As reported by Owens and Phillips [45], the choice of different rheological models only changes the breakdown process, not necessarily eliminates it altogether.

The high Deborah-number problem may arise from the difficult problem of enforcing appropriate boundary conditions in order to obtain a mathematically well-posed problem. Instabilities of Hadamard type [45] can also lead to the blow-up of the simulations. They are associated to the unphysical loss of positiveness of the conformation tensor which is induced by the accumulation of numerical errors during the computation of the flow dynamics.

Considering only fully periodic domains, like in the available numerical investigations of elastic turbulence [5,58], the issue that remains to avoid the loss of positiveness of the conformation tensor is to efficiently control the discretization errors in space and in time, which is addressed in the next section.

6.1.1   Numerical method

Spatial discretization

The error associated to the spatial discretization is directly linked to the truncation error introduced in equation (3.5). Therefore, an estimation of this quantity is required in order to correctly adapt the truncation parameter q as a function of the state of the system.

Since only periodic domains are considered, the spatial discretization relies on the Fourier collocation method presented in section 3.3, which seems a rather natural and straightforward choice. For sufficiently regular functions such as those expected in the framework of incompressible fluid mechanics, the modal coefficients decay exponentially as a function of the wave-number. A good indicator of the truncation error is therefore given by the estimation of the high-frequency part of the computed spectrum.

For instance, the difference between the aliased and de-aliased products of the unknown, see (3.35) and (3.36), reads

$$\mathbf{e} = (\mathbf{\Phi}_q^q \underline{\mathbf{u}} . \mathbf{\Phi}_q^q \underline{\mathbf{u}}) - \mathbf{G}_r^q (\mathbf{\Phi}_q^r \underline{\mathbf{u}} . \mathbf{\Phi}_q^r \underline{\mathbf{u}}), \tag{6.1}$$

and is directly proportional to the magnitude of the modes comprised between q/2 and q. Hence, choosing q in such a way that the aliasing error satisfies the criterion

$$|\mathbf{e} \cdot \mathbf{e}| \leq \tau, \tag{6.2}$$

where $\tau \in \mathbb{R}$ represents the error tolerance, and assuming the exponential decay of the modal coefficients implies that the truncation error (3.5) is bounded by

$$|\boldsymbol{\varepsilon}_x \cdot \boldsymbol{\varepsilon}_x| \leq C\tau, \tag{6.3}$$

with $C \in \mathbb{R}$ a given constant. Consequently, adapting q to satisfy (6.2) enables the indirect control of the error associated with the spatial discretization.

Time-integration

For time-integration, an explicit Runge-Kutta scheme of order 8 based on the method of Dormand and Prince is used. It is described by Hairer *et al.* in [26] and available at the author's website[1] as a fortran 77 subroutine. It features embedded error estimators of order 5 and 3 which enables the adaptation of the time-step in such a way that the local integration error (3.55) satisfies the constraint

$$||\boldsymbol{\epsilon}_t||_\infty \leq \tau, \quad \forall t. \tag{6.4}$$

Combined with the control of the spatial error, this algorithm allows to control the overall error associated with the numerical approximation which can lead to the loss of positiveness of the conformation tensor.

6.1.2   Viscoelastic Taylor–Green vortex

Given the order of accuracy of both the spatial and temporal discretization methods, it would be conceivable to solve the governing equations (2.32)-(2.34) to machine precision. However, in practice, the computational costs for reaching such a precision become prohibitive. Hence, the error tolerance is raised up to $\tau = 10^{-12}$, the time-step and the number of modes being adapted accordingly.

---

[1]http://www.unige.ch/~hairer/software.html

Initial conditions

In order to validate this numerical approximation framework for the simulation of high-Deborah number flows, a modified version of the three dimensional Taylor–Green vortex as presented by Brachet *et al.* [13] is considered. The initial condition for the velocity field is given by

$$\boldsymbol{v}_0 = \frac{2V}{\sqrt{3}} \begin{pmatrix} (\alpha + \frac{2\pi}{3})\sin(kx)\cos(ky)\cos(kz) \\ (\alpha - \frac{2\pi}{3})\cos(kx)\sin(ky)\sin(kz) \\ \sin(\alpha)\cos(kx)\cos(ky)\sin(kz) \end{pmatrix}, \tag{6.5}$$

with V the reference velocity, the free parameter chosen as $\alpha = \pi/2$ and the wave-number

$$k = \frac{2\pi n}{L}, \qquad n \in \mathbb{N}, \tag{6.6}$$

L representing the size of the three-dimensional periodic domain $\boldsymbol{\Omega} = [0, L]^3$. This must be extended to the viscoelastic case by the initial condition of the conformation tensor which is arbitrarily chosen as

$$\boldsymbol{\chi}_0 = \boldsymbol{I}. \tag{6.7}$$

Using expression (2.28) to retrieve the extra-stress tensor yields

$$\boldsymbol{\tau}_0 = 2\mu\dot{\boldsymbol{\gamma}}_0, \tag{6.8}$$

which reduces to the single contribution of the Newtonian solvent. The viscoelastic stresses are thus null at the initial time, which means that the polymers are initially at the equilibrium state. The dimensionless numbers which characterise the flow are defined as

$$De = \lambda V k, \qquad Re = \frac{V}{(1 + \eta)\nu k}, \tag{6.9}$$

where the 2π scaling coefficient is omitted. In the sequel, the Reynolds number is fixed to $Re = 1$, the polymer viscosity coefficient to its typical value $\eta = 10/13$, while the Deborah number is considered as a parameter.

Evolution of the energy

In the case of an Oldroyd-B fluid which is composed of a suspension of Hookean dumbbells in a Newtonian solvent, the total energy of the flow E is the sum of the kinetic energy K and the elastic one stored by the deformation of the dumbbells H, that is

$$E(t) = K(t) + H(t) = \frac{1}{2}\langle \boldsymbol{v} \cdot \boldsymbol{v} + \text{tr}\,\boldsymbol{\tau}_p \rangle. \tag{6.10}$$

In order to get some insight about the physics involved in the flow, the conversion of energy between the kinetic and elastic forms is considered. As shown in figure 6.1, the elastic energy is null at initial time, which is in accordance with equation (6.8), and increases at first passing a peak which is less marked and occurs later with increasing the Deborah number. In order to understand this mechanism, consider the time-derivative of the polymer contribution to the extra-stress tensor at the initial time

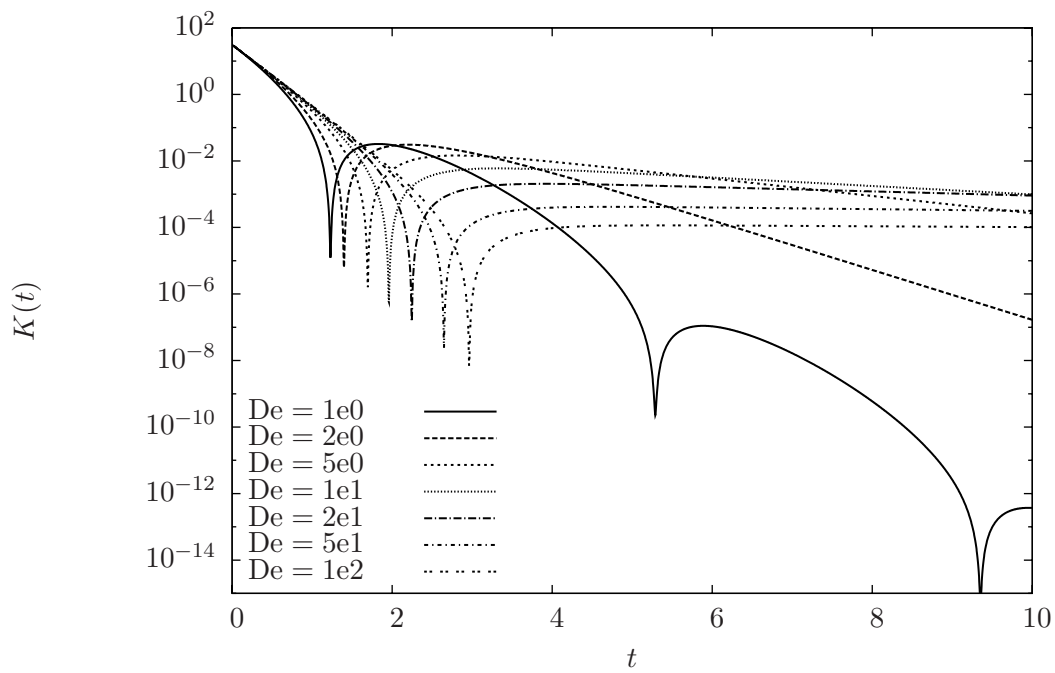$$\partial_t \boldsymbol{\tau}_p(t = 0) = \frac{2\eta}{De}\dot{\boldsymbol{\gamma}}_0. \tag{6.11}$$
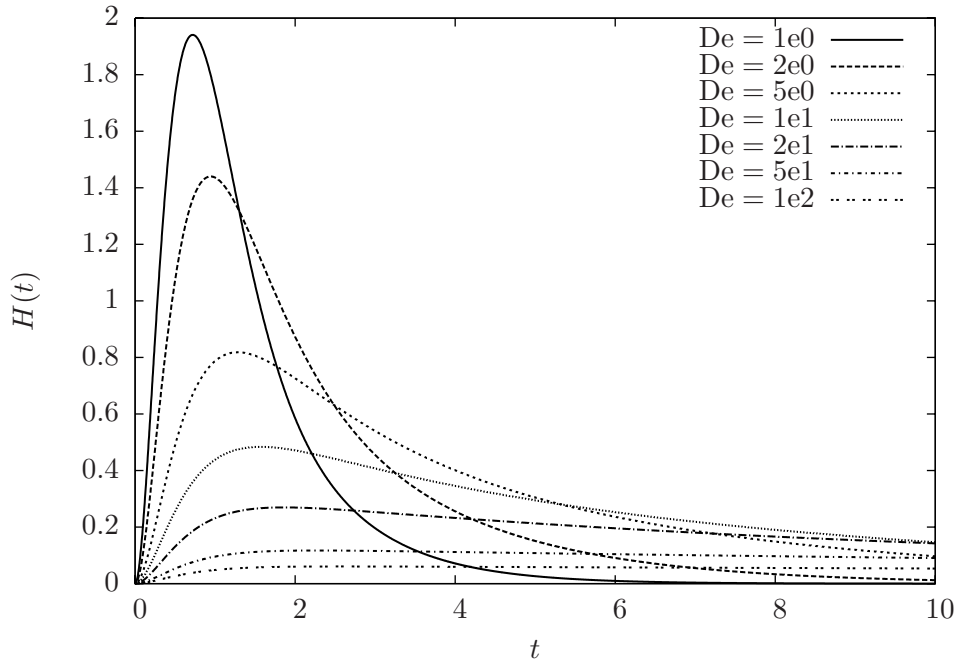
Fig. 6.1: Three-dimensional Taylor-Green vortex. Time-evolution of the total elastic energy for different values of the Deborah number.

Thus, the initial energy transfer from the velocity field to the elastic stresses is lower at high-Deborah number, which explains the behaviour reported in figure 6.1. Since less energy is stored in the dumbbells, the decay on the kinetic energy presented in figure 6.2 is slower at high-Deborah number. Moreover, local minimas of kinetic energy occur at relatively low energy levels. When the kinetic energy re-increases, elastic energy is transferred back under kinetic form. The total energy of the flow represented in figure 6.3 is monotonically decaying since no energy is injected into the system through boundary conditions, and volume or surface forces.

Perhaps most interestingly, no problem was encountered while increasing the Deborah number, retaining numerical stability and physical consistency all along. As already mentioned, this was achieved enforcing the tolerance on the spatial and temporal errors to $\tau = 10^{-12}$.

Despite the high-Deborah numbers considered for the Taylor–Green vortex, the development of a wide range of space and time scales and the transition to a turbulent state is not observed since no energy is injected into the flow. Indeed, all the reported cases were resolved satisfying the accuracy constraints using only $q_i = 64$ Fourier modes in each spatial direction. Hence, the Taylor-Green vortex is not an appropriate test case for the investigation of elastic turbulence.

6.2   Large eddy simulation in periodic domains

For direct numerical simulations, and focusing on periodic domains, the key issue to avoid the loss of positiveness of the conformation tensor is the control of the error related to the spatial and temporal discretizations. In the case of large eddy simulations, by definition, the flow is under-resolved in space which was also identified by Kupfermann [32] and Hulsen *et al.* [27] as a cause for the loss of positiveness of the conformation tensor.

Hence, the first challenge for subgrid modelling is to compensate the under-resolution of the flow

Fig. 6.2: Three-dimensional Taylor-Green vortex. Time-evolution of the total kinetic energy for different values of the Deborah number.
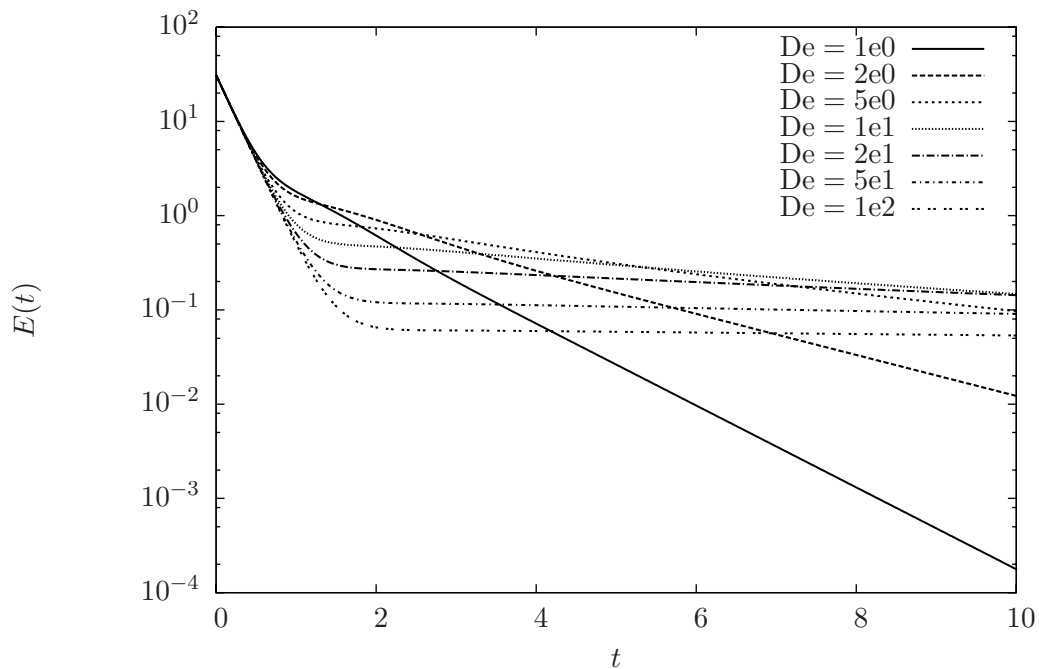
Fig. 6.3: Three-dimensional Taylor-Green vortex. Time-evolution of the total energy for different values of the Deborah number.

in order to maintain the positiveness of the conformation tensor, which is already a complicated task. Moreover, the subgrid model must perform a correct modelling of the subgrid scales whose physical behaviour is not clearly understood. However, if the positiveness of the conformation tensor is conserved, a correct subgrid modelling can be expected.

6.2.1 Viscoelastic Kolmogorov flow

The simplest configuration which enables the study of elastic turbulence in periodic domains is referred to as the Kolmogorov flow [2], which is considered in two spatial dimensions. Defining a forcing term of the form

$$\boldsymbol{g} = \left(\begin{array}{c} \mathrm{C}\cos(\mathrm{k}y) \\ 0 \end{array} \right), \qquad \mathrm{k} = \frac{2\pi\mathrm{n}}{\mathrm{L}}, \qquad \mathrm{n} \in \mathbb{N}, \tag{6.12}$$

with $\mathrm{C} \in \mathbb{R}$, the system of equations (2.32)-(2.34) admits a fixed point, that is a laminar and steady state solution given by

$$\boldsymbol{v}_0 = \left(\begin{array}{c} \mathrm{V}\cos(\mathrm{k}y) \\ 0 \end{array} \right), \qquad \boldsymbol{\chi}_0 = \left(\begin{array}{cc} 2\,\mathrm{De}^2\sin(\mathrm{k}y)^2 + 1 & -\mathrm{De}\,\sin(\mathrm{k}y) \\ -\mathrm{De}\,\sin(\mathrm{k}y) & 1 \end{array} \right), \tag{6.13}$$

where the Deborah number is defined as in (6.9) and the reference velocity implicitly given by

$$\mathrm{C} = \nu(1 + \eta)\mathrm{k}^2\mathrm{V}. \tag{6.14}$$

The complete stability diagram of the Kolmogorov fixed point in the $(\mathrm{Re} - \mathrm{De})$ plane was given by Boffetta *et al.* in [8]. In the Newtonian limit, inertial instabilities occur above the critical value $\mathrm{Re_c} = \sqrt{2}$ [41]. On the other hand, for very low and vanishing Reynolds numbers, the Kolmogorov flow displays purely elastic instabilities for sufficiently high Deborah numbers.

The goal of the large eddy simulation presented hereafter is to reproduce the transition from the laminar fixed point to turbulence in the regime of elastically-driven instabilities, with the aim of reaching a statistically-steady state and avoiding the loss of positiveness of the conformation tensor induced by the coarse spatial discretization.

6.2.2 Grid filter modelling

According to the approach described in chapter 4, grid filter modelling exclusively relies on the approximate inversion of the sampling filter which allows to compute the modelling filter defined in equation (4.23).

However, using the particular sampling filter inverse proposed in section 4.4 also requires to find an approximate inverse of the grid filter for the approximation of the weight matrix in equation (4.56). Hence, the approximate inverse of the grid and sampling filters used for the large eddy simulation of the Kolmogorov flow are presented hereafter.

The direct numerical simulations reported herein are performed with $\mathrm{q}_i = 512$ modes per space direction, while $\mathrm{p}_i = 256$ modes are used for the corresponding large eddy simulations. The number of modes is actually divided by two which is equivalent to the under-resolution used for the large eddy simulation of the lid-driven cavity flow presented in chapter 5.

Approximate inverse of the sampling filter

Since the evolution of the Kolmogorov flow is considered from the laminar fixed point to a turbulent state, the linearised approach presented in section 5.3.1 can not be applied in this context. Hence, the approximate inverse of the sampling filter is re-evaluated as the state of the system changes using the general non-linear formulation (4.55), that is

$$\underline{\mathbf{S}}' = \underline{\mathbf{U}} \, \underline{\mathbf{S}}^{\mathrm{T}} (\underline{\mathbf{S}} \, \underline{\mathbf{U}} \, \underline{\mathbf{S}}^{\mathrm{T}})^{-1}, \tag{6.15}$$

where the weight matrix is given by equation (4.56)

$$\underline{\mathbf{U}}_{ij} = \underline{\mathbf{u}}_i \delta_{ij} \simeq \underline{\mathbf{G}}'_{ik} \hat{\underline{\mathbf{u}}}_k \delta_{ij}, \tag{6.16}$$

which requires therefore the additional definition of an approximate inverse of the grid filter.

Approximate inverse of the grid filter

In contrast with the modelling used for the lid-driven cavity flow, the case of the two-element and static-basis approximation (4.43) is considered to express the approximate inverse of the grid filter. The first approximate inverse is the Moore–Penrose pseudo-inverse obtained with the no-coupling approach presented in section 4.5.1 and given by

$$\underline{\mathbf{G}}''_1 = \begin{pmatrix} \mathbf{I} \\ \mathbf{0} \end{pmatrix}, \tag{6.17}$$

which is recalled from equation (4.73). The second basis matrix relies on the probabilistic coupling and the use of the Gaussian mapping function (5.9), leading to a matrix of the form

$$\underline{\mathbf{G}}''_2 = \begin{pmatrix} \mathbf{I} \\ \underline{\mathbf{R}}''_2 \end{pmatrix}, \tag{6.18}$$

which does not predict a null subgrid field. According to the definition of the weight parameter (4.92), the approximate inverse of the grid filter becomes

$$\underline{\mathbf{G}}' = (1 - \theta)\underline{\mathbf{G}}''_1 + \theta\underline{\mathbf{G}}''_2. \tag{6.19}$$

In this case, the dynamic weight parameter can be interpreted as an indicator of the importance of the subgrid field and computed according to (4.94).

Modelling filter

Using the approximate inverse of the sampling filter given in equation (6.15) allows to compute the modelling filter according to equation (4.23)

$$\tilde{\underline{\mathbf{G}}} = \underline{\mathbf{G}} \, \underline{\mathbf{S}}'. \tag{6.20}$$

Like for the spectral elements method, the modelling filter obtained by this procedure is diagonal in the case of the Fourier basis, which seems quite involved to demonstrate since the definition of the sampling operation relies on the inversion of a full matrix, see equation (4.19).

As illustrated in figure 6.4, when the weight parameter vanishes, the modelling filter is the identity matrix since no subgrid field is predicted by the approximate inverse of the grid filter. In other words, the model vanishes since the flow is predicted as fully resolved. For increasing values of the weight parameter, the modelling filter becomes more and more effective.
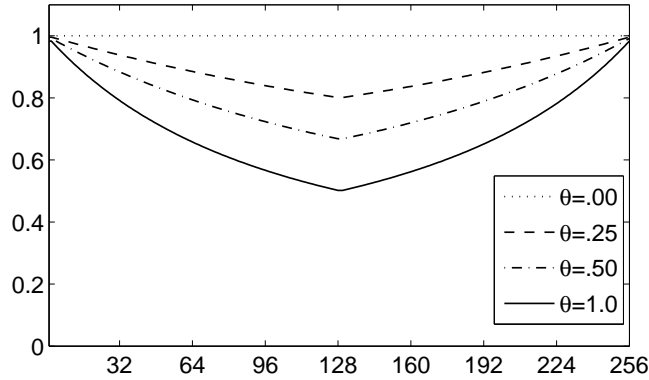
Fig. 6.4: Diagonal coefficients of the modelling filter obtained with different values of the weight parameter, for $q_i = 512$ and $p_i = 256$.

6.2.3   Evolution of the flow resistance

In order to analyse the transition from the laminar fixed point to a statistically-steady turbulent state, the evolution of the flow resistance to the external forcing is considered. Normalising this quantity with respect to the laminar fixed point yields

$$R(t) = \frac{\langle \boldsymbol{v} \cdot \boldsymbol{g} \rangle}{\langle \boldsymbol{v}_0 \cdot \boldsymbol{g} \rangle} = \frac{2\langle \boldsymbol{v} \cdot \boldsymbol{g} \rangle}{\nu(1+\eta)(kV)^2}. \tag{6.21}$$

This quantity is presented as a function of time in figure 6.5. While no numerical instability is encountered for the direct numerical simulation, the large eddy simulation is affected by an Hadamard instability after 11 adimensional time units. Hence, the aim of reaching the statistically-steady state of the Kolmogorov flow by large eddy simulation could not be achieved.
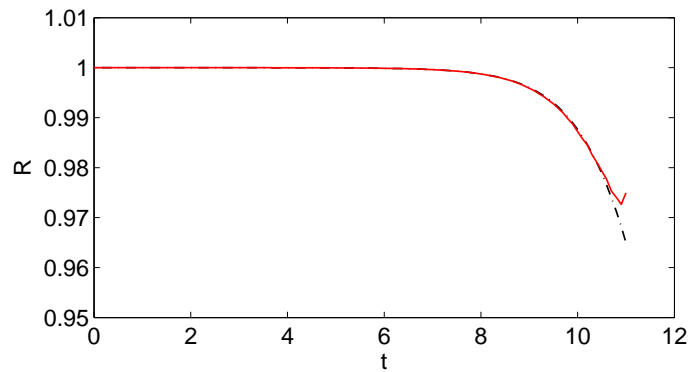
Fig. 6.5: Evolution of the flow resistance for $q_i = 512$ and $p_i = 256$ with De = 16. Large eddy simulation in red-solid line, direct numerical simulation in black-dash-dotted line.

A possibility to overcome this issue would be to mathematically enforce the positiveness of the conformation tensor. Several methods have been proposed in this scope, such as the continuous eigendecomposition and the Cholesky decomposition presented by Vaithianathan *et al.* in [60], but also the log-matrix formulation introduced by Hulsen *et al.* in [27]. While such methods could allow to obtain numerically stable simulations, they would only cure the consequences and not the cause,

that is the dismal modelling performance performed by the grid filter model presented in section 6.2.2.

Despite many attempts, a better subgrid modelling which enables to avoid the loss of positiveness of the conformation tensor could not be achieved, thereby always leading to the same type of unphysical instabilities. This illustrates the improvements which are required in terms of grid filter modelling for the large eddy simulation of elastic turbulence.

Chapter 7

Conclusions and perspectives

A possible way towards the suppression of functional modelling for deconvolution-based subgrid models has been paved, which was defined as the driving motivation of this work. This achievement potentially allows to extend the use of such models to the large eddy simulation of flows which can not be modelled using the functional strategy.

However, this proposal only represents a possibility among others and several bifurcations have been highlighted throughout the presentation. In this concluding chapter, a review of the achievements and the perspectives is presented in order to highlight the possible starting points for further researches.

7.1 Achievements

The key idea of the method is to consider the effects of the coarse spatial discretization used for large eddy simulation as the only effective filter applied to the macroscopic equations. In this context, the grid filter models are defined as a particular class of deconvolution-based subgrid models which allows to approximate the effect of the scales lost by spatial discretization on the resolved scales of the flow. Moreover, this gives a theoretical justification to the use of deconvolution models for the entire subgrid modelling and the classical distinction between the hard and the soft deconvolution problems appears useless.

In this framework, a general method for the computation of the convolution filter which models the effect of the grid filter on the computable scales of the solution is proposed, thereby providing a first answer to the key issue of the numerical discretization in large eddy simulation. More precisely, the definition of the convolution filter relies on the use of an approximate inverse of the sampling filter, which opens a wide range of modelling strategies.

In order to overcome this major issue, a general method for the approximate inversion of projective operators is proposed. Building a basis of the space of the possible inverses, a particular approximate inverse is expressed as a linear combination in this basis. Based on this general method, a purely algorithmic and intuitive strategy for the approximate inversion of the sampling filter is introduced and requires the use of the original quantities. Since these are unknown when performing a large eddy simulation, an approximate inverse of the grid filter is also needed and relies on the physical modelling of the coupling between the modes in modal space.

The large eddy simulation of the lid-driven cavity flow enabled a first validation of the grid filter models and the corresponding grid filter modelling presented in section 5.3. In this particular case, gradually removing functional modelling seems to provide subgrid modelling of increasing quality. However, when further decreasing the spatial resolution, the quality of subgrid modelling obtained by this approach becomes to low, even for the correct prediction of the first-order statistics, which already appears as a measure of the improvements required in terms of grid filter modelling.

The large eddy simulation of the viscoelastic Kolmogorov flow is considered in order to extend the validity domain of the grid filter models. In this framework, compensating the errors related

to the coarser spatial discretization in order to avoid the unphysical loss of positiveness of the conformation tensor has been envisaged as a challenge. While the aim of the large eddy simulation is to reach a statistically-steady and turbulent state from the Kolmogorov fixed point, the dismal performance of the grid filter modelling presented in section 6.2.2 did not allow to avoid the onset of Hadamard instabilities in the transitional phase.

7.2   Further developments

As mentioned in the introduction of this work, this modelling approach was presented as a straight path but improvements and other solutions could and have to be envisaged in order to increase the performance of the grid filter modelling. Such improvements would enable the large eddy simulation of more complex flows, with more complex fluids and the coarsening of the required spatial resolutions in order to further decrease the computational costs.

The first central issue is related to the approximate inversion of the sampling filter which bears the entire subgrid modelling in the particular framework of the grid filter models. The proposal presented in this work is based on the *ansatz* (4.44) and corresponds to the intuitive strategy of unfolding the modes in modal space. This approximation method could certainly be replaced by others and the approximate inversion could also be performed in physical space.

For the approximate inversion of the grid filter, other basis matrices could be considered by defining other interpretations of the Jacobian appearing in equation (4.61). Three intuitive interpretations of this quantity, which describes the coupling of the modes in modal space, were given but these do not represent an exhaustive presentation. Moreover, the mapping functions appearing in equations (4.77) and (4.85) could perhaps be determined by analytical approaches based on simplified theories of turbulence.

As detailed in section 4.5.2, another important issue is to generalise the method for the determination of the coefficients in (4.42) and (4.43) which would allow to use a general n-dimensional basis of the admissible subspace, thereby potentially improving the accuracy of the approximate inversion of projective operators.

Another aspect which has been introduced but completely neglected is the dual approach of the grid filter models, that is the sampling filter models. Their definition raises a fundamental question about the nature of the implicit filter associated with the spatial discretization which shall be considered in large eddy simulation, thereby hopefully opening one more subject for the *disputatio*.

List of Figures

List of Tables

Bibliography

[1] N. Anderson and G. L. Comer, *Relativistic fluid dynamics: Physics for many different scales*, Living Rev. Relativity **10** (2007), no. 1.

[2] V. I. Arnold and L. D. Meshalkin, *A. Kolmogorov's seminar on selected problems of analysis*, Uspekhi Mat. Nauk **15** (1960), no. 1(91), 247–250.

[3] J. Bardina, J. H. Ferziger, and W. C. Reynolds, *Improved subgrid scale models for large eddy simulation*, AIAA J. **80** (1980).

[4] P. Bergé, Y. Pomeau, and C. Vidal, *De l'ordre dans le chaos, vers une approche déterministe de la turbulence*, Hermann, Paris, 1988.

[5] S. Berti, A. Bistagnino, G. Boffetta, A. Celani, and S. Musacchio, *Two-dimensional elastic turbulence*, Phys. Rev. E **77** (2008), no. 5, 055306.

[6] R. B. Bird and J. M. West, *Constitutive equations for polymeric liquids*, Ann. Rev. Fluid Mech. **27** (1995), 169–193.

[7] C. Boeckle, *On the origins of numerical instabilities in the simulations of viscoelastic fluid flows*, Master's thesis, École Polytechnique Fédérale de Lausanne, Section de Physique, 2009.

[8] G. Boffetta, A. Celani, A. Mazzino, A. Puliafito, and M. Vergassola, *The viscoelastic Kolmogorov flow: eddy viscosity and linear stability*, J. Fluid Mech. **523** (2005), 161–170.

[9] J. Botsis and M. Deville, *Mécanique des milieux continus: une introduction*, Presses Polytechniques Universitaires Romandes, 2006.

[10] R. Bouffanais, *Simulation of shear-driven flows: transition with a free surface and confined turbulence*, Ph.D. thesis, no. 3837, École Polytechnique Fédérale de Lausanne, 2007.

[11] R. Bouffanais, M. O. Deville, and E. Leriche, *Large-eddy simulation of the flow in a lid-driven cubical cavity*, Phys. Fluids **19** (2007), Art. 055108.

[12] J. P. Boyd, *Two comments on filtering (artificial viscosity) for Chebyshev and Legendre spectral and spectral element methods: Preserving boundary conditions and interpretation of the filter as a diffusion*, J. Comput. Phys. **143** (1998), 283–288.

[13] M. E. Brachet, D. I. Meiron, S. A. Orszag, B. G. Nickel, R. H. Morf, and U. Frisch, *Small-scale structure of the Taylor–Green vortex*, J. Fluid Mech. **130** (1983), 411–452.

[14] C. Canuto, M. Y. Hussaini, A. Quarteroni, and T. A. Zang, *Spectral Methods – Fundamentals in Single Domains*, Springer Verlag, 2006.

[15] P. Chassaing, *Turbulence en mécanique des fluides*, Cépaduès-Editions, Toulouse, 2000.

[16] W. Couzy and M. O. Deville, *A fast Schur complement method for the spectral element discretization of the incompressible Navier–Stokes equations*, J. Comput. Phys. **116** (1995), 135–142.

[17] M. O. Deville, P. F. Fischer, and E. H. Mund, *High-order methods for incompressible fluid flow*, Cambridge University Press, Cambridge, 2002.

[18] J. A. Domaradzki and N. A. Adams, *Direct modelling of subgrid scales of turbulence in large-eddy simulations*, J. of Turbulence **3** (2002), no. 24.

[19] Y. Dubois-Pèlerin, V. Van Kemenade, and M. O. Deville, *An object-oriented toolbox for spectral element analysis*, J. Sci. Comput. **14** (1999), 1–29.

[20] M. Germano, U. Piomelli, P. Moin, and W. H. Cabot, *A dynamic subgrid-scale eddy viscosity model*, Phys. Fluids A **3** (1991), 1760–1765.

[21] B. J. Geurts, *Inverse modeling for large-eddy simulation*, Phys. Fluids **9** (1997), 3585–3587.

[22] T. Gmür, *Méthode des éléments finis en mécanique des structures*, Presse Polytechniques Universitaires Romandes, Lausanne, 2000.

[23] A. Groisman and V. Steinberg, *Elastic turbulence in a polymer solution flow*, Nature **405** (2000), 53–55.

[24] M. A. Habisreutinger, *Large-eddy simulation of turbulent flows by approximate deconvolution models using spectral element method*, Master's thesis, École Polytechnique Fédérale de Lausanne, Section de Génie Mécanique, 2006.

[25] M. A. Habisreutinger, R. Bouffanais, E. Leriche, and M. O. Deville, *A coupled approximate deconvolution and dynamic mixed scale model for large-eddy simulation*, J. Comput. Phys. **224** (2007), 241–266.

[26] E. Hairer, S. Nørsett, and G. Wanner, *Solving ordinary differential equations I*, Springer-Verlag, 1993.

[27] M. A. Hulsen, R. Fattal, and R. Kupfermann, *Flow of viscoelastic fluids past a cylinder at high Weissenberg number: Stabilized simulations using matrix logarithms*, J. Non-Newtonian Fluid Mech. **127** (2005), 27–39.

[28] A. N. Kolmogorov, *Dissipation of energy under locally isotropic turbulence*, Dokl. Akad. Nauk SSSR **32** (1941), 16–18.

[29] ———, *The local structure of turbulence in an incompressible fluid at very high Reynolds numbers*, Dokl. Akad. Nauk SSSR **30** (1941), 301–305.

[30] ———, *Equations of turbulent motion of an incompressible fluid*, Izvest. Acad. of Sci., SSSR, Physics **6** (1942), 56–58.

[31] J. G. M. Kuerten, B. J. Geurts, A. W. Vreman, and M. Germano, *Dynamics inverse modeling and its testing in large-eddy simulation of the mixing layer*, Phys. Fluids **11** (1999), 3778–3785.

[32] R. Kupferman, *On the linear stability of plane Couette flow for an Oldroyd-B fluid and its numerical approximation*, J. Non-Newtonian Fluid Mech. **127** (2005), 169–190.

[33] L. Landau and E. Lifschitz, *Physique théorique, tome 6, Mécanique des fluides*, Editions MIR, Moscow, 1989.

[34] R. G. Larson, *Constitutive equations for polymer melts and solutions*, Butterworths, Boston, 1988.

[35] E. Leriche, *Direct numerical simulation of lid driven cavity at high-Reynolds numbers*, J. Sci. Comput. **27** (2006), 335–345.

[36] E. Leriche and S. Gavrilakis, *Direct numerical simulation of the flow in the lid-driven cubical cavity*, Phys. Fluids **12** (2000), 1363–1376.

[37] D. K. Lilly, *A proposed modification of the Germano-subgrid-scale closure method*, Phys. Fluids A **4** (1992), 633–635.

[38] Y. Maday and A. T. Patera, *Spectral element methods for the incompressible Navier–Stokes equations*, State-of-the-Art Survey on Computational Mechanics, A. K. Noor & J. T. Oden Eds., pp. 71–142, ASME, New-York, 1989.

[39] Y. Maday, A. T. Patera, and E. M. Rønquist, *The $\mathbb{P}_N \times \mathbb{P}_{N-2}$ method for the approximation of the Stokes problem*, Tech. Report 92009, Department of Mechanical Engineering, MIT, Cambridge, MA, 1992.

[40] B.S. Massey, *Units, dimensional analysis and physical similarity*, Van Nostrand Reinhold, London, 1971.

[41] L. Meshalkin and Y. G. Sinai, *Investigation of the stability of a stationary solution of a system of equations for the plane movement of an incompressible viscous liquid*, J. Appl. Math. Mech. **25** (1961), 1700–1705.

[42] G. I. Ogilvie and M. R. E. Proctor, *On the relation between viscoelastic and magnetohydrodynamic flows and their instabilities*, J. Fluid Mech. **476** (2003), 389–409.

[43] J. Oldroyd, *On the formulation of rheological equations of state*, Proc. Roy. Soc. Lond. A **200** (1950), 523–541.

[44] S. A. Orszag, *Numerical simulation of incompressible flows within simple boundaries*, Studies in Applied Mathematics **50** (1971), 293–327.

[45] R. G. Owens and T. N. Phillips, *Computational Rheology*, Imperial College Press, London, 2002.

[46] J. B. Perot, *An analysis of the fractional step method*, J. Comput. Phys. **108** (1993), 51–58.

[47] U. Piomelli, P. Moin, and J. H. Ferziger, *Model consistency in large eddy simulation of turbulent channel flows*, Phys. Fluids **31** (1988), 1884–1891.

[48] C. D. Pruett, B. C. Thomas, C. E. Grosch, and T. B. Gatski, *A temporal approximate deconvolution model for large-eddy simulation*, Phys. Fluids **18** (2006), Art. 028104.

[49] A. Quarteroni, R. Sacco, and F. Saleri, *Méthodes numériques pour le calcul scientifique*, Springer-Verlag, 2000.

[50] A. Quarteroni and A. Valli, *Numerical Approximation of Partial Differential Equations*, Springer Series in Computational Mathematics, Springer, Berlin, 1994.

[51] I. L. Rhyming, *Dynamique des fluides*, Presses Polytechniques Universitaires Romandes, Lausanne, 1991.

[52] P. Sagaut, *Large eddy simulation for incompressible flows: an introduction*, 3rd ed., Springer, Berlin, 2005.

[53] K. B. Shah and J. Ferziger, *A new non-eddy viscosity subgrid-scale model and its application to channel flow*, Annual Research Briefs, Center for Turbulence Research, NASA/ Stanford Univ., 1995, pp. 73–90.

[54] J. S. Smagorinsky, *General circulation experiments with the primitive equations. I: The basic experiment*, Month. Weath. Rev. **91** (1963), 99–165.

[55] S. Stolz and N. A. Adams, *An approximate deconvolution procedure for large-eddy simulation*, Phys. Fluids **11** (1999), 1699–1701.

[56] S. Stolz, N. A. Adams, and L. Kleiser, *The approximate deconvolution model for large-eddy simulations of compressible flows and its application to shock-turbulent-boundary-layer interaction*, Phys. Fluids **13** (2001), 2985–3001.

[57] A. H. Taub, *Relativistic Rankine-Hugoniot equations*, Phys. Rev. **74** (1948), no. 3, 328–334.

[58] B. Thomases and M. Shelley, *Emergence of singular structures in Oldroyd-B fluids*, Phys. Fluids **19** (2007), no. 103103.

[59] B. Toms, *Early experiments on drag reduction by polymers*, Phys. Fluids **20** (1977), no. 10, S3–S5.

[60] T. Vaithianathan and L.R. Collins, *Numerical approach to simulating turbulent flow of a viscoelastic polymer solution*, J. Comput. Phys. **187** (203), no. 1, 1–21.

[61] G. S. Winckelmans, A. A. Wray, O. V. Vasilyev, and H. Jeanmart, *Explicit-filtering large-eddy simulation using the tensor-diffusivity model supplemented by a dynamic Smagorinsky term*, Phys. Fluids **13** (2001), 1385–1403.

[62] Y. Zang, R. L. Street, and J. R. Koseff, *A dynamic mixed subgrid-scale model and its application to turbulent recirculating flows*, Phys. Fluids A **5** (1993), 3186–3193.

[63] L. Zuppiroli, *La bulle universitaire*, Editions d'en bas, 2010.

Curriculum Vitae

Marc A. Habisreutinger   marc.habisreutinger@gmail.com

Teaching Assistant and Ph.D. Student at EPFL   Swiss, Italian
R&D Engineer at Enairys Powertech SA   12 September 1982, Geneva

EPFL - STI - IGM - LIN, Station 9   Rue de la Madeleine 4
CH - 1015 Lausanne   CH - 1003 Lausanne
Tel. +41 21 693 69 94   Tel. +41 76 393 42 21

Main professional interests

Engineering, especially for sustainable development, energy supply and transportation
Modelling and numerical simulation in fluid and solid mechanics or environmental systems
Continuous media mechanics, statistical mechanics, fundamental physics

Education

Philosophy Doctorate in fluid and solid mechanics. *Turbulence modelling for the simulation of complex flows of complex fluids*. Ecole Polytechnique Fédérale de Lausanne, Switzerland.   2006-2010

Master of Science in mechanical engineering. *Simulation of Newtonian fluid turbulent flows*. Ecole Polytechnique Fédérale de Lausanne, Switzerland.   2001-2006

Federal and cantonal maturity. *Scientific option*. Collège de Calvin, Geneva, Switzerland.   1997-2001

Professional experience

Lecturer. *Numerical simulation*. Ecole Polytechnique Fédérale de Lausanne, Switzerland.   since 2011

Research Scientist. *Statistical modelling and simulation dedicated to the prediction of environmental risks*. Institut de gestion et d'analyse du risque, Faculté de géosciences et environnement, Université de Lausanne, Switzerland.   2010-2011

R&D Engineer. *Design, simulation and development of energy storage and transfer solutions based on compressed air technologies*. Enairys Powertech SA, Parc Scientifique Ecublens, Switzerland.   since 2008

Teaching Assistant. *Teaching of exercise sessions and student supervision for semester projects and Master theses*. Laboratoire d'ingénierie numérique, Ecole Polytechnique Fédérale de Lausanne, Switzerland.   2006-2010

Numerical fluid dynamics internship. *Aero- and thermodynamic simulation of high-speed trains in confined spaces*. Fondation Numexia, Parc Scientifique Ecublens, Switzerland.   2004

Mechanical engineering and machining internship. *Machining and design of pneumatic engine and brake systems*. Bobst SA. Prilly, Switzerland.   2003

MAIN PUBLICATIONS

Grid filter models for large eddy simulation. R. Bouffanais, Marc A.   2008
Habisreutinger, Michel O. Deville. *Proc. Appl. Math. Mech., (7), 1101203-
1101204.*

A coupled approximate deconvolution and dynamic mixed scale   2007
model for large eddy simulation. Marc A. Habisreutinger, Roland Bouf-
fanais, Emmanuel Leriche, Michel O. Deville. *J. Comput. Phys., (224), 241-
266.*

Can a Helmholtz solver run on a cluster? Ralf Gruber, Vincent Keller,   2006
Emmanuel Leriche, Marc A. Habisreutinger. *IEEE International Conference on
Cluster Computing, 1-8, ISBN 1-4244-0327-8.*

HONNORS AND AWARDS

Ryhming award. Original contribution to the knowledge of fluid mechanics   2006
during a Master or Ph.D. thesis performed at Ecole Polytechnique Fédérale de
Lausanne.

Special award of the Collège Calvin, Geneva. Co-author of a reference   2000
lecture book in mathematics.

INVITED PRESENTATIONS

Laboratory of Fluid Mechanics and Instabilities seminars. *Prof.*   07.2010
François Gallaire. Ecole Polytechnique Fédérale de Lausanne, Switzerland.

Annual Meeting of the Leonhard Euler Center. *European Research Com-*   11.2006
munity on Flow Turbulence and Combustion. Lausanne, Switzerland.

CONFERENCE PRESENTATIONS

International Conference On High-Order And Spectral Methods.   06.2009
Trondheim, Norway.

International Conference on Turbulence and Interactions. Martinique,   06.2009
France.

International Congress on Rheology. Monterey (CA), USA.   08.2008

French Congress on Mechanics. Grenoble, France.   08.2007

International Congress on Industrial and Applied Mathematics.   07.2007
Zürich, Switzerland.

International Conference On High-Order And Spectral Methods. Bei-   06.2007
jing, PRC.

Annual Meeting of the Division of Fluid Dynamics. Tampa Bay, USA.   11.2006

Teaching-assistant experience

Continuum media mechanics. *Prof. Michel Deville*. Bachelor course in mechanical engineering, EPFL.	2009
Incompressible fluid mechanics. *Prof. Peter Monkewitz*. Bachelor course in mechanical engineering, EPFL.	2008-2009
Finite differences and finite volumes methods. *Dr. Mark Sawley*. Bachelor course in mechanical engineering, EPFL.	2008-2010
Numerical flow simulation. *Dr. Mark Sawley*. Master course in mechanical engineering, EPFL.	2006-2010
Finite elements method for incompressible flows. *Prof. Michel Deville*. Master course in mechanical engineering, EPFL.	2006-2010
Compressible fluid mechanics. *Dr. Alain Drotz*. Bachelor course in mechanical engineering, EPFL.	2006-2008
Finite elements method. *Prof. Thomas Gmür*. Bachelor course in mechanical engineering, EPFL.	2004-2006
Vibratory mechanics. *Prof. Thomas Gmür*. Bachelor course in mechanical engineering, EPFL.	2004-2006

Main supervision activities

Simulation of viscoelastic fluid flows. *Christoph Boeckle*. Master thesis, EPFL.	2008-2009
Turbulence modelling for the simulation of complex flows. *Sohrab Kehtari*. Master semester-project, EPFL.	2007-2008
Numerical heart modelling and cardiac cycle simulation. *Marcel Vonlanthen*. Master semester-project, EPFL.	2007-2008

Languages

French	mother tongue	**English**	fluent C1
Italian	mother tongue	**German**	intermediate B1

Software knowledge

Operating systems	Linux/Unix, Windows, Mac-OS
Computer-aided design	Catia, Ideas, SolidWorks
Comp. fluid dynamics	Fluent, Star-CCM^{++}, CFX, ICEM-CFD, Gambit, T-Grid
Programming	Fortran, C^{++}, Matlab/Octave, MPI, bash/sh
Multi-purpose simulation	Comsol Multiphysics
Visualisation	Paraview, Tecplot, FieldView

Hobbies

Tennis, ski, hiking, cycling, sailing.